

# Dynamics of Self-Propelled Particles: Diffusion, Motility-Sorting, and Rectification

Inaugural-Dissertation

zur

Erlangung des Doktorgrads

der Mathematisch-Naturwissenschaftlichen Fakultät

der Universität zu Köln

vorgelegt von

Andrea Costanzo

aus Rom, Italien

Köln  
2015

Berichterstatter: Prof. Dr. Gompper

Prof. Dr. A. Schadschneider

Dr. M. Ripoll

Tag der mündlichen Prüfung: 20. April 2015

## Zusammenfassung

Selbstangetriebene Teilchen wandeln laufend gespeicherte Energie in kinetische Energie um. Sie sind daher nicht im thermodynamischen Gleichgewicht. Selbstangetriebene Teilchen haben ein deutlich anderes Verhalten als passive Brownsche Teilchen. Die kollektiven Phänomene, die durch die Wechselwirkung vieler selbst-angetriebenen Teilchen entstehen, sind besonders vielfältig und interessant. Die Forschung über das Verhalten selbstangetriebener Teilchen ist in den letzten Jahren stark gewachsen. Trotz der vielen Beobachtungen und Erklärungen, die bis jetzt gemacht wurden, mangelt es an einem allgemeinen theoretischen Bild, das die ähnlichen kollektiven Erscheinungen, die in unterschiedlichen Systemen zu beobachten sind, einheitlich beschreibt.

Wir erforschen hier mit Computersimulationen verschiedene Eigenschaften der Dynamik selbstangetriebener Stäbchen in zwei Dimensionen. Wir untersuchen vor allem "Run-and-Tumble"-Teilchen. Die Dynamik solcher Teilchen ist durch zwei Phasen charakterisiert. Während der "Run"-Phase bewegt sich das Teilchen geradlinig. Diese geradlinige Fortbewegung wird zu zufälligen Zeiten vom "Tumbling" unterbrochen. Während des "Tumbling" bewegt sich das Teilchen nicht fort, sondern dreht sich. Das Nacheinanderfolgen von "Run" und "Tumble" ergibt eine Art Zufallsbewegung oder Irrfahrt, die gut die echte Bewegung von Bakterien wie *E. coli* beschreibt.

Wir untersuchen zuerst die Bewegung von "Run-and-Tumble"-Stäbchen im Volumen. Die Rotationsdiffusion steigt mit der Teilchendichte in einer bestimmten Region des Teilchenlänge-Geschwindigkeits-Phasenraums an, im Gegensatz zu passiven Brownschen Stäbchen, für die die Anwesenheit von Nachbarpartikeln immer die Teilchenrotation erschwert. Dieses Phänomen kann mit einem Aktiv-Gas-Bild verstanden werden, das die Teilchenkollisionen als binäre Punktkollisionen betrachtet, die zu keiner Ausrichtung führen. Beim Vergrößern der Länge des Teilchens erzeugen Kollisionen zwischen den Teilchen mehr Ausrichtung. Die Stäbchen bewegen sich parallel zusammen weiter für eine nicht vernachlässigbare Zeit, was zu Clusterbildung führen kann. Die Rotationsdiffusion nimmt mit der Teilchendichte ab, und das aktiv-Gas-Bild ist nicht mehr gültig.

Die spontane Segregation von aktiven Teilchen mit unterschiedlichen Selbstantriebskräften (Geschwindigkeiten) in Mikrokanälen wird ebenfalls untersucht. Aktive Teilchen in Mikrokanälen zeigen Anhäufung an den Wänden des Kanals. Hier zeigen wir, dass schnellere Teilchen die langsameren von den Wänden vertreiben, so dass eine Trennung der Teilchen zustande kommt. Das Phänomen wird als Funktion von Teilchengeschwindigkeiten, Teilchendichte und Kanalbreite untersucht. In Anwesenheit einer Poiseuille-Strömung zeigen aktive Teilchen das "upstream-swimming", eine der Strömung entgegengerichtete Fortbewegung, die besonders an den Wänden des Kanals zu beobachten ist. Da dieser Effekt von der Motilität abhängt, zeigen wir hier, dass die Strömungsgeschwindigkeit so eingestellt wer-

---

den kann, dass langsamere und schnellere Teilchen getrennt werden können. Anwendungen können in der Entwicklung von “microfluidic lab-on-chip devices” für die kontrollierte Trennung von Teilchen mit verschiedenen Geschwindigkeiten liegen.

Zuletzt untersuchen wir die Bewegung von selbstangetriebenen Teilchen in Mikrokanälen mit asymmetrischen Wänden. Die Asymmetrie des Kanals bewirkt einen gerichteten Teilchenfluss, ein “Ratschen”-Effekt, also die Ausrichtung der sonst chaotischen Bewegung der Teilchen. Wir messen die Durchschnittsgeschwindigkeit der Teilchen als Funktion der relevanten Teilchen- und Kanalparameter. Die Ergebnisse können anhand der Trajektorien von Einzelteilchensimulationen ohne Tumbling verstanden werden. Mit steigender Teilchendichte nimmt der Ratscheneffekt ab. Nur in einigen Fällen, wenn Teilchen in den spitzen Winkeln der benutzten Kanal-Geometrie gefangen werden, zeigt ein System mit kleiner Dichte bessere Ausrichtung als Einzelteilchen. Für Zwei-Komponenten-Systeme, ist die Separation langsamer und schneller Teilchen näherungsweise proportional zum Ausrichtungseffekt von Ein-Komponenten-Systemen. Auch wenn in Mikrokanälen mit asymmetrischen Wänden keine Flüssigkeitsströmung gebraucht wird, um schnelle und langsame Teilchen zu trennen, sind sie für die Trennung von Teilchen mit unterschiedlichen Geschwindigkeiten weniger effektiv als Mikrokanäle mit Poiseuille-Strömung.

Die meisten unserer Ergebnisse sind recht allgemeingültig und von den Details des Modells unabhängig. Dies zeigt sich durch den Vergleich einiger beispielhafter Ergebnisse mit Ergebnissen, die wir mit anderen selbstangetriebenen-Teilchen Modellen erzielt haben. Die vorliegenden Resultate geben neue Einblicke in die faszinierende Welt der selbstangetriebenen Teilchen und der Physik des thermodynamischen Nichtgleichgewichts. Diese Ergebnisse sind besonders relevant für die Entwicklung von “lab-on-chip” Mikrofluidik-Modulen, mit denen die Manipulation, der Transport, die Kontrolle und die gerichtete Bewegung von Teilchen ohne die Benutzung externer Kraftfelder erreicht werden kann.

## Abstract

Self-propelled particles, or active particles, continuously convert stored energy into kinetic energy, and are therefore intrinsically out of thermodynamic equilibrium. Self-propelled particles have very different behaviors than their passive counterparts, and show very rich collective phenomena. In the last few years, the number of investigations on active particles has significantly grown, but a general picture connecting the emergence of similar collective behaviors from a great variety of systems is still lacking.

Here, the dynamics of self-propelled rod-like particles in two dimensions is investigated by means of numerical simulations. The main model we use corresponds to Run-and-Tumble particles which move straight for certain time (run), until they randomly change direction of motion (tumble). The sequence of these runs and tumbles leads to a kind of random walk that nicely models the motion of flagellated bacteria like *E. coli*.

We first study the diffusive motion of self-propelled elongated particles in the bulk. In a particular region of the particle length-velocity space, the rotational diffusion coefficient increases with density. This is in strong contrast to the case of passive elongated Brownian particles, where the presence of neighboring particles always diminish each particle's rotational motion. This enhancement of the rotation due to the particle activity can be understood with a simple active-gas picture. In this active-gas approximation, collision events are treated as two-particle point-like collisions, where no mutual alignment is induced. Increasing the particle aspect ratio, collisions among particles induce particle alignment, such that after each collision particles move together for some time, eventually forming larger clusters. The active-gas picture is no longer valid and rotational diffusion decreases with density.

Spontaneous segregation of active particles with different velocities in microchannels is also investigated. Self-propelled particles are known to accumulate in the proximity of walls. Here we show how fast particles expel slower ones from channel walls, leading to a segregated state. The mechanism is characterized as a function of particle velocities, particle density, and channel width. In the presence of capillary flow, self-propelled particles show upstream swimming at the channel walls. Since this effect depends on particle motility, we show that the solvent velocity can be tuned to segregate slow and fast particles. Promising applications can be found in the development of microfluidic lab-on-a-chip devices for sorting of particles with different motilities.

Finally, the motion of self-propelled particles in microchannels with asymmetric ratchet-like walls is analyzed. The asymmetry of the channel induces a net flux of particles in a determined direction with a flow which shows to be planar. We quantify the average flow velocity as a function of the relevant parameters of the self-propelled particles and the microchannel geometry. The results can be explained in terms of single-particle trajecto-

---

ries in the non-tumbling limit. With increasing particle density, the ratchet effect strongly decreases. Only in some cases, when particles get trapped in acute angles, a semi-dilute system performs better than a dilute one. For two-component systems, the separation of fast and slow particles is approximately proportional to the ratchet effect of single-component systems. Although the channel with ratchet-like walls does not need any imposed flow to separate fast and slow particles along the channel main axis, it turns out to be less effective in separating fast and slow particles compared to a channel with Poiseuille flow.

The results presented here are quite general since they are not dependent on the specific details of the self-propelled mechanism. Sample results obtained with run-and-tumble particles have been compared with results obtained with other models. The results we present are of great theoretical and practical interest, and they give new insights into the fascinating world of self-propelled particles and off-equilibrium systems. The presented findings are of particular relevance in the design of microfluidic lab-on-chip devices, where the manipulation, the transport, the control, and the directed motion of particles is achieved without the use of laser fields or other external invasive force fields.

---

## Contents

<b>1</b>	<b>Introduction</b>	<b>9</b>
1.1	Self-propelled particles . . . . .	9
1.2	Microswimmers . . . . .	10
1.2.1	<i>E. coli</i> bacteria . . . . .	11
1.2.2	Run-and-Tumble motion . . . . .	13
1.3	Hydrodynamics at the microscale . . . . .	15
1.3.1	Swimming at low Reynolds number . . . . .	18
1.3.2	Hydrodynamic Interactions . . . . .	19
1.4	Properties of self-propelled particles . . . . .	21
1.5	Theoretical models . . . . .	22
<b>2</b>	<b>Model</b>	<b>25</b>
2.1	Our self-propelled particle model . . . . .	25
2.2	Run-and-Tumble dynamics . . . . .	27
2.3	Channels with and without Poiseuille flow . . . . .	28
<b>3</b>	<b>Diffusion properties of Run-and-Tumbling particles</b>	<b>31</b>
3.1	Introduction . . . . .	31
3.2	Rotational diffusion enhancement . . . . .	35
3.2.1	Two-particles scattering analysis . . . . .	38
3.2.2	Cluster analysis . . . . .	40
3.2.3	Order parameter . . . . .	42
3.3	Translational diffusion . . . . .	42
3.3.1	Effective particle velocity . . . . .	44
3.4	Comparison between different noise types . . . . .	45
3.5	Summary . . . . .	47
<b>4</b>	<b>Motility-sorting of particles in micro-channels</b>	<b>49</b>
4.1	Introduction . . . . .	49
4.2	Channel without flow . . . . .	52
4.2.1	One component systems . . . . .	52
4.2.2	Two component systems . . . . .	53
4.3	Channels with Poiseuille flow . . . . .	60
4.3.1	One component systems . . . . .	61
4.3.2	Two component systems . . . . .	65
4.4	Channel with Poiseuille flow and membranes . . . . .	67
4.5	Comparison between different noise types . . . . .	67

4.6	Summary . . . . .	70
<b>5</b>	<b>Run-and-Tumbling particles in ratcheted-microchannels</b>	<b>73</b>
5.1	Introduction . . . . .	73
5.2	Geometry and observables . . . . .	76
5.3	Single-Particle Simulations . . . . .	78
5.3.1	Arm-geometry . . . . .	78
5.3.2	Wedge geometry . . . . .	89
5.3.3	Dependence on particle aspect ratio . . . . .	89
5.4	Effects of particle density . . . . .	91
5.5	Mixture of fast and slow particles . . . . .	97
5.6	Summary . . . . .	100
<b>6</b>	<b>Conclusions</b>	<b>103</b>



---

# 1 Introduction

## 1.1 Self-propelled particles

Self-propelled particles, or active particles, continuously convert stored energy in kinetic energy and are therefore intrinsically out of thermodynamic equilibrium, which leads to interesting and fascinating collective behaviors [1]. The study of self-propelled particle systems is a relatively new topic of particular relevance in the areas of Soft Matter Physics, Bio- and Micro-physics. There are many examples of self-propelled particles, both at the macro-scale and at the micro-scale, both by biological organisms and by synthetic particles.

Figure 1 shows some eye-catching examples of self-propelled living organisms at the macro-scale and their amazing properties like whirlpool formation of ants [2], synchronous swimming of fish [3], flocking of birds [4], and lane formation of pedestrians [5, 6]. At the micro-scale, biological self-propelled particles like bacteria or spermatozoa show also similar behavior [7]. There are also several examples of synthetic self-propelled particles at different length scales. These include chemically powered particles, like the so-called Janus particles, coated on one side with one material and on the other side with another material, such that the chemical reactions of the materials with the environment produce a net constant force on the particle which is then self-propelled [8, 9]. There are also studies on vehicular traffic [10, 11], which can be considered as an example of non-living self-propelled system, since cars continuously convert chemical energy of the gasoline into kinetic energy. It is worth noting that also granular matter, which consists of non-self-propelled small and thin particles on a substrate or in a box, when the substrate or the box is shaken externally, behaves very similarly to self-propelled systems [12].

There are many open questions regarding the study of self-propelled particles, concerning both the self-propelling mechanism of single particles [13], the interaction of single particles with obstacles like walls [14], and collective phenomena [1]. Different systems with different microscopic interaction rules show similar collective behavior. In classical equilibrium statistical mechanics, the relation between the microscopic interactions and

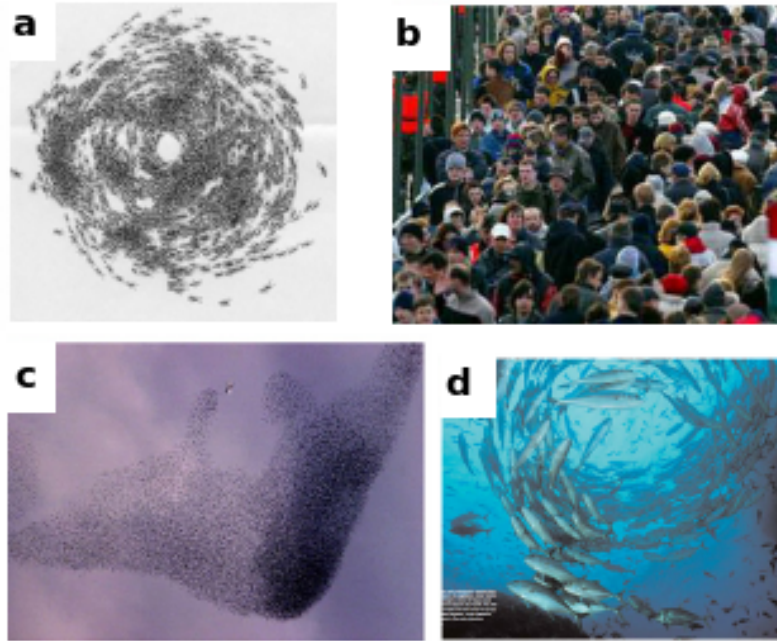


Figure 1: Collective behavior of self-propelled particles at the macro-scale. (a) A rotating colony of ants. (b) People spontaneously ordered into “traffic lanes”. (c) Starlings producing aerial displays. (d) Fish vortices. Taken from [1].

the macroscopic observables is well understood. For off-equilibrium systems, this question is still open and a field of ongoing research. The overarching question is whether there are general rules that apply to all this different systems.

## 1.2 Microswimmers

Here we focus our attention to biological self-propelled particles at the micro-scale. In nature, there is a rich variety on ways microorganisms achieve swimming and self-propulsion [13, 15]. In Figure 2, different types of living micro-swimmers are sketched, which employ different techniques to obtain self-propulsion: Flagella of *E. coli* bacteria (Fig. 2a) are put into rotation by motors embedded in the cell wall, exerting a constant force on the cell body (for a detailed mathematical description see for example Reference [16]). The *Caulobacter crescentus* (Fig. 2b) has a single filament whose motor can rotate in both ways, pushing or pulling the cell depending on the rotation direction. The motor of the bacterium *Rhodobacter sphaeroides* (Fig. 2c) turns in only one direction but stops from time to time. Furthermore, the Spiroplasma, helically shaped bacteria with no flagella (Fig. 2d), swim via the propagation of pairs of kinks along the length of the body, which are thought to be generated by contraction of the cytoskeleton. Spermatozoa (Fig. 2e and f) have molecular

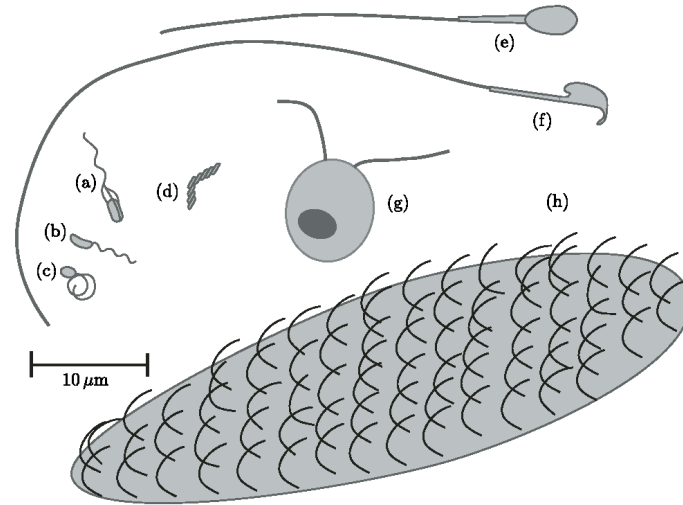


Figure 2: Sketches of microscopic swimmers, to scale. (a) *E. coli*. (b) *C. crescentus*. (c) *R. sphaeroides*, with flagellar filament in the coiled state. (d) Spiroplasma, with a single kink separating regions of right-handed and left-handed coiling. (e) Human spermatozoon. (f) Mouse spermatozoon. (g) *Chlamydomonas*. (h) A smallish *Paramecium*. Figure and caption taken from [15].

motors on their filaments which then move in a coordinated whip-like motion and produce self-propulsion of the cell. Other microorganisms like the *Paramecium*, have many cilia that produce self-propulsion (Fig. 2h). These cilia are much shorter than the cell body, much thicker than bacterial flagella, and have a more complex internal structure.

### 1.2.1 *E. coli* bacteria

Bacteria in general and *Escherichia coli* (*E. coli*) bacteria in particular, are useful and important model systems that allow us to investigate the properties of self-propelled systems at the micro-scales. The model that we use (see chapter 2) is inspired by the real motion of *E. coli* bacteria. Here we therefore shortly present the characteristics of *E. coli* that mostly interest us and that mostly influence our model. For more detailed information see References [17] and [18].

Bacteria are unicellular microorganisms. Their single cell is a prokaryotic cell, which means that in contrary to eukaryotic cells, they do not have a membrane-bound cell nucleus. Their typical size is of the order of the micrometer and they can have different shapes, ranging from spherical shape, to spiral or rod shape. The *E. coli* bacterium has been identified by the German pediatrician Theodor Escherich in 1885. It is one of the most used bacteria in scientific research and one of the best known bacteria, since it can be easily found, and reproduces itself fast in a laboratory environment. *E. coli* bacteria are mainly

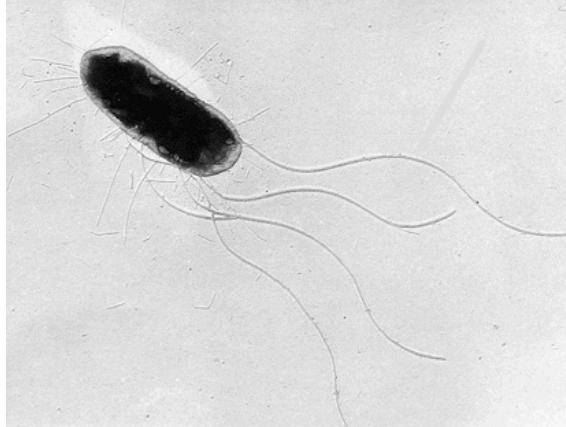


Figure 3: *E. coli* bacterium.

found in the low part of the intestine of warm blood animals, humans included. Although in some cases it can also be the cause of some diseases like peritonitis or pneumonia, *E. coli* bacteria are generally harmful for human beings. They also help in the digestion process and defend from other more dangerous microorganisms.

The shape of the cell body of *E. coli* bacteria is a cigar-shape, or a prolate spheroid, as shown in Figure 3. *E. coli* are approximately  $2\ \mu\text{m}$  long and  $1\ \mu\text{m}$  wide. Flagella, long ( $\sim 10\ \mu\text{m}$ ) and thin ( $\sim 20\ \text{nm}$ ) filaments, are attached at the cell wall. Through molecular motors they are set into rotation, which make the motion and self-propulsion of the bacterium possible. The flagella are put by the motors in directed and synchronized rotation, at a frequency of approximately 100 Hz, such that they form a spinning flagella bundle, which exerts a constant force on the cell body. The cell body, which due to angular momentum conservation rotates in the opposite direction of the flagella at approximately 10 Hz, proceeds than at constant velocity, since at that length scale, as we discuss in more detail in the Section 1.3, inertia is negligible and the velocity of a particle is proportional to the force which is exerted on it. The self-propelled velocity is of the order of magnitude of  $30\ \mu\text{m s}^{-1}$ , which is about 10 cell lengths per second.

This straight motion, called the *run*, is then suddenly and randomly interrupted by a random change in direction of the cell body. This change in direction is called *tumbling*. It is caused by the reverse rotation of one or more flagella. The flagella bundle gets disordered, the cell stops and rotates by a random angle. Afterward the run starts again, and the particle starts again to move in straight motion. The tumbling has an average duration of 0.1 s and a frequency such that the mean free path of the *E. coli* cell is about 10 cell lengths. The bacterium can change direction of motion not only because of the tumbling, but also for other reasons like collisions with other bacteria or with obstacles and hydrodynamics interactions (see Section 1.3.2).

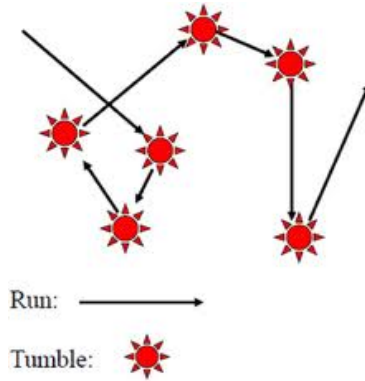


Figure 4: Sketch of the Run-and-Tumble dynamics, taken from [19].

### 1.2.2 Run-and-Tumble motion

*E. coli* bacteria are too small to feel any gradients (like food concentration gradients) in the surrounding environment. They can therefore not move directly to regions with more nutrients, they have to use rather different foraging strategies. *E. coli* bacteria exploit the fact that they can change the tumbling frequency in order to stay longer in zones with more nutrients. In other words, *E. coli* bacteria do not compute space gradients, they rather compute time averages of the food they met on their way. When the time average is low, bacteria tend to have low tumbling frequency, such that a big position change can happen, which can lead to a displacement to a richer zone. On the other hand, when the food concentration is high, and so the time average, the tumbling frequency increases in order to not move far away from that area.

The Run-and-Tumbling motion of *E. coli* bacteria is a particular type of random walk. Here we shortly describe random walks and some of their main properties. For further reading we refer to the book by Klafter and Sokolov [20] and to the review paper by Frey and Kroy [21]. The simplest version of a random walk considers the motion of a walker in one single dimension, where every time step it makes a step of size  $l$  either to the right or to the left, with equal probability. The average position (average over many different walks) at time  $t$  is zero because of left-right symmetry in the problem,  $\langle x(t) \rangle = 0$ . More interesting is the average of the square of the position, also called mean square displacement, which is proportional to the time  $t$ ,

$$\langle x^2(t) \rangle = l^2 t, \quad (1)$$

due to the additivity property of the average and the independence of the random variables, i.e.  $\langle r_i r_j \rangle = l^2 \delta_{i,j}$ . This means that a random walker increases its distance from the starting point much slower than a non-random, sober, clear headed deterministic directed walker, which increases its distance linearly with time and therefore its mean square displacement

increases quadratically with time  $\langle x^2(t) \rangle \sim t^2$ . The first behavior is called diffusive regime, while the latter one is called ballistic regime.

Considering a walker whose step size  $l$  tends to be infinitesimally small,  $l \rightarrow 0$ , and which time step  $\tau$  also tends to be infinitesimally small,  $\tau \rightarrow 0$ , in a way such that  $l^2/\tau$  stays constant, we get the so-called Wiener Process. Since the mean square displacement of the walker is a sum on a large number of independent random variables with finite mean and variance, the central limit theorem ensures that the resulting sum is normally distributed, namely following the Gaussian distribution with variance

$$\sigma^2 = \frac{t}{\tau} l^2. \quad (2)$$

A random walk with step size and time step tending to zero is therefore equivalent to taking at every time step a random variable for the walked distance from a Gaussian distribution. The resulting dynamics is diffusive. This is a very good model for the Brownian Motion, such that often the terms Wiener Process and Brownian motion are used equivalently, although the Wiener Process is the model and the Brownian motion is the observed thermal motion of sufficiently small particles [22, 23].

When displacements are distributed with a power-law  $P(x) \sim x^\alpha$  with  $\alpha \leq 3$ , then mean and variance are no longer finite, the central limit does not hold any more and anomalous diffusion is observed. Such distributions are often called “heavy-tailed” distributions. Anomalous diffusion refers to a mean square displacement which is not linearly proportional to time, but rather proportional to the time to a power  $\gamma$  different from 1,

$$\langle x^2(t) \rangle \sim t^\gamma, \quad \gamma \neq 1 \quad (3)$$

Random walks with heavy tailed distributions of the walking step are called *Levy flights*. Such walks are observed in nature for example in the foraging motion of animals [24].

The Run-and-Tumble motion of *E. coli* bacteria is a random walk with an exponential distribution for the displacements, namely for the run lengths between tumbling events. Since the exponential distribution has finite mean and variance, the central limit theorem ensures that the sum of such displacements will be Gaussian distributed. Run-and-Tumbling particles will therefore diffuse normally,  $\langle x^2(t) \rangle \sim t$ , like Brownian particles, although the diffusion coefficient will be much larger, since Run-and-Tumbling particles are self-propelled and move much faster than Brownian particles. For a more detailed analysis of the Run-and-Tumble motion of bacteria see for example References [25, 26].

### 1.3 Hydrodynamics at the microscale

Self-propelled particles at the micro-scale like *E. coli* bacteria do generally move in fluids like water. Here we introduce the equations that govern the motion of fluids and micro-particles therein. The fundamental equation for the motion of fluids is the Navier-Stokes equation [27]

$$\rho \left[ \frac{\partial \mathbf{v}}{\partial t} + (\mathbf{v} \cdot \nabla) \mathbf{v} \right] = -\nabla p + \mu \nabla^2 \mathbf{v} + \left( \zeta + \frac{1}{3} \mu \right) \nabla (\nabla \cdot \mathbf{v}) \quad (4)$$

with  $\mathbf{v}$  the fluid velocity,  $\rho$  the fluid density,  $p$  the fluid pressure,  $\zeta$  and  $\mu$  viscosity coefficients. The viscosity of a fluid is a measure of the resistance of the fluid to mechanical stresses, and is due to friction between fluid particles. Intuitively, honey has a high viscosity and water a lower one. Assuming the fluid to be incompressible ( $\nabla \cdot \mathbf{v} = 0$ ), which for water is a sufficiently realistic assumption, the Navier-Stokes equation can be simplified and reads then

$$\rho \left[ \frac{\partial \mathbf{v}}{\partial t} + (\mathbf{v} \cdot \nabla) \mathbf{v} \right] = -\nabla p + \mu \nabla^2 \mathbf{v}. \quad (5)$$

The left hand side expresses the inertial forces and is of the order of magnitude of  $\rho v^2/l$ , with  $v = |\mathbf{v}|$  the velocity norm and  $l$  the characteristic system length scale (e.g. bacterium size). The viscous term  $\mu \nabla^2 v$  is of the order of magnitude of  $\mu v/l^2$ . The ratio between them is the Reynolds number, which is defined as

$$\mathcal{R} = \frac{\rho l v}{\mu}. \quad (6)$$

The Reynolds number expresses therefore the ratio between inertial and viscous forces. At high Reynolds number,  $\mathcal{R} \gg 1$ , the fluid motion is turbulent. At low Reynolds number,  $\mathcal{R} \ll 1$ , the fluid motion is laminar.

In the limit of quasi-stationary motion and zero Reynolds number, the inertial term in the Navier-Stokes equation is neglected, which results in the Stokes equation

$$\nabla p = \mu \nabla^2 \mathbf{v}. \quad (7)$$

The Stokes equation is a linear and time independent equation, therefore we get at low Reynolds number the so called hydrodynamic reversibility. This is very nicely shown in the Taylor experiment. In Figure 5, snapshots from an experiment of the New York University are shown [28]. A high viscous fluid is between two transparent cylinders, which can rotate one respect to the other. A red ink drop is inserted into the fluid, and the rotation in clockwise direction (seen from above) starts. The red drop becomes a weak red ring and the rotation stops. Then, the rotation in the other direction starts, and after the same

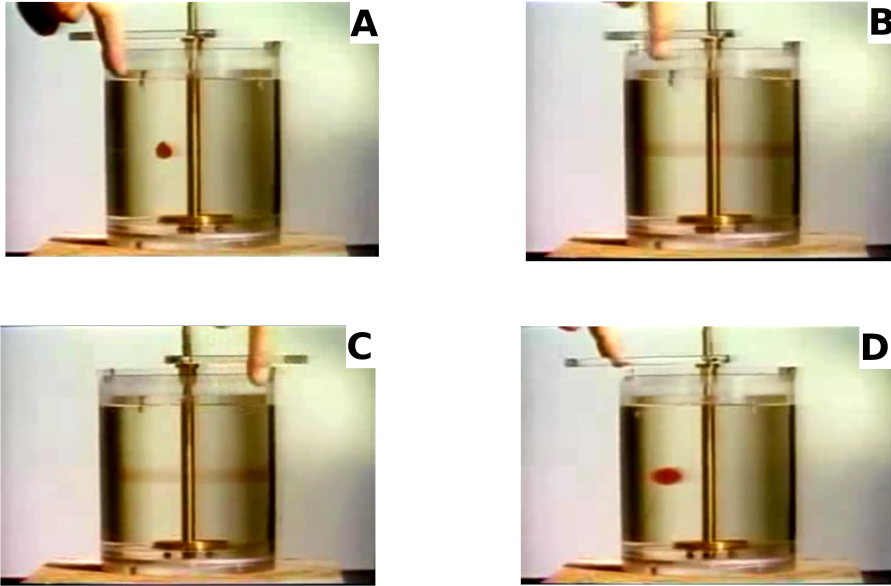


Figure 5: Hydrodynamic reversibility. Snapshots of the Taylor experiment taken from one video of the New York University [28]. A high viscous fluid is between two transparent cylinders, which can rotate one respect to the other. A red ink drop is inserted into the fluid (A). The rotation in clockwise direction (seen from above) starts (B). The red drop becomes a weak red ring and the rotation stops. Then, the rotation in the other direction starts (C). After the same number of rotations the red drop comes together as it was at the beginning (D).

number of rotations the red drop comes together as it was at the beginning. The fluid behaves somehow like a rigid body, where there is no diffusion, like as if every motion of the fluid can be done backwards to restore all particle positions. In the opposite regime, the high Reynolds number regime, also called the turbulent regime, the motion of the fluid particles is extremely chaotic and irreversible.

At low Reynolds number, the velocity of a particle is proportional to the force which is exerted on it. Considering the physical quantities in the Stokes equation, the only physical quantities that we can use to obtain a force are velocity, length and viscosity.

$$F \sim \mu l v \tag{8}$$

In general, the proportionality coefficient between velocity and force is called mobility  $M$

$$v = MF. \tag{9}$$

The mobility coefficient is not a scalar, but a matrix, characterized by the transverse and



parallel mobility coefficients,  $m_{\perp}$  and  $m_{\parallel}$ . Suppose not to have a spheroidal particle but rather an ellipsoidal one, like a prolate spheroid. In that case, if we apply a force in the direction parallel to the main axis of the particle, it will move with a higher velocity than if we apply the same force in the perpendicular direction. The fluid drag in this latter case will be higher. Therefore for the center of mass velocity  $\mathbf{v}$  we can write

$$\mathbf{v} = \mathbf{M} \cdot \mathbf{F} \quad (10)$$

and for the angular velocity  $\boldsymbol{\Omega}$

$$\boldsymbol{\Omega} = \mathbf{K} \cdot \mathbf{T} \quad (11)$$

where  $\mathbf{F}$  and  $\mathbf{T}$  the force and torque acting on it and

$$\mathbf{M} = m_{\parallel} \hat{\mathbf{e}} \hat{\mathbf{e}} + m_{\perp} (\mathbf{1} - \hat{\mathbf{e}} \hat{\mathbf{e}}) \quad (12)$$

and

$$\mathbf{K} = k_{\parallel} \hat{\mathbf{e}} \hat{\mathbf{e}} + k_{\perp} (\mathbf{1} - \hat{\mathbf{e}} \hat{\mathbf{e}}) \quad (13)$$

their translational and rotational mobility matrices [29] and  $\hat{\mathbf{e}}$  the unit vector describing the particle orientation.

A very important and useful result of the theoretical micro-hydrodynamics is the so called Oseen tensor [30]. The velocity field of the fluid produced by a force localized in time and space acting on a point particle can be calculated through the relation

$$\mathbf{v}(\mathbf{r}) = \int \mathbf{G}(\mathbf{r} - \mathbf{r}') \cdot \mathbf{F}(\mathbf{r}') d\mathbf{r}' \quad (14)$$

where  $\mathbf{G}(\mathbf{r})$  is the Oseen tensor which reads

$$\mathbf{G}(\mathbf{r}) = \frac{1}{8\pi\mu r} (\mathbf{1} + \hat{\mathbf{r}} \hat{\mathbf{r}}). \quad (15)$$

Rewriting the field  $\mathbf{v}(\mathbf{r})$  in spherical coordinates  $(r, \theta)$ , we notice that it is the same field which is generated by a sphere moving at constant velocity in a fluid [27]

$$\begin{aligned} v_r &= -v \frac{3R}{2r} \cos \theta = \frac{-F \cos \theta}{4\pi\mu r} \\ v_{\theta} &= +v \frac{3R}{4r} \sin \theta = \frac{F \sin \theta}{8\pi\mu r} \end{aligned} \quad (16)$$

having used the Stokes law which relates force and velocity for a sphere in three dimensions

$$F = 6\pi\mu Rv. \quad (17)$$

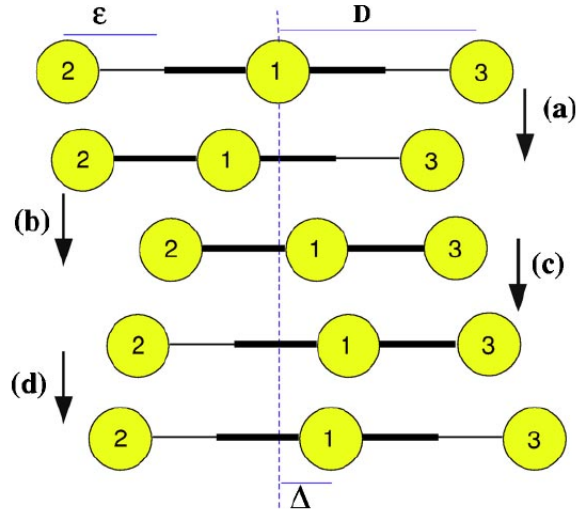


Figure 6: Complete cycle of the proposed nonreciprocal motion of the artificial swimmer, which is composed of four consecutive time-reversal breaking stages: (a) the left arm decreases its length with the constant relative velocity  $W$ , (b) the right arm decreases its length with the same velocity, (c) the left arm opens up to its original length, and finally, (d) the right arm elongates to its original size. By completing the cycle the whole system is displaced to the right side by an amount  $\Delta$ . Figure and caption taken from [31].

We have seen that a particle moving in a fluid generates a velocity field in the fluid itself. This field will influence the motion of other particles if there are any in the fluid. This kind of interaction between particles in fluids is called hydrodynamic interaction and will be discussed in section 1.3.2.

### 1.3.1 Swimming at low Reynolds number

Swimming refers to the motion of self-propelled particles in a fluid like water. When particles are very small, of the order of magnitude of the micrometer like *E. coli* bacteria, the properties of the motion are very different compared to the properties of the motion at larger length scales. Inserting in the definition of Reynolds number typical values for bacteria like *E. coli* swimming in water,  $\rho \simeq 1 \text{ g cm}^{-3}$ ,  $\mu \simeq 10^{-3} \text{ Pa s}$  ( $\text{Pa s} = \text{kg}/(\text{s m})$ ),  $v \simeq 10 \text{ } \mu\text{m s}^{-1}$ ,  $l \simeq 1 \text{ } \mu\text{m}$ , we get  $\mathcal{R} \simeq 10^{-5}$ , while on the other hand, for humans swimming in water ( $l \simeq 1 \text{ m}$ ,  $v \simeq 1 \text{ m s}^{-1}$ ) we get  $\mathcal{R} \simeq 10^6$ . We therefore notice that for small particles like bacteria, the motion is laminar and without inertia, while for human beings in water inertia is not negligible.

Because of the hydrodynamic reversibility, it turns out that swimming, namely moving forward in a fluid, is very different at low Reynolds numbers [32]. A scallop, which at intermediate Reynolds number swims just opening and closing its shell at different veloci-

ties, will not swim at low Reynolds number. This fact is known as “Scallop theorem” [32]. “Any attempt to move by imparting momentum to the fluid, as is done in paddling, will be foiled by the large viscous damping” [15]. At low Reynolds number a motion with only one degree of freedom is not sufficient to obtain a net displacement. What is needed is at least a cyclic degree of freedom, like the angle of a spinning flagella bundle of *E. coli* bacteria. Other minimal artificial swimmers use two degrees of freedom [31]. Three spheres confined in one dimension are connected by two extensible arms, whose lengths are the two degrees of freedom. With a cyclic nonreciprocal deformation that breaks time and space symmetry, shown in Figure 6, the micro-swimmer moves in a predetermined direction.

### 1.3.2 Hydrodynamic Interactions

When one particle moves in a fluid, it is intuitive that it will move the fluid which is around it. Suppose that we have at a certain distance from the moving particle an other particle which is not moving. The position and the orientation of this second particle is affected by the motion of the fluid, and it can start to move because of the motion of the fluid. Therefore the motion of one particle affects the motion of other particles, where the medium that carries the interaction is the fluid. This interaction is what is known and called as hydrodynamic interaction. Here we briefly describe what hydrodynamic interactions are and how they can be taken into account. A more exhaustive description of hydrodynamic interactions can be found for example in the review of Lauga and Powers [15].

Suppose to have one spherical particle that moves with constant velocity in a fluid at low Reynolds number because of a constant force acting on it. We have already discussed that at low Reynolds number, when viscosity dominates on inertia, the velocity of a body is proportional to the force which is exerted on it. The velocity field of the fluid is given by eq.(16). Other particles in the fluid which were at rest will stay at rest respective to the fluid and move respective to the laboratory frame accordingly to the fluid velocity. If many particles are moving because of external forces, than the fluid motion will be a sum of Oseen tensors, and the motion of every particle will be affected by the motion of the others.

Self-propelling particles move not because of an external force. They are force and torque free. The motion of flagella pushes bacteria forward, like the motion of a propeller moves a ship. The resulting solvent velocity field is not the one given by the Oseen tensor. Instead, a dipole expansion of the Oseen tensor can be performed to obtain the right velocity field produced by one swimming micro particle. The flagella of an *E. coli* bacterium rotate and push the solvent away from the cell body. The cell body moves and pushes also the fluid away of the cell body. The resulting flow field is a dipolar field, with the fluid going away from the head and tail of the particle, and coming in at the sides of

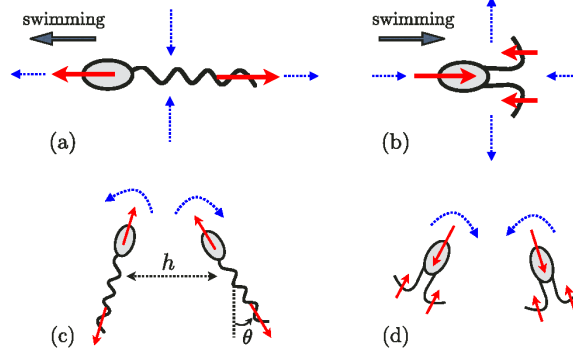


Figure 7: Hydrodynamic interactions between The flow field created by a swimmer at low Reynolds number. (a) Cells which are pushers induce a flow field directed away from the cells along their swimming direction (repulsion) and a flow field directed toward the cells along their sides (attraction) (red solid arrows represent local forcing from the cell on the surrounding fluid, and blue dotted arrows represent the flow direction in the surrounding fluid); (b) Pullers induce an attractive flow field along their swimming direction and a repulsive flow field along their sides (in figures (a) and (b) the swimming direction of the cell are indicated with a thick gray arrow); (c) two pushers on a converging course reorient each other, tending toward a configuration with cells parallel and swimming side-by-side ( $h$  is the separation distance between the cells, and  $\theta$  is the angle between the cell direction and the direction normal to their separation); (d) two pullers on a diverging course reorient each other, tending toward a configuration in which the cells are antiparallel, swimming away from each other. (Figure and caption taken from [15]).

the particle. This kind of flow fields is produced by so called *pushers* like *E. coli* bacteria. The algae *Chlamydomonas*, instead, is a *puller*. It pulls the fluid at its front and at its back, while the fluid goes away from the cell at its sides. The dipole  $p$  is defined to be positive for pushers and negative for pullers.

Describing the swimming particle by the vector  $\hat{\mathbf{e}}_j$  and the dipole  $p$ , the field reads

$$\mathbf{V}_{i,j}^h(\hat{\mathbf{e}}_j, \hat{\mathbf{r}}) = \frac{p}{8\pi\mu} [3(\hat{\mathbf{e}}_j \cdot \hat{\mathbf{r}})^2 - 1] \frac{\hat{\mathbf{r}}}{r^2} \quad (18)$$

Actually the second particle (described by the vector  $\hat{\mathbf{e}}_i$ ) at distance  $\mathbf{r} = \mathbf{r}_i - \mathbf{r}_j$  from the first one, feels not only the velocity field produced by the first particle, but also the vorticity, which causes the rotation of the second particle, even if it is a sphere. The angular velocity induced on the second particle is given by

$$\boldsymbol{\Omega}_{i,j}^h(\hat{\mathbf{e}}_j, \hat{\mathbf{r}}) = \boldsymbol{\Omega}^\infty + \lambda \hat{\mathbf{e}}_i \times (\hat{\mathbf{e}}^\infty \cdot \hat{\mathbf{e}}_i) \quad (19)$$

with vorticity  $\boldsymbol{\Omega}^\infty = (\nabla \times \mathbf{V}_{i,j}^h)/2$ , strain tensor  $\hat{\mathbf{e}}^\infty = (\nabla \mathbf{V}_{i,j}^h + (\nabla \mathbf{V}_{i,j}^h)^T)/2$ . and  $\lambda = (\alpha^2 - 1)/(\alpha^2 + 1)$ , with  $\alpha$  the aspect ratio [29].

## 1.4 Properties of self-propelled particles

Self-propelled particles, continuously convert energy into directed motion, resulting in many interesting properties which can be very different from properties of Brownian particles. Here we introduce some of these fascinating effects.

A difference between equilibrium systems and self-propelled particle systems is in the interaction rule among particles. Considering the system made by particles only, and not the environment, momentum is not conserved in collisions among self-propelled particles. And since we are not at the thermodynamic equilibrium, also the time reversal symmetry is not conserved. In chapter 4 we present the upstream swimming phenomenon of self-propelled particles in micro-channels with Poiseuille flow. Unlike passive tracers, self-propelled particles aggregate at the channel walls and swim there against the solvent flow. As we will discuss in chapter 5, self-propelled particles show ratchet phenomena, i.e. rectification of their chaotic motion into directed motion, in a static asymmetric potential. Passive Brownian particles would not. Another interesting property is the non-Boltzmann space distribution in the presence of an energy potential and the related cluster formation. Particles like gas molecules at thermodynamic equilibrium, in the absence of any attraction force, are homogeneously distributed in space. Any concentration gradient would lead to a particle flux which would diminish the gradient itself and restore the homogeneous density. This is known as first Fick law, after A. E. Fick (1829-1901) German physician and physiologist, who introduced it in 1855, and reads

$$J = -D\nabla c, \tag{20}$$

where  $J$  is the flux,  $D$  the diffusion coefficient, and  $c$  the concentration. Active particles, in contrast, do not always show homogeneous density distributions. The self-propulsion alone, without any attraction force between particles, is sufficient for cluster formation. The cluster formation increases with particle self-propelling velocity and aspect ratio. Experimental observation of cluster formation of self-propelled bacteria are reported for example in References [7, 33–36].

In the absence of external potentials, Brownian particles are homogeneously distributed in space. In the presence of an external potential, macroscopic observables like the particle density  $\rho(x)$  of Brownian particles follow the Boltzmann distribution

$$\rho(x) \sim e^{-E(x)/(k_B T)}, \tag{21}$$

where  $E(x)$  is the potential energy,  $k_B$  the Boltzmann constant and  $T$  the temperature. Fluctuations from these mean values are possible. The density distribution of self-propelled particles does not follow the Boltzmann distribution [37]. Already in the absence of an

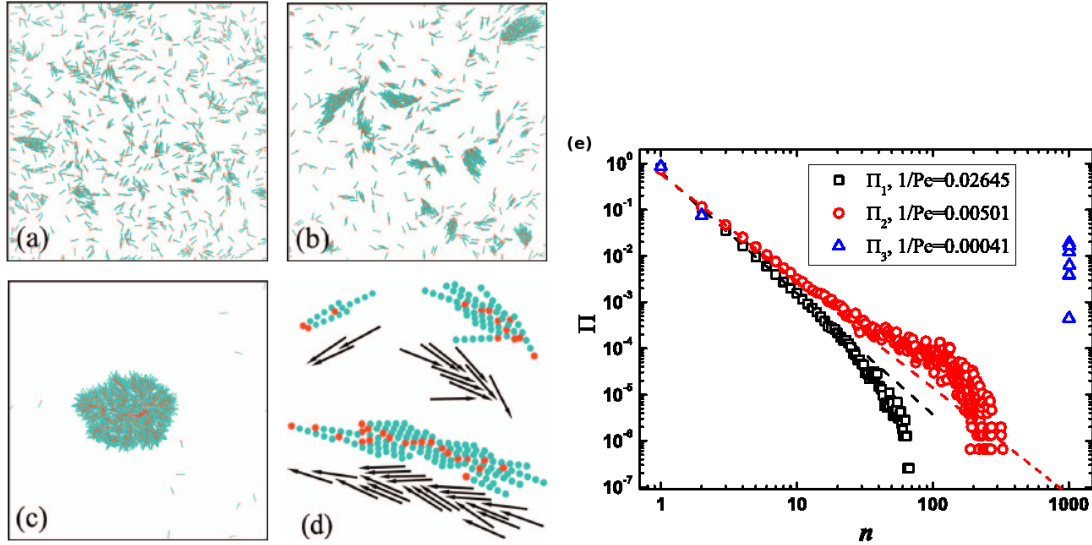


Figure 8: Cluster formation of self-propelled rods. Simulation snapshots at increasing Peclet number (a-c), clusters of size  $n = 3, 10, 22$  (d), and cluster size distribution (e). Figure taken from [38].

external potential, where the Boltzmann distribution would be simply a constant distribution, active particles can form clusters resulting in non-uniform density profiles.

Moreover, the stronger the potential, i.e. the stronger the applied forces are, the worse self-propelled particles follow the Boltzmann law [37]. This can be described with a simple example. Suppose to have a single self-propelled particle confined in one dimension. The particle moves straight and changes its direction of motion at random times. In the presence of a flat potential, the particle distribution will be flat and will therefore satisfy the Boltzmann law. On the other hand, in the presence of potential barriers, which are so steep that the particles can not overcome them, i.e. the external force is stronger than the self-propulsion force, the density profile will strongly deviate from the Boltzmann distribution. The density profile shows two strong peaks close to the potential walls. This happens since a particle moving in one direction reaches the potential wall and stays there not moving, since the self-propulsion force keeps the particle close to the wall until a random change in the direction of motion happens. The frequency of the reorientation events, i.e. the Peclet number, determines the time for which particles stay close to the walls and therefore the density profile.

## 1.5 Theoretical models

There are several theoretical model approaches to study self-propelled particles. Most of them are based on standard molecular dynamics simulations. In molecular dynamics

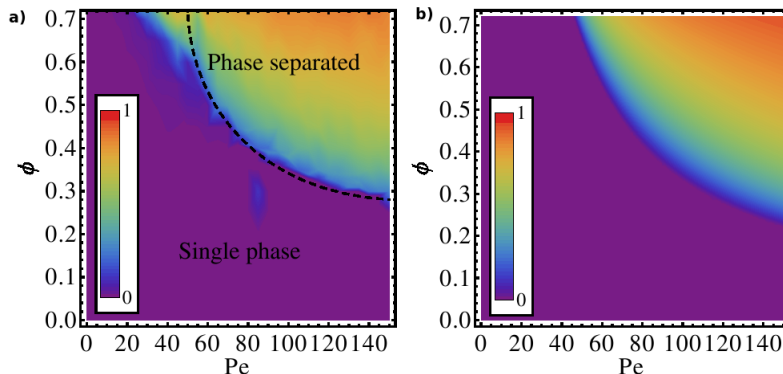


Figure 9: Phase diagram (Density  $\phi$  - Peclet number  $Pe$ ) for the cluster formation of self-propelled spheres. Numerical result (a) and analytical prediction (b). Figure taken from [42].

simulations, the motion of particles like atoms or molecules is simulated by numerical integration of the Newton's equation of motion with specific inter-particle forces. In self-propelled particle simulations, the particles are constantly subjected to the self-propulsion force and are therefore intrinsically not at thermodynamic equilibrium. It is worth noting that also without self-propelling force one can perform off-equilibrium molecular dynamics simulations like using passive particles in a temperature gradient or in shear flow. The particle dynamics is simulated starting from a (usually random) initial configuration. Interesting collective phenomena emerge, which can be usually hardly predicted *a priori* (otherwise the simulation would not be useful). Self-propelled particle models are mainly used to model the motion of several groups of animate and inanimate organisms and objects ranging from bacteria, birds and fish, to cars and pedestrians [1, 11, 39]. Self-propelled particle models are usually individual-based off-lattice models, where the particles are free to move in the continuum space.

The probably best known self-propelled particle model is the Vicsek model [40, 41]. In that model, particles proceed at constant velocity in the two-dimensional space and are only subjected to an alignment force, which tends to align velocity directions of neighboring particles. Decreasing the noise, a phase transition from zero average velocity to finite net transport is found.

Order and alignment can emerge also from other models, like rod-like models, which do not have explicit alignment forces. Rod-like models consider self-propulsion and excluded volume forces only, and have been used, for example, to study the clustering of self-propelled rods as a function of system parameters, finding that high particle density and high aspect ratio are needed to have phase separation [33, 43]. A similar phase space behavior has been also found for the clustering of beating flagella [38]. Figure 8a-c shows

simulation snapshots at increasing Peclet number (which is the ratio between ballistic motion and diffusive motion, i.e. between self-propulsion and noise). We notice that cluster formation increases with Peclet number, as also evident from the cluster size distribution data of Figure 8e. Other numerical as well as analytical continuum theory studies show how clustering is also possible for self-propelled spheres, investigating the phase space of particle density and Peclet number [42, 44–49]. Figure 9 shows a comparison between numerical simulations and analytical predictions for the regions in the phase space, in which a system of self-propelled spheres is homogeneous or shows phase separation (clustering).

The variety of self-propelled particle models is of course even more rich than shortly presented here. Without going into detail, it is worth mentioning that there are models with attraction forces only [50], or with attraction, repulsion and alignment forces together [51], where eventually these different forces are associated with different interaction radii. Not only continuum-space models have been used, but also discrete-space, lattice models have been used to study clustering phenomena [52]. Moreover, there are also several types of leader-follower models [53], as well as predation and escape models [54] and evolutionary models [55].



---

## 2 Model

### 2.1 Our self-propelled particle model

We use a minimal model for self-propelling particles, based on the models used in previous works [56, 57]. Since previous simulations of self-propelled particles in two dimensions [56] were in very good agreement with experimental results [58], and since many experimental setups are quasi two dimensional, we also perform our simulation study in two dimensions.

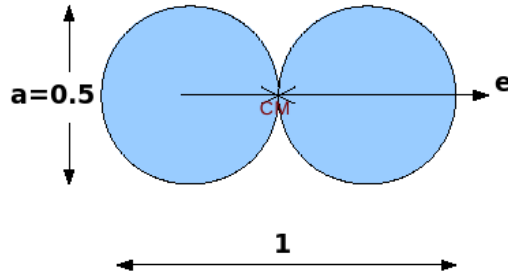
The model aims to mimic the geometry and the motion of an *E. coli* bacterium [17], but without loosing in generality, we model each particle with  $n$  rigidly connected force-beads of diameter  $a$ . The distance between two consecutive beads is  $a$ , such that the length of the particle is  $l = na$ , the width is  $a$  and the length to width aspect ratio is  $\alpha = l/a = n$ . The center of mass of the particle is at position  $\mathbf{r}_i$  and is subjected to a self-propelling force along its main axis  $\hat{\mathbf{e}}_i$  (see Figure 10 for a sketch of a particle with  $n = 2$  beads). Particles dynamics is described by mobility equations, see eq.(10) and eq.(11), assuming the limit of negligible inertia at low Reynolds numbers at the microscale. The force  $\mathbf{F}_i$  acting on the  $i$ -th particle is a sum of the mechanical interactions with the other particles and the self-propelling force,

$$\mathbf{F}_i = f_0 \hat{\mathbf{e}}_i + \sum_{j \neq i} \sum_{\beta, \gamma} \mathbf{f}(\mathbf{r}_i^\beta - \mathbf{r}_j^\gamma) \quad (22)$$

where  $f_0$  is the self-propelling force, the indexes  $\beta$  and  $\gamma$  run over the  $n$  force-beads and  $\mathbf{f}(\mathbf{r})$  is a repulsive force that we choose of the form

$$\mathbf{f} = \frac{A}{r^{13}} \hat{\mathbf{r}} \quad (23)$$

namely the repulsive part of the Lennard-Jones potential, using a cutoff for  $r > 3$ . The coefficient  $A$  is chosen in a way such that two particles facing head to head have their front beads at distance  $a$  ( $A = a^{13}$ , since imposing  $\mathbf{f}(a) = f_0$ , it follows  $A = f_0 a^{13} \sim a^{13}$ ). The

Figure 10: Model particle formed by  $n = 2$  force-beads.

corresponding torque generated by mechanical interactions reads

$$\mathbf{T}_i = \sum_{j \neq i} \sum_{\beta, \gamma} (\mathbf{r}_i^\beta - \mathbf{r}_i^{\text{cm}}) \times \mathbf{f}(\mathbf{r}_i^\beta - \mathbf{r}_j^\gamma) \quad (24)$$

where  $\mathbf{r}_i^{\text{cm}} = (\mathbf{r}_i^n + \mathbf{r}_i^0)/2$  is the particle center of mass. The equations of motion are integrated with a second-order Runge-Kutta method with a time step  $\Delta t = 10^{-3}$  (if not stated differently in the result sections).

### Cell list algorithm

To avoid the computation of all the distances between all pairs of particles, and so to speed up the simulation, we use “cell lists”. At every time step the space is divided in cells of a fixed size (we typically use as size the cutoff-radius of the interaction-potential). To every cell corresponds a list in which all particles belonging to that cell at that time are stored. Then, for all the particles in one cell, only distances (and so forces) with the particles in the same cell and in neighboring cells are computed. Without using the cells, one needs to compute at every time step the distances between all the particles, which are  $\sim N^2$ . Using cell lists, the distances to compute are  $\sim N$ . The computation time increases therefore quadratically with the number of particles without using the cell lists, while scales linearly with the number of particles using them.

### Reduced units

In numerical simulations the choice of a reduced unit reference system has to be done in order to be able to interpret the results of the simulations. We use the following reduced units:

- $2a$ , twice the particle width as unit of length
- $m_{\parallel}$  as unit for mobility

- $f_0$ , the standard self-propelling force, as unit of force

It follows that

- $v = f_0 m_{\parallel}$ , the standard self-propelling velocity, is the unit of velocity
- $t = 2a/v$  is the unit of time.

Physical values suitable for example for *E. coli* bacteria can be obtained choosing  $2a = 3 \mu\text{m}$ ,  $f_0 = 0.5 \text{ pN}$ ,  $m_{\parallel} = 60 \mu\text{m s}^{-1} \text{ pN}^{-1} \Rightarrow t = 0.1 \text{ s}$ ,  $v = 30 \mu\text{m s}^{-1}$ .

The mobility values are chosen to describe a prolate spheroid,  $m_{\perp} = 0.87 m_{\parallel}$  and  $k_{\perp} = 4.8 m_{\parallel}$ , values obtained from the general equations [29]

$$m_{\perp} = \frac{1}{32\pi\mu l} \frac{2e + (3e^2 - 1)L}{e^3} \quad m_{\parallel} = \frac{1}{16\pi\mu l} \frac{-2e + (1 + e^2)L}{e^3} \quad (25)$$

$$k_{\perp} = \frac{3}{32\pi\mu l^3} \frac{-2e + (1 + e^2)L}{e^3(2 - e^2)} \quad k_{\parallel} = \frac{3}{32\pi\mu l^3} \frac{2e - (1 + e^2)L}{e^3(2 - e^2)} \quad (26)$$

with the constants

$$L = \log \frac{1 + e}{1 - e} \quad \text{and} \quad e = \sqrt{1 - 1/\alpha^2} \quad (27)$$

and  $\alpha$  the particle length to width aspect ratio.

## 2.2 Run-and-Tumble dynamics

The dynamics described until now is completely deterministic, particles would move on straight lines until they collide with other particles or with a wall. Inspired by the real motion of *E. coli* bacteria (see Section 1.2.1), we model the Run-and-Tumble motion [25, 26]. The straight motion of the run state, is interrupted by the tumbling event. The tumbling event consists in a random torque, which leads to a random rotation by an angle  $\eta \in [-\pi, \pi]$  if the particle is free to rotate. This rotation starts at random times and has a fixed duration  $\tau_{\text{tb}}$ . The time intervals and so the traveled distances between the ending of a rotation and the starting of the new rotation are exponentially distributed,  $e^{-\nu t}$ , leading to a Poisson distribution of the number of rotating events in a time unit, with mean frequency  $\nu$ , and  $\nu_{\text{eff}} = \frac{\nu}{(1 + \nu\tau_{\text{tb}})}$  an effective frequency considering that  $\nu$  alone does not consider the duration of the rotation itself. During the tumbling event of duration  $\tau_{\text{tb}}$  the self-propelling force is deactivated. The rotational diffusion coefficient (of a single free swimming particle) reads

$$D_r = \nu_{\text{eff}} \frac{(2\eta)^2}{12} \quad (28)$$

where  $\frac{(2\eta)^2}{12}$  is the mean square angle by which the particle is rotated, since the angle is uniformly distributed between  $\pm\eta$ .

We choose  $\eta = \pi$ ,  $\tau_{\text{tb}} = 1$  and  $\nu = 10^{-1}$ . These are realistic values for *E. coli* bacteria, for which the tumbling time is 0.1 s and the tumbling frequency 1 Hz [17]. This means that in average every  $10/\Delta t$  integration steps a tumbling event of fixed duration  $1/\Delta t$  integration steps occurs. The rotational diffusion coefficient results to be  $D_r = 0.3$  and the Peclet number at self-propelling velocity  $v = 1$  is  $Pe = \frac{v}{lD_r} = 3.3$ .

Defining a state variable  $\theta$  which assumes the value  $\theta = 0$  in the run state and the value  $\theta = 1$  in the tumbling state, the force on the  $i$ -th particle can be written as

$$\mathbf{F}_i = f_0 \hat{\mathbf{e}}_i (1 - \theta_i) + \sum_{j \neq i} \sum_{\beta, \gamma} \mathbf{f}(\mathbf{r}_i^\beta - \mathbf{r}_j^\gamma) \quad (29)$$

and the torque reads

$$\mathbf{T}_i = \mathbf{T}_r \theta_i + \sum_{j \neq i} \sum_{\beta, \gamma} (\mathbf{r}_i^\beta - \mathbf{r}_i^{\text{cm}}) \times \mathbf{f}(\mathbf{r}_i^\beta - \mathbf{r}_j^\gamma) \quad (30)$$

where  $T_r$  is the random torque value which is applied in the tumbling state.

### Active-Brownian-Particles

Although most of our results are obtained with Run-and-Tumbling particles, we do also compare some of our results with Active-Brownian-Particles [59]. The motion of Active-Brownian-Particles is similar to the dynamics of *passive*-Brownian-particles. Instead of having two different states as Run and Tumbling, rotational noise and self-propulsion are both always present.

We model Active-Brownian-Particles applying at every time step a random torque on the particle and keeping the self-propulsion always activated. The intensity of the random torque is such that the rotational diffusion of a single Active-Brownian-Particle equals the rotational diffusion of a single Run-and-Tumbling particle. Further comparison between Run-and-Tumbling and Active-Brownian-Particles can be found for example in a work by Cates and Tailleur [60], where they often result in similar behavior.

### 2.3 Channels with and without Poiseuille flow

Confinement in micro-channels is also considered due to the large number of applications as those in microfluidic devices. Two dimensional channels are described by two parallel walls (at  $x = \pm L$ , with relative distance  $L_x = 2L$ , length  $L_y$ ) with periodic boundary conditions along  $y$ . The steric repulsion of a swimmer with the channel walls is obtained as a soft repulsion, like in Eq. 23, between the force centers of the swimmer and their

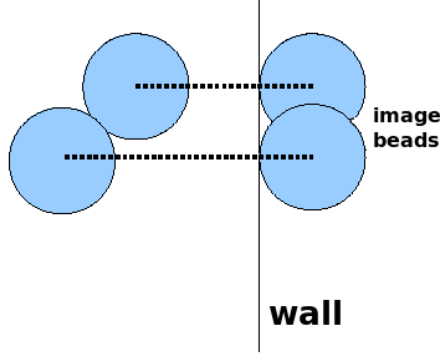


Figure 11: Interaction with the walls. For each force-bead of the particles (here  $n = 2$ ) the interaction with an image bead behind the wall is computed.

images behind (by a distance  $a/2$ , see Figure 11) the considered wall:

$$\begin{cases} F_{i,x}^{wall} = \sum_{\beta} A[x_i^{\beta} \pm (L + \frac{a}{2})]^{-13} \\ F_{i,y}^{wall} = 0 \end{cases} \quad (31)$$

where obviously the  $\pm$  is a  $-$  for the wall on the right and is a  $+$  for the wall on the left.

We may include channel flow in our simulation. We implement an implicit solvent, adding to the translational and rotational velocities of each particle the velocity and the vorticity of the flow:

$$\begin{pmatrix} \mathbf{V}_i \\ \boldsymbol{\Omega}_i \end{pmatrix} = \begin{pmatrix} \mathbf{M}_i & 0 \\ 0 & \mathbf{K}_i \end{pmatrix} \cdot \begin{pmatrix} \mathbf{F}_i \\ \mathbf{T}_i \end{pmatrix} + \begin{pmatrix} \mathbf{V}^f \\ \boldsymbol{\Omega}^f \end{pmatrix} \quad (32)$$

The flow is considered to be of parabolic Poiseuille profile:

$$\mathbf{V}^f = V_0 \left(1 - \frac{x^2}{L^2}\right) \hat{\mathbf{y}} \quad (33)$$

with a vorticity field, which takes the form [29, 57]

$$\boldsymbol{\Omega}^f = \frac{V_0 x}{L^2} [1 + \lambda(2e_x^2 - 1)] \hat{\mathbf{z}} \quad (34)$$

where  $e_x$  is the  $x$ -component of the particle orientation  $\hat{\mathbf{e}}$  and  $\lambda = (\alpha^2 - 1)/(\alpha^2 + 1)$ , such that  $\lambda = 1$  for infinite aspect ratio  $\alpha$  (needles) and  $\lambda = 0$  for spheres [29].

In Chapter 5 we describe the motion of Run-and-Tumble particles in micro-channels with an asymmetric ratchet-like wall structure. In that case, the walls are formed by force-

beads fixed in space. These force-beads are like the one used for the particles and so the wall-particle interaction is like the particle-particle interaction described in the previous section.

### **Hydrodynamic Interactions between particles**

Here we described the interaction between solvent flow and particles. This is the only hydrodynamic interaction that we consider in our model, we neglect the effect that particles have on the solvent and so hydrodynamic interaction between particles themselves (see section 1.3.2). The effect of hydrodynamic interactions between particles themselves is certainly very interesting and has shown to be of relevance in several systems. However, previous works indicate that the role of hydrodynamic interactions between particles leading to cluster formation, or between wall and particles is negligible in comparison with steric interactions, in particular for elongated particles. Numerically this has been tested with two approaches. One is the model here employed [57] where the presence of effective hydrodynamic interactions can be included or not. A second approach considers an explicit solvent particle based method (multiparticle collision dynamics) where hydrodynamic interactions can be easily switched on and off [61, 62]. Furthermore, experimental studies of two independent groups [14, 36] compare their results with minimal models in which HI are not included and obtain good agreements. We therefore believe that it is justified to employ a minimal model in which hydrodynamic interactions are disregarded. For these reasons and also for computational advantage we do not consider hydrodynamic interactions between particles in the simulations used to obtain the results presented here. Further investigation about the effects induced by hydrodynamics will be certainly of interest, although we do not expect qualitative modification of our main conclusions.

---

### 3 Diffusion properties of Run-and-Tumbling particles

Here we investigate the dynamics of self-propelled particles in bulk. This is performed in a two dimensional box geometry with periodic boundary conditions. We study the behavior of the translational- and rotational diffusion coefficient as a function of particle aspect ratio, self-propelling velocity and number density.

#### 3.1 Introduction

The study of dynamical quantities like translational and rotational diffusion coefficient is of crucial importance for a complete characterization of both passive and active rod systems. For active particles, the dynamical properties, in particular the dependence of translational and rotational diffusion coefficients on system parameters like particle density, as well as their dependence on each other, have not been exhaustively studied yet.

The translational diffusion coefficient or diffusivity  $D$  is defined by the long-time limit of the particle mean square displacement,

$$\lim_{t \rightarrow \infty} msd(t) = \lim_{t \rightarrow \infty} \frac{1}{N} \sum_{i=1}^N |\mathbf{r}_i(t - t_0) - \mathbf{r}_i(t_0)|^2 = 2dDt \quad (35)$$

where  $\mathbf{r}_i(t)$  is the position of the  $i$ -th particle at time  $t$  and  $d$  is the dimension of the space. The translational diffusion coefficient describes how fast particles diffuse, e.g. how fast they randomly move away from a fixed point in space. Typically, the mean square displacement increases initially quadratically with time. This behavior is also called ballistic regime. After a time  $\tau_b$ , it shows a crossover to the so-called diffusive regime, where the mean square displacement increases linearly with time. Imposing the equality of the diffusive ( $4Dt$ ) and ballistic ( $v^2t^2$ ) displacement, we get the relation between the diffusion coefficient and the crossover time  $\tau_b = 4D/v^2$ . Alternatively, the Green-Kubo relations can be employed to

characterize the diffusivity using the velocity auto-correlation function  $C_v(t) = \langle \mathbf{v}(0) \cdot \mathbf{v}(t) \rangle$

$$D = \frac{1}{3} \int_0^\infty dt C_v(t). \quad (36)$$

Similarly to the diffusivity, the rotational diffusion coefficient  $D_r$  is defined as

$$\lim_{t \rightarrow \infty} \frac{1}{N} \sum_{i=1}^N |\theta_i(t - t_0) - \theta_i(t_0)|^2 = 2D_r t \quad (37)$$

where  $\theta_i \in \mathbb{R}$  is the angle which defines the orientation of the particles. In analogy with the diffusivity, it tells how fast particles rotate and randomize their initial orientation, and  $\tau_r$  is the time after which the time dependence of the square angle is linear.

### Passive rods

The translational and rotational diffusion coefficients for a passive Brownian sphere of radius  $r$  in three dimensions are well known and can be obtained by solving the Stokes equation [27],

$$D = \frac{k_B T}{6\pi\mu r} \quad \text{and} \quad D_r = \frac{k_B T}{8\pi\mu r^3}, \quad (38)$$

with fluid viscosity  $\mu$ . From these expressions, the diffusion coefficients for single passive Brownian rods can be derived [63], which state that the translational diffusion coefficient decreases with rod length and the rotational diffusion coefficient decreases with the cube of the rod length

$$D \sim l^{-1} \quad \text{and} \quad D_r \sim l^{-3} \quad (39)$$

for sufficiently long rods. The dynamics of passive rods as a function of their number density and their length has been widely studied [64–72]. The Onsager theory for liquid crystals [73] predicts the isotropic-nematic transition for infinitely thin rods of length  $l$  at the critical density

$$\rho_c = 3\pi/2l^2. \quad (40)$$

For passive infinitely thin rods in the isotropic phase, the Doi-Edwards theory [74] predicts a decrease of the rotational diffusion with density and particle length

$$D_r \sim \rho^{-2} l^{-9}. \quad (41)$$

Results of two-dimensional simulations [69] and experimental studies [66] of the rotational diffusion as a function of density are in agreement with this theory. In Reference [66] the dependence on the rod length is also measured, but the reported dependence  $\rho \sim l^{-5.7}$  is in disagreement with the Doi-Edwards theory. This decrease of the rotational diffusion



with length and density is reasonable, since two long particles will hinder each other in the rotational motion. The longer the particles are, the smaller is the angle the particles can rotate without colliding.

The translational diffusion is expected from Enskog theory (see page 204 of Reference [75]) to decrease with particle density

$$D \sim 1/\rho \quad (42)$$

which is valid in the dilute regime. In simulation studies,  $D$  is observed to decrease at low density in agreement with the Enskog theory and then to increase at higher densities [70], in agreement with the theory developed by Frenkel and Maguire [76], which predicts

$$D \sim \rho^{1/2} \quad (43)$$

at higher densities. This happens since at high density the rotation of the particles is suppressed by collisions, particles are in the nematic phase and rather move on straight paths.

### Active rods

Active particles behave very differently than passive ones, giving rise to interesting collective phenomena like swarming [1]. The isotropic-nematic transition happens at lower density than for passive rods [47, 77]. Experimental studies show that the translational diffusion decreases with particle density eventually leading to caging phenomena [78–80]. The translational diffusion coefficient of passive Brownian particles  $D_p$  becomes for active particles [81–83]

$$D = D_p + v_e^2/4D_r, \quad (44)$$

where  $v_e^2/D_r \gg D_p$ , so that the translational and rotational diffusion coefficients of active particles are inversely proportional to each other

$$D \sim v_e^2/D_r. \quad (45)$$

Note that the effective velocity  $v_e$  in eq.(45) is the velocity at which particles really move. This corresponds to the self-propelling velocity  $v$  for single-particle simulations, while it is the sum of self-propelling velocity and collisions with other particles in dense systems.

In the next sections we will measure translational and rotational diffusion coefficients as well as the effective velocity showing that eq.(45) is indeed not only valid for single-particle simulations but also for dense systems of low aspect ratio particles.

The fact that  $v^2/D_r \gg D_p$  justifies to use a model for which the translational diffusion

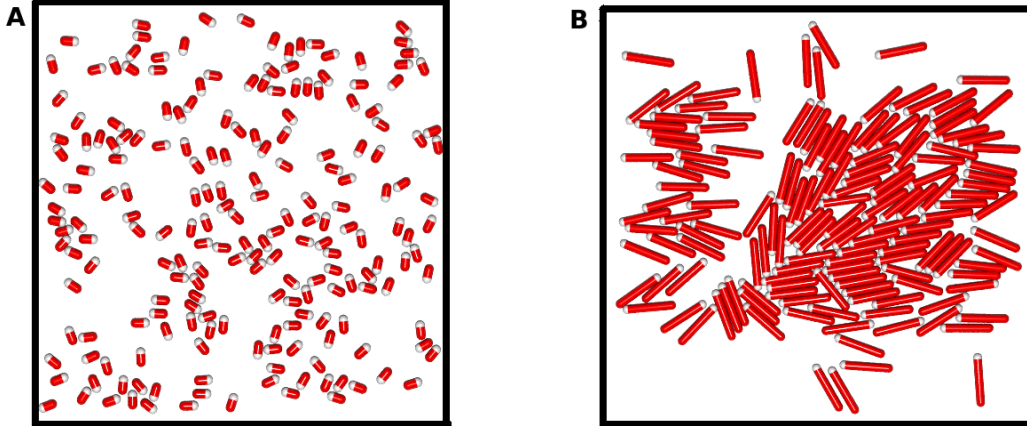


Figure 12: (Color online) Snapshots of simulations: particle length to width aspect ratio  $\alpha = 2$  (A),  $\alpha = 6$  (B). Particle number density  $\rho = N\alpha/2L^2 = 1$ .

of passive particles is zero. By construction of our model, for single-particle simulations,  $D$  and  $D_r$  do not depend on particle length, they depend only on particle velocity. For particles of aspect ratio  $\alpha = 1$  (spheres) the rotational diffusion coefficient is a constant and does not depend on any other parameter as density or self-propelling velocity. This model allows to study better the density effects on the diffusion coefficients. We investigate the diffusion coefficients in units of single-particle coefficients (at self-propelling velocity  $v = 1$  and tumbling frequency  $\nu = 0.1$  - mean free path  $\lambda = 10$ ), which we denote  $D_0$  and  $D_{r,0}$  respectively for translational and rotational diffusion.

We simulate the motion of run-and-tumbling particles of the same type (one component systems). We study the diffusion coefficients varying the particle aspect ratio, the particle self-propelling velocity and the particle density. The tumbling frequency is kept constant at the standard value of  $\nu = 0.1$ . Simulation snapshots are shown in Figure 12. Figure 12a shows an isotropic, non-clustering system of active particles of aspect ratio  $\alpha = 2$ , while in Figure 12b we notice alignment and cluster formation for longer particles ( $\alpha = 6$ ). In order to better understand the effects in the diffusion properties induced by the active character of the particles, we study both particles with self-propelled motion and passive particles. Note though that our model there is no translational diffusion at zero velocity. In this limit the model is not really properly defined since particles only rotate and eventually their centers of mass could move because of collisions with other particles induced by the rotations. Our model describes the motion of self-propelling run-and-tumbling rod-like particles, for which the Brownian noise is negligible.

Typical measures of the mean square displacement are shown in Figure 13. There, we observe that with increasing particle density the mean square displacement decreases, since more particles lead to more collisions and less displacement. We also notice that increasing

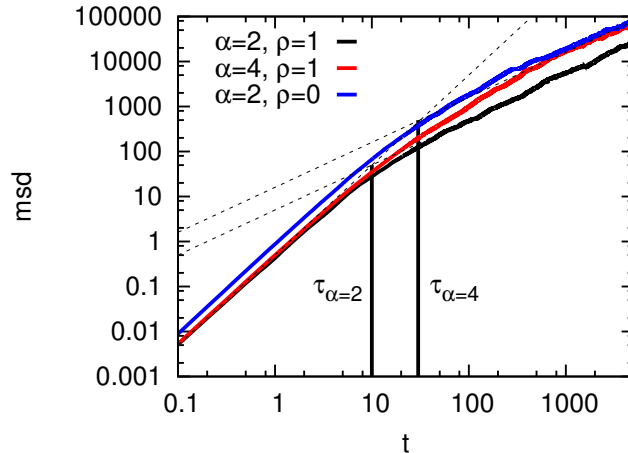


Figure 13: Mean square displacement of run-and-tumble particles at different aspect ratios  $\alpha$  and different particle densities  $\rho$  indicated in the labels, self-propelling velocity  $v = 1$ .

aspect ratio  $\alpha$ , the diffusion coefficient increases and the diffusive regime is reached later.

### 3.2 Rotational diffusion enhancement

The rotational diffusion of passive rods always decreases with increasing particle density since the collision with neighboring rods hinders the Brownian rotation with respect to that of isolated rods. Interestingly, for active particles we find that the rotational diffusion coefficient can also increase with particle density. This enhancement is therefore a specific effect due to the active character of the particle, which has, to our knowledge, not yet been reported. In the following we characterize the presence and significance of this enhancement as a function of the particle aspect ratio and self-propelling velocity.

In our model, at aspect ratio  $\alpha = 1$ , the rotational diffusion is an independent parameter, i.e. it does not depend on density or on velocity, since the mechanical interactions between spheres do not change particle orientation. The dependence of the rotational diffusion coefficient on the particle density at larger aspect ratios and different velocities is shown in Figure 14. At aspect ratio  $\alpha = 2$ , the rotational diffusion increases with density, and only at density values close to the close-packing there is a slight decrease of the rotational diffusion. This effect increases with higher self-propelling velocity. Increasing the aspect ratio to  $\alpha = 4$  (Figure 14b), the rotational diffusion has different behavior as a function of particle density. For velocity  $v = 2$  it increases until  $\rho = 0.5$ , while it slightly decreases for higher densities. For velocity  $v = 1$  the rotational diffusion decreases monotonically with density. An intermediate behavior where the rotational diffusion is almost independent on density is observed at velocity  $v = 1.5$ . For particles of aspect ratio  $\alpha = 6$

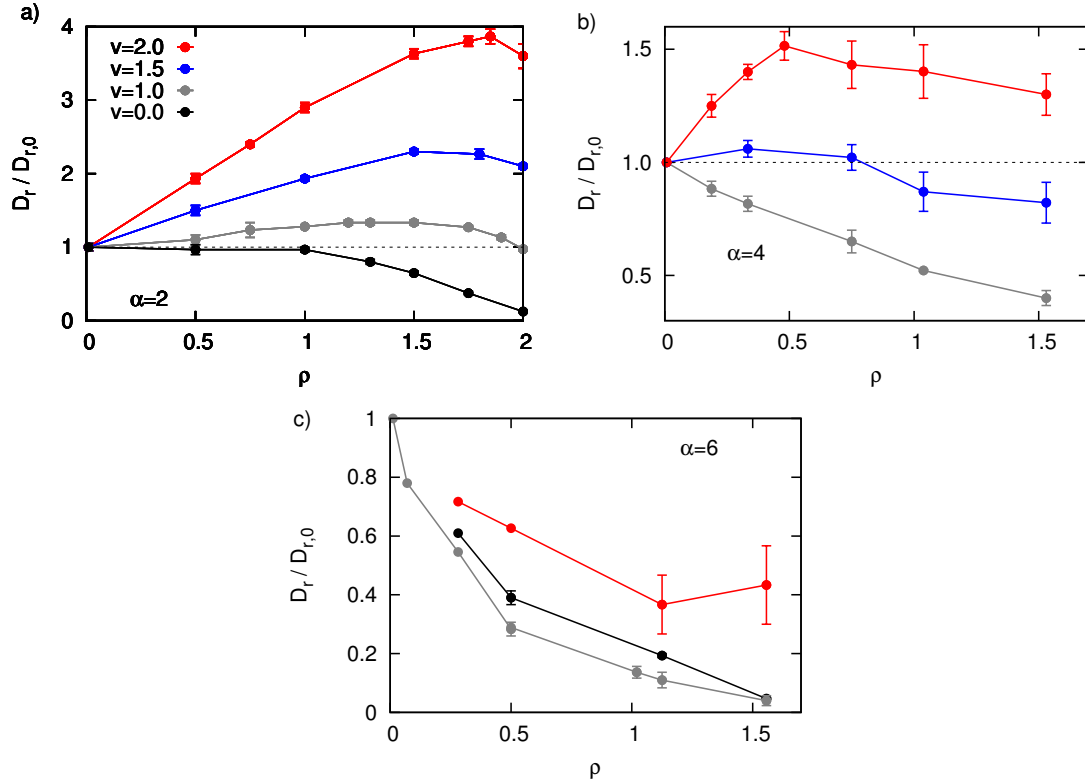


Figure 14: Rotational diffusion coefficient  $D_r$  as a function of particle number density  $\rho$  at different self-propelling velocities  $v$  (see legend) and different particle aspect ratios,  $\alpha = 2$  (a),  $\alpha = 4$  (b),  $\alpha = 6$  (c).

the rotational diffusion monotonically decreases with particle density up to self-propelling velocity  $v = 3$ , only at  $v = 4$  an increase of the rotational diffusion is observed (not shown in Figure 14c).

Figure 15a shows the same rotational diffusion data as a function of aspect ratio at different self-propelling velocities and different densities. The rotational diffusion increases with aspect ratio from  $\alpha = 1$  to  $\alpha = 2$ , and decreases for  $\alpha > 2$ . At  $\alpha = 2$  it has a maximum at every velocity and density considered. Figure 15b shows rotational diffusion data as a function of self-propelling velocity at different aspect ratios. For aspect ratios  $\alpha > 1$  the rotational diffusion increases with self-propelling velocity. Figure 16 shows the velocity and aspect ratio values for which the rotational diffusion increases with density (enhancement) and the values for which it decreases with density (no-enhancement).

Intuition may suggest that density suppresses motion and rotation. But actually, we have seen that there is a zone in the  $v$ - $\alpha$  parameter space, where the rotational diffusion coefficient increases with particle density, which indicates that collisions among the particles enhance their rotation. This result is only possible with active particles and not with

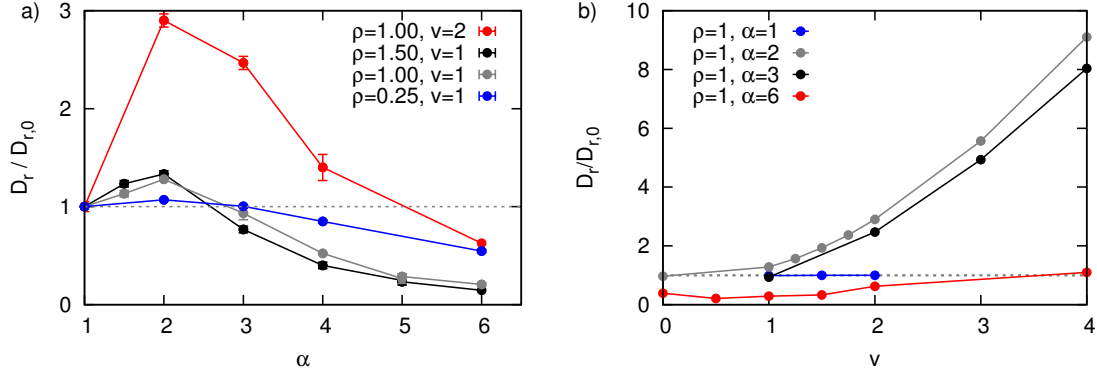


Figure 15: Rotational diffusion coefficient  $D_r$  as a function of particle aspect ratio  $\alpha$  at different particle densities  $\rho$  and self-propelling velocities  $v$  (a), and as a function of self-propelling velocity (b) .

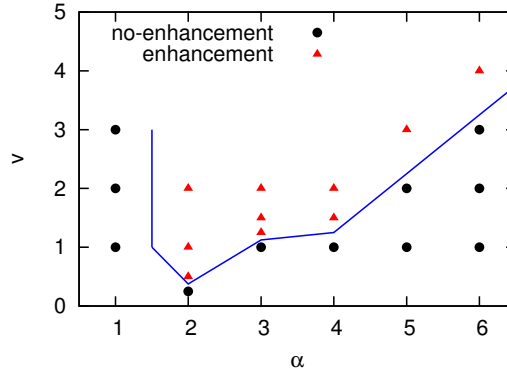


Figure 16: Rotational diffusion enhancement with particle density in the  $\alpha$ - $v$ -space (aspect ratio - self-propelling velocity - space). Enhancement means that there is at least one density  $\rho$  for which  $D_r > D_{r,0}$ .

passive Brownian ones. Therefore there has to be a critical self-propelling velocity at which this effect sets in. From Figure 16 we notice that this critical velocity increases with aspect ratio.

The increasing behavior of the rotational diffusion with density can be explained within an active-gas approximation, e.g. particles performing binary, point-like collisions which do not induce alignment. On top of the rotational diffusion of a single particle  $D_{r,0}$ , the contribution to the rotational diffusion of collisions is proportional to the rotation angle  $\Delta\theta$  during a collision and inversely proportional to the time  $\tau$  between two collisions

$$D_r \sim D_{r,0} + \frac{\Delta\theta^2}{\tau} \quad (46)$$

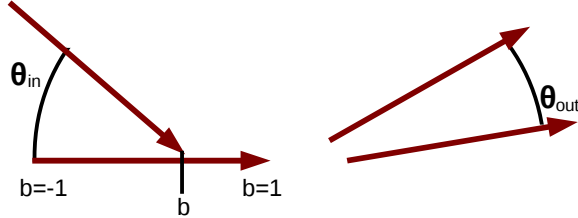


Figure 17: Sketch of the collision between two particles. Changing collision point  $b$  and angle  $\theta_{in}$ , we measure the angle between the two particles after the collision  $\theta_{out}$ .

with  $\tau = \lambda/v$ , where  $\lambda$  is the free path between collisions, which will decrease with density,

$$\lambda \sim \frac{1}{\sigma\rho} \quad (47)$$

and  $\sigma$  is the characteristic particle length. It follows that  $\tau \sim 1/v\sigma\rho$  and that

$$D_r \sim D_{r,0} + v\sigma\rho\Delta\theta^2. \quad (48)$$

This increasing behavior of the rotational diffusion with density is observed for example at aspect ratio  $\alpha = 2$  and self-propelling velocity  $v = 1$ . Increasing the aspect ratio the collisions between particles induce more alignment. Particles tend to stay aligned for some non negligible time after the collision, eventually forming clusters. The active-gas approximation does not hold any more, and the rotational diffusion decreases with density. An increase of self-propelling velocity increases rotational diffusion since the overall dynamics get faster, e. g. all particles speed up and time between collisions decreases. As a consequence also the rotations become faster and the rotational diffusion coefficient increases. The observed increase is though not linear as predicted from the active-gas approximation. This deviation from the linear behavior can be explained considering that the rotation angle  $\Delta\theta$  induced by the collision can also depend on  $v$ , such that the effective dependence of the rotational diffusion coefficient on the self-propelling velocity  $v$  becomes of the type  $D_r \sim v^\gamma$  with  $\gamma > 1$ .

### 3.2.1 Two-particles scattering analysis

To understand why at  $\alpha = 3$ ,  $D_r$  decreases with  $\rho$ , we analyze the collision of two non-tumbling (deterministically moving) particles with self-propelling velocity  $v = 1$ . We

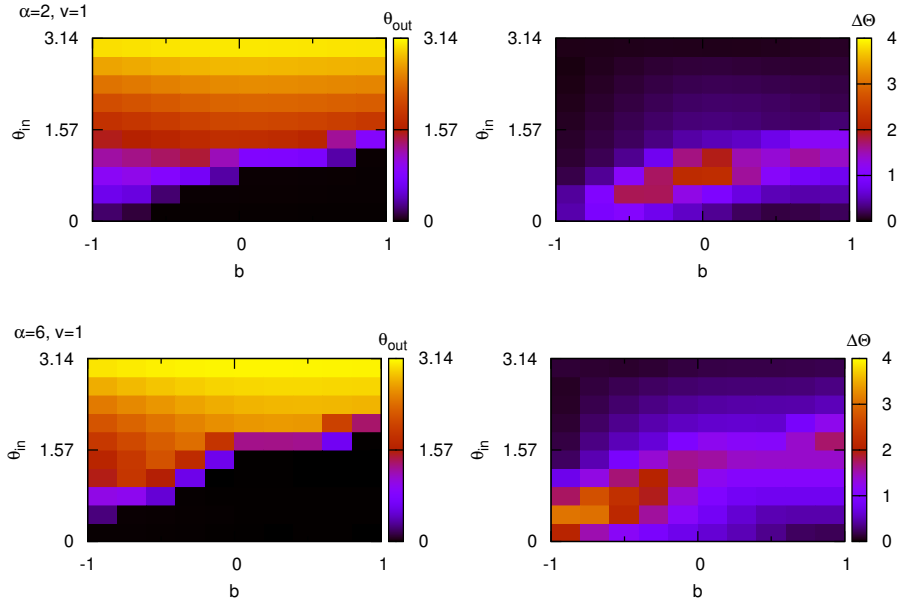


Figure 18: Angle  $\theta_{out}$  between the two colliding particles after the collision (left panels) and the total rotation angle  $\Delta\Theta$  (right panels) as a function of the collision angle  $\theta_{in}$  and collision position  $b$  for different aspect ratios  $\alpha$ .

vary the collision point  $b$  and collision angle  $\theta_{in}$  between the two particles, and measure the angle  $\theta_{out}$  between the two particles after the collision. As shown in the sketch of Figure 17,  $b = -1$  ( $b = 1$ ) indicates that the incoming particle hits the other one on the back (front).

There is a zone in the  $b$ - $\theta_{in}$  space, for which the two particles align ( $\theta_{out} = 0$ ). This zone increases with particle aspect ratio, as can be seen in Figure 18(left panels) and Figure 19a. In Figure 19a we show the quantity

$$I = \left\langle 1 - \frac{\theta_{out}}{\pi} \right\rangle_{b, \theta_{in}} \quad (49)$$

where the average is over all the possible collisions. This quantity is 1 if the particles are always aligned after all possible collisions, while  $I$  is 0 if the particles are always anti-aligned ( $\theta_{out} = \pi$ ).

We can conclude that at  $\alpha = 3$  and  $v = 1$ , although there is no cluster formation yet, the rotational diffusion decreases with density since after the collisions particles are often aligned such that they stay together for a non negligible time, leading eventually to many particles collisions or clustering. The active-gas approximation (binary collisions) is no longer valid and the rotational diffusion decreases with density.

In order to quantify the rotation induced by the collision we do also measure the total rotation angle  $\Delta\Theta = \Delta\theta_1 + \Delta\theta_2$ , where  $\Delta\theta_i$  is the difference of the orientation angle of the  $i$ -th particle before and after the collision. This quantity indicates how much the two particles have rotated during the collision. Increasing aspect ratio,  $\Delta\Theta$  increases from  $\alpha = 2$  to  $\alpha = 4$  and is almost constant for  $\alpha > 4$ , as shown in Figure 18(right panels) and Figure 19b, where we actually show the average

$$R = \left\langle \frac{\Delta\Theta}{\pi} \right\rangle_{b, \theta_{in}}. \quad (50)$$

This indicates that the decrease of the rotational diffusion with density is exclusively due to the collision-induced alignment and the breakdown of the active-gas approximation.

Increasing the self-propelling velocity we observe a slight decrease of the alignment as well as an increase of the total rotation angle  $\Delta\Theta$ . This, together with the fact that with increasing self-propelling velocity the entire dynamics becomes faster, e.g. the time between two collisions decreases and the collision itself is faster, explains why increasing the self-propelling velocity the dependence of the rotational diffusion on particle density can change from decreasing to increasing.

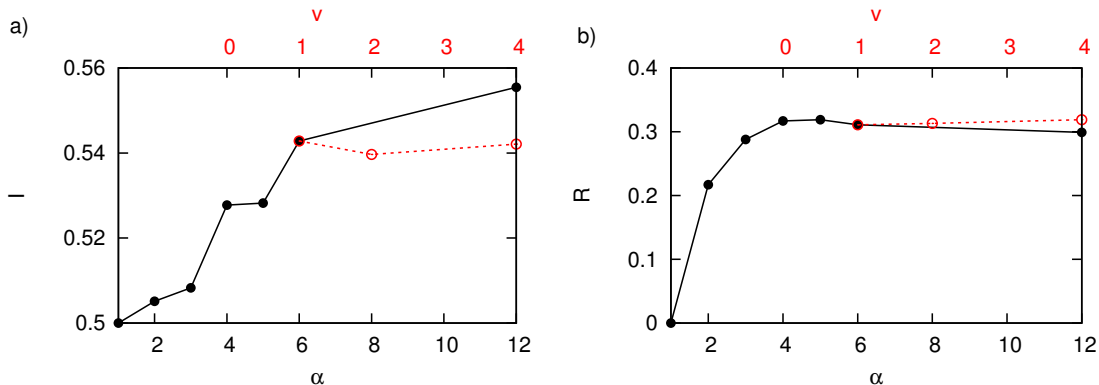


Figure 19: Integral  $I$  (a) and integral  $R$  (b) (see eq.(49) and eq.(50) for definitions) as a function of aspect ratio  $\alpha$  (at  $v = 1$ ) and as a function of self-propelling velocity  $v$  (at  $\alpha = 6$ ).

### 3.2.2 Cluster analysis

Cluster formation or coexistence of phases with two different densities can be characterized by the bi-modality of the probability density function of the cell density. It depends on self-propelling velocity  $v$ , particle aspect ratio  $\alpha$  and on particle density  $\rho$ . From the phase diagrams shown in References [38, 43], we notice that at constant self-propelling velocity, the tendency to form clusters increases with particle aspect ratio and particle density.



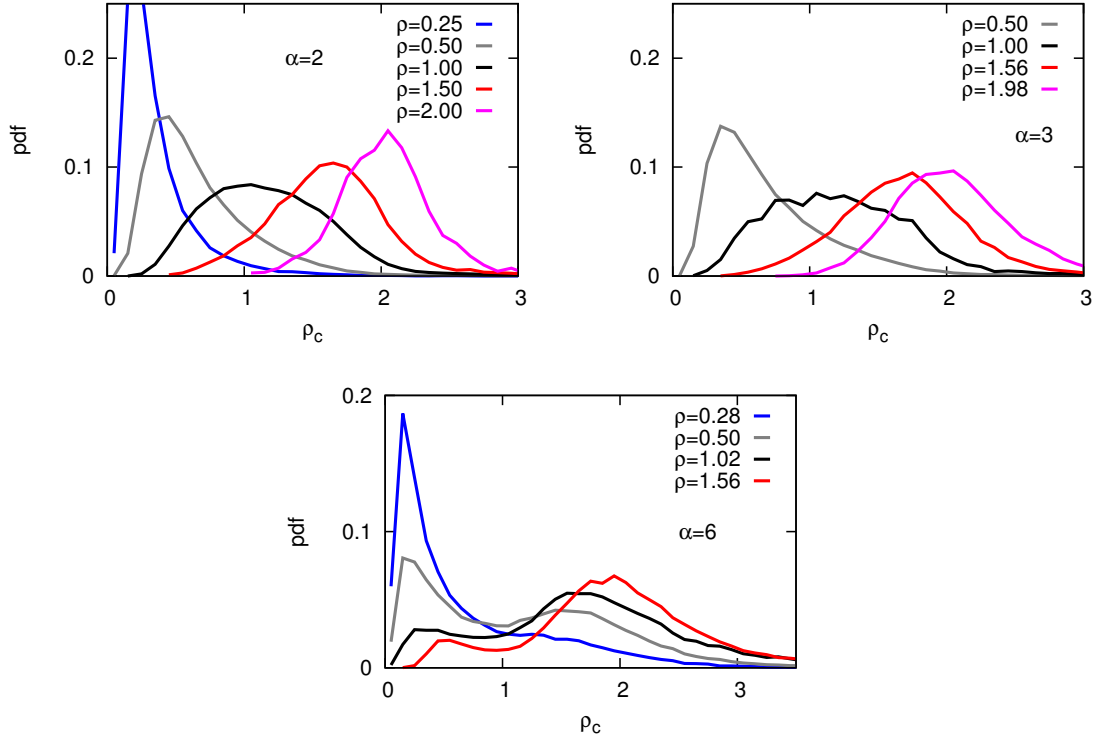


Figure 20: Probability distribution function of the cell density  $\rho_c$  at different particle densities  $\rho$  and different aspect ratios  $\alpha$ . Self-propelling velocity  $v = 1$ .

In order to better understand the dependence of the rotational diffusion on particle density and aspect ratio, we analyze the cluster formation through Voronoi cells [84]. The Voronoi tessellation is made around the particles centers-of-mass. The  $i$ -th Voronoi cell is defined such that all the points in the cell are closer (or equally distant) to  $\mathbf{r}_i$  than to all other  $\mathbf{r}_{j \neq i}$ .

Dividing the total area in Voronoi cells allows us to define a local or cell density  $\rho_c$  as

$$\rho_c = \alpha/2A \quad (51)$$

where  $\alpha$  is the particle aspect ratio and  $A$  is the cell area. In Figure 20 we show the probability density function (pdf) of the cell density. We notice that for particles with self-propelling velocity  $v = 1$ , cluster formation does not happen at  $\alpha = 2$  and  $\alpha = 3$ . At  $\alpha = 6$  cluster formation happens at  $\rho \geq 0.5$ . Since at  $v = 1$  there is rotational diffusion enhancement (increasing behavior with density) only at aspect ratio  $\alpha = 2$ , we can conclude that the absence of cluster formation does not imply rotational diffusion enhancement.

### 3.2.3 Order parameter

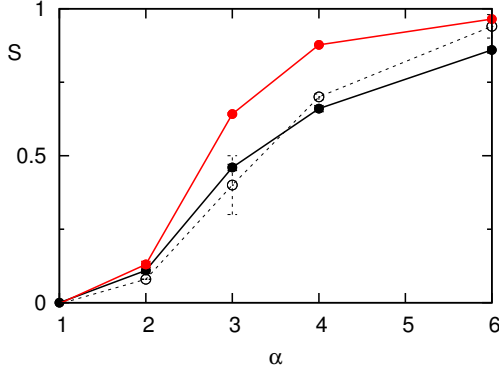


Figure 21: Order parameters  $S_n$  (red) and  $S_p$  (black) as a function of particle aspect ratio  $\alpha$ . Particle density  $\rho = 1$  (dashed line),  $\rho = 0.25$  (solid line). Self-propelling velocity  $v = 1$ .

We characterize the collision-induced order as a function of aspect ratios  $\alpha$  also with the order parameters

$$S_n = \sum_{i,j \in \delta} \cos[2(\theta_i - \theta_j)] \quad \text{and} \quad S_p = \sum_{i,j \in \delta} \cos[(\theta_i - \theta_j)] \quad (52)$$

where  $\theta_i - \theta_j = \arccos(\mathbf{e}_i \cdot \mathbf{e}_j) \in [0, \pi]$  is the angle between the orientation vectors  $\mathbf{e}_i$  and  $\mathbf{e}_j$  of the  $i$ -th and  $j$ -th particle. The pairs  $i, j$  are chosen such that the distance between the two particles is less than  $\delta$ , we choose  $\delta = 1$ .  $S_n$  is the nematic order parameter [47, 85],  $S_n = 1$  in the nematic phase and  $S_n = 0$  in the isotropic phase.  $S_p$  is the polar order parameter, which does distinguish between parallel ( $S_p = 1$ ) and antiparallel ( $S_p = -1$ ) orientation of rods,  $S_p = 0$  in the isotropic state. By construction,  $S_n$  is always larger than  $S_p$ . Both order parameters are shown in Figure 21. There we notice that both order parameters increase with aspect ratio. For spheres, the order parameters are zero in our model, since the orientation of spheres is not affected by collisions with other particles. The highest increase of the order parameter is between  $\alpha = 2$  and  $\alpha = 3$ , reflecting the transition from the regime in which the rotational diffusion increases with aspect ratio ( $\alpha \leq 2$ ) to the regime in which the rotational diffusion decreases with aspect ratio ( $\alpha > 2$ ).

### 3.3 Translational diffusion

Here we study the translational diffusion coefficient and its relation with the rotational diffusion, investigating the range of validity of eq.(45). In Figure 22, we report values of the translational diffusion of rods as a function of particle density for different particle aspect ratios and different particle self-propelling velocities. At every aspect ratio and

every particle velocity  $v > 0$  considered, the translational diffusion decreases with particle density, in agreement with the experimental results of Reis and Kudrolli [78, 79]. There, the diffusivity decreases with density and at too high density the dynamics does not reach the diffusive regime, since the particles almost do not move any more, showing crystallization and caging phenomena. At larger aspect ratios  $\alpha > 4$ , based on the data shown in Figure 23a, we infer that the translational diffusion coefficient can also increase with density. Due to the large separation between between  $\tau$  and  $\tau_r$  at  $\alpha > 4$  we have been able to determine only the rotational diffusion coefficient.

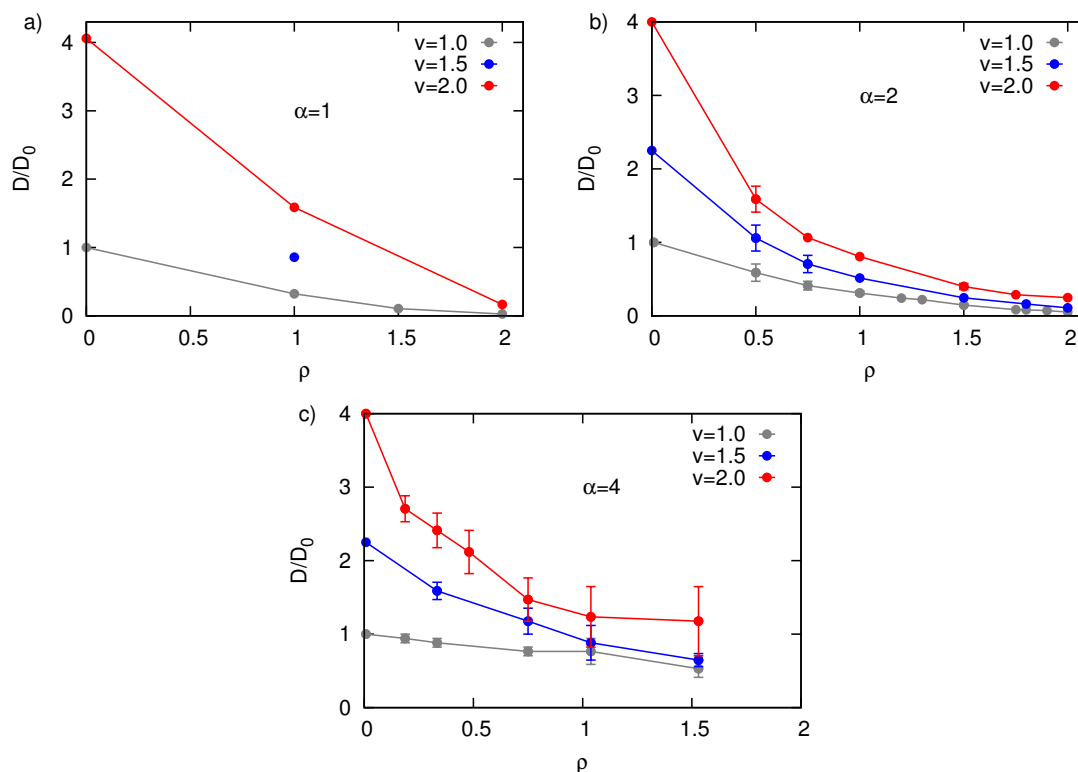


Figure 22: Translational diffusion coefficient  $D$  as a function of particle number density  $\rho$  at different self-propelling velocities  $v$  (see legend) and different particle aspect ratios,  $\alpha = 1$  (a),  $\alpha = 2$  (b),  $\alpha = 4$  (c).

For dense systems, the translational diffusion increases monotonically with the aspect ratio, besides a decrease from  $\alpha = 1$  to  $\alpha = 2$  at self-propelling velocity  $v = 2$ , as shown in Figure 23a. At low aspect ratios, velocity  $v = 1$  and both at  $\rho = 1$  and  $\rho = 1.5$ , the diffusivity is much smaller than the diffusivity  $D_0$  of a single particle. Increasing the particle aspect ratio the diffusion coefficient increases and the crossover from ballistic to diffusive regime is slower (see also Figure 13), since a cluster rotates less than a single particle and needs more time to change direction of motion. From the data that we have

we can infer that at high enough aspect ratio the translational diffusion coefficient can reach values larger than  $D_0$ .

In Figure 23b we show the translational diffusion as a function of self-propelling velocity. We have seen that the rotational diffusion of spheres is, by construction of our model, independent on velocity and any other parameters. The translational diffusion of a single particle will then increase quadratically with velocity, according to eq.(45). At non-vanishing concentrations, collisions between spheres clearly hinder and decrease the translational diffusion, while the rotational diffusion is unaffected by density. The translational diffusion of interacting spheres at  $\rho > 0$  still increases quadratically with velocity, but with lower prefactors.

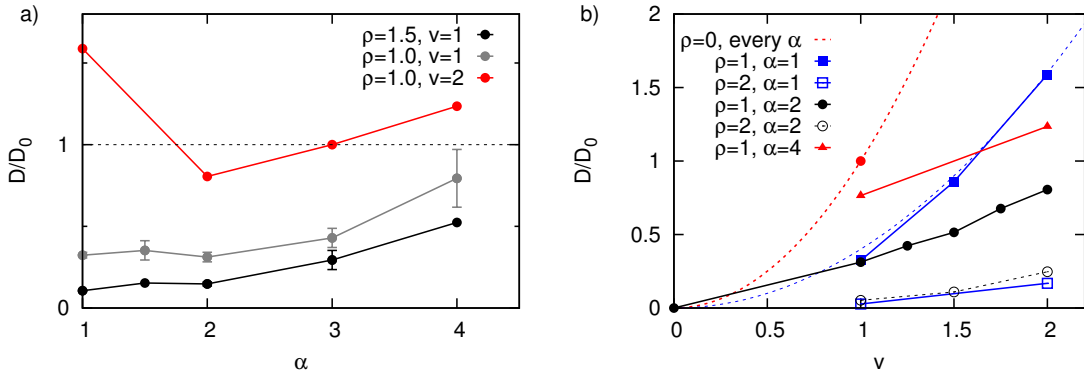


Figure 23: Translational diffusion coefficient  $D$  as a function of particle aspect ratio  $\alpha$  at different particle densities  $\rho$  and self-propelling velocities  $v$  (a), and as a function of self-propelling velocity (b) .

### 3.3.1 Effective particle velocity

In order to better study the relation between rotational and translational diffusion coefficient at finite densities, and to check the validity of eq.(45) for dense systems, we measure the average effective particle square velocity  $v_e^2$  as a function of particle density, where the average is a time and ensemble average. The effective average square velocity can be simply measured as the average particle displacement in a time unit. For single-particle simulations it equals the self-propelling velocity, while it is the sum of self-propelling velocity and mechanical collisions with other particles in dense systems.

This effective velocity decreases linearly with particle density, since the free particle movement is hindered by collisions, as shown in Figure 24. There we also show the product  $D_r D / D_{r,0} D_0$  as a function of particle density. The same quantity normalized by the average square effective velocity  $v_e^2$  is shown in Figure 24c. The product of rotational and translational diffusion coefficients decreases with density, almost as the effective velocity

does, and we conclude that eq.(45) is well satisfied at low particle densities, low aspect ratio and high self-propelling velocities.

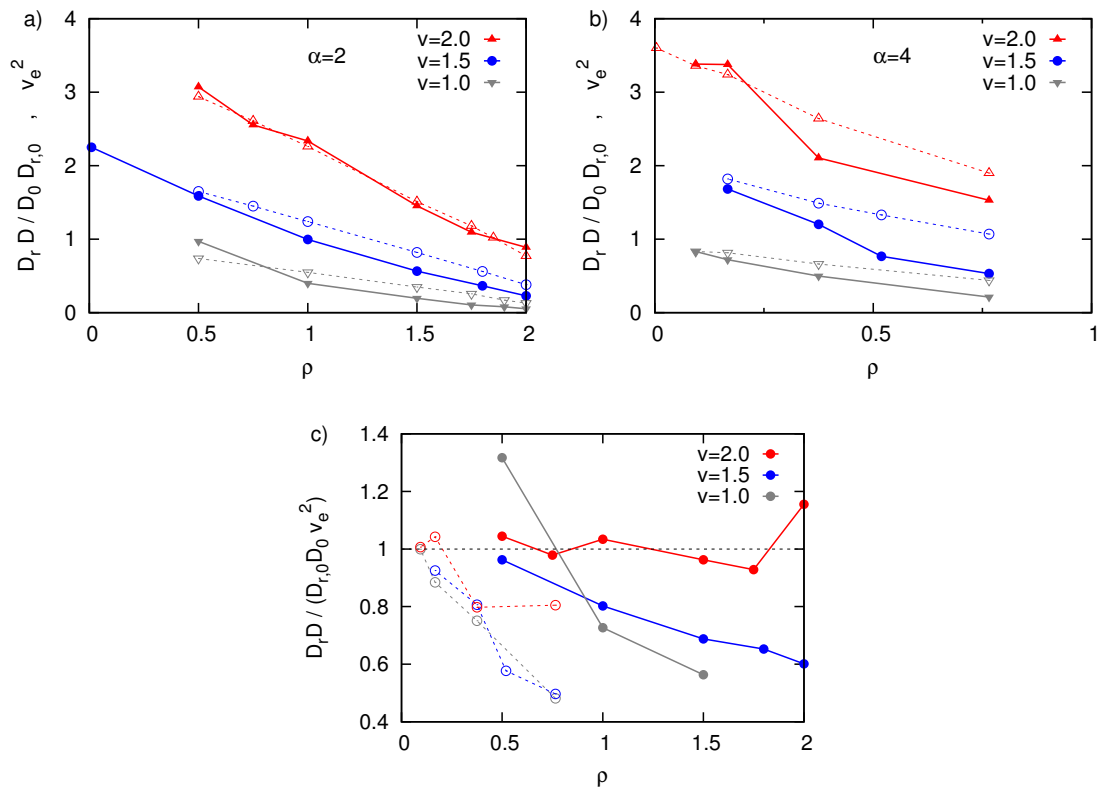


Figure 24: Product  $D_r D$  (solid lines, full symbols) and average square velocity  $v_e^2$  (dashed lines, empty symbols) as a function of particle number density  $\rho$ , at aspect ratio  $\alpha = 2$  (a) and  $\alpha = 4$  (b) for different self-propelling velocities (see legend). Product  $D_r D / D_{r,0} D_0$  normalized by the average square effective velocity  $v_e^2$  (c),  $\alpha = 2$  (solid lines),  $\alpha = 4$  (dashed lines).

### 3.4 Comparison between different noise types

In order to understand the general applicability of the results shown in the previous sections, we perform a few simulations with active Brownian particles and deterministically moving particles. These simulations help to better understand the run-and-tumble model extensively discussed in this thesis.

Deterministically moving particles are particles that change their direction of motion only because of collisions with other particles. Active Brownian particles are simulated imposing at every time step a random torque on the particle. In contrast to the run-and-tumbling motion, where during the tumbling event the self-propulsion of the particle is deactivated, for active Brownian particles the self-propulsion is always present. The

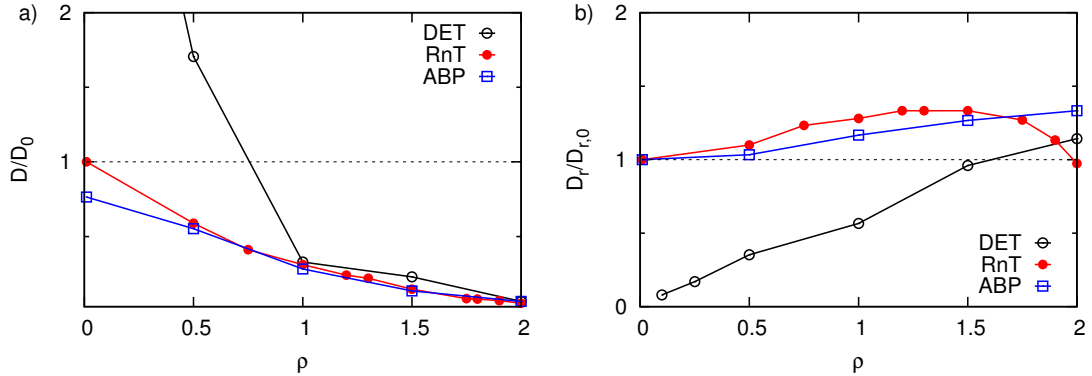


Figure 25: Comparison between run-and-tumbling particles (RnT), active Brownian particles (ABP) and deterministically moving particles (DET). Translational (a) and rotational (b) diffusion values as a function of particle density  $\rho$ . Particle aspect ratio  $\alpha = 2$  and self-propelling velocity  $v = 1$ .

intensity of the random torque is tuned such that the rotational diffusion of a single particle is the same as the rotational diffusion of a single run-and-tumbling particle  $D_{r,0}$ . It turns out that with our tumbling-parameters choice (tumbling duration time, tumbling frequency and tumbling angle) the translational diffusion of a single active Brownian particle is slightly lower than the translational diffusion of a single run-and-tumbling particle (see Figure 25a).

In Figure 25a, we show the translational diffusion as a function of particle density for the three different particle types. The translational diffusion of deterministically moving particles diverges at low densities, since a single deterministically moving particle would always move straight and never change direction, such that its motion is ballistic and no more diffusive. Increasing the particle density the translational diffusion of deterministically moving particles decreases. The translational diffusion of active Brownian particles decreases also with density, and the values are comparable to the run-and-tumbling ones. At densities  $\rho \geq 1$ , the translational diffusion values of deterministically moving particles are still slightly higher than the other values reflecting the lower rotational diffusion values, but at  $\rho \sim 2$  the values of all the three different particles types almost coincide.

As shown in Figure 25b, the rotational diffusion of deterministically moving particles increases linearly with density, being zero in the dilute limit of a single particle and being comparable with the values of run-and-tumbling particles in the high packing limit. The rotational diffusion of active Brownian particles increases with density similarly as the rotational diffusion of run-and-tumbling particles, although at high densities we do not observe the decrease that we notice for run-and-tumbling particles. At high density, small and fast rotations as those of active Brownian particles are more effective to change

orientation, since large rotations of tumbling events are easily suppressed by neighboring particles. At  $\rho = 2$ , active Brownian particles show the highest rotational diffusion, while run-and-tumbling particles shown the lowest one.

From this comparison of translational and rotational diffusion as a function of particle density for different particle types we can conclude that the presented enhancement of the rotational diffusion with particle density is independent on model details. The decrease of the rotational diffusion of run-and-tumbling particles in the high-density limit is not present for the other particle types. The fast rotations of active Brownian particles result to be more effective to change orientation than tumbling events, where large rotations are easily stopped by neighboring particles. Moreover, the deactivation of the self-propulsion during the tumbling event may also favor the slight lower value of the rotational diffusion of run-and-tumbling at high densities.

### 3.5 Summary

In this chapter we have investigated how rotational and translational diffusion coefficients of active particles depend on system parameters like particle aspect ratio, particle density and particle self-propelling velocity. Intuition may suggest that increasing particle density diminishes the possibility to rotate and therefore a decreasing behavior of the rotational diffusion coefficient as a function of density can be expected. This is indeed the case for passive Brownian particles, while for active particles we show that the rotational diffusion can increase with density. We find a zone in the  $\alpha$ - $v$ -space in which the rotational diffusion of active rods is higher than the rotational diffusion of free moving particles. In other words, collisions among particles enhance their rotation.

We have described this phenomenon with a simple active-gas picture. Increasing the particle aspect ratio, collisions among particles lead to more particle alignment. Particles move together for a non-negligible time eventually forming clusters. The active-gas picture is no longer valid and the rotational diffusion coefficient decreases with density. Increasing the self-propelling velocity the overall dynamics becomes faster and therefore also the rotation and the rotational diffusion coefficient. These results turns out to be independent on the model details. They are valid both for run-and-tumbling particles and for Active-Brownian-Particles.

We also described the behavior of the translational diffusion coefficient, which is a consequence of the behavior of the rotational diffusion, in good agreement with the relation  $D \sim v^2/D_r$ . This agreement is better at low aspect ratio, where the active-gas approximation is valid. Increasing the particle aspect ratio, the translational diffusion coefficient increases, since longer particles form cluster more easily, and big clusters change direction of motion much slower than single particles. For  $\alpha \leq 4$ , the translational diffusion coeffi-

cient decreases with particle density. Based on our results we infer that for higher aspect ratios the translational diffusion coefficient may also increase with density. Further studies with longer particle tracking data are needed to corroborate this result at higher aspect ratios. Increasing the particle self-propelling velocity the translational diffusion coefficient of elongated particles increases, but not quadratically as for single-particle simulations.

The collective dynamics of passive rods as a function of their number density and their length has been widely studied. Increasing density particles undergo the isotropic-nematic transition, and the rotational diffusion decreases with density. On the other hand, for active particles the dynamical properties and in particular the dependence of translational and rotational diffusion coefficients on particle aspect ratio, particle density and particle velocity have been less studied. Our results are therefore of great theoretical and practical interest, giving new insight in the dynamical properties of off-equilibrium systems. Moreover, our results are of great relevance for the development of techniques for microfluidic devices, since in order to optimally manipulate the motion of particles a complete knowledge of how diffusion coefficients depend on system parameters is extremely useful.



---

## 4 Motility-sorting of particles in micro-channels

Here we present results about the motion of self-propelled particles in micro-channel confinement, both with and without Poiseuille flow. We first discuss single component systems and then we focus our attention on two component systems.

### 4.1 Introduction

Sorting different types of particles, which are initially in a mixed state, always fascinated scientists. In Maxwell's famous Gedanken-experiment [86], fast and slow gas molecules in a box were separated by the so called Maxwell demon, paradoxically violating the second law of thermodynamics [87]. The phase behavior of small and long passive rods has been investigated by Vroege and Lekkerkerker [88]. More recently, several studies focused the problem of sorting different types of particles, exploiting entropic means [89], gravity [90], and microfluidic devices [91–93].

The separation of big and small passive particles under gravity is known as *Brazilian Nut Problem* [90], or also as *Müsli Problem*. Indeed one can easily observe, that shaking a muesli box which has in its inside different kinds of nuts and flakes, some types of particles tend to reach the bottom and others the top of the box. In Figure 26, simulation snapshots of a two-component system, a binary mixture, under gravity is shown. In the reported cases, depending on the simulation parameters like temperature, masses and diameters of the two types of particles, small particles are found prevalently on top of the big particles, which are then at the bottom of the box, or vice-versa.

Separation of small and big particles has been investigated also in channels with solvent flow, simulating the separation of red blood cells and platelets in blood vessels [94]. Red blood cells are bigger than the platelets and are found preferentially at the center of the vessel, while the small platelets aggregate near the walls, giving rise to a clear separation of the two types of particles.

Separation of passive Brownian particles is an interesting research field, separation and

sorting of self-propelled particles is also a very fascinating topic. Moreover, populations of active particles are in nature usually heterogeneous in all their characteristics, like size, shape, composition or in self-propelling velocity. For example, sperm cells of mammals are not all equally fast and only the fastest ones can reach the ovum and fertilize it.

In assisted reproductive technologies [95] like intracytoplasmic sperm injection only one sperm cell has to be chosen from a cell culture or colony for the fertilization of the ovum. The common method used to select the fastest cells, is called the swim-up method. It consists in taking the cells in solution and putting a bigger layer of solvent without cells over the cell-solution layer. After sufficient time, only a thin layer on the top will be taken, which only the motile cells will have reached, while non-motile cells will still be on the bottom [96]. Other methods use laser traps to select cells [97, 98], and also microfluidic devices [99] have been used to sort motile from non motile sperm cells [100].

A spontaneous segregation of active and passive particles, freely swimming in a periodic two-dimensional box, has been numerically investigated [101]. Clockwise rotating and anti-clockwise rotating self-propelled particles have been separated using asymmetric obstacles [102]. The study of separation of self-propelled particles with different motilities has been started by means of numerical simulations [103] as well experimentally using centrifuges [104]. Moreover active particles have been also used to sort passive particles with different properties in microchannel environment [105].

In this chapter we numerically show that two types of particles, which differ only in their swimming speed, spontaneously separate from each other in the simple geometry of a micro-channel, with and without solvent Poiseuille flow, and can therefore be easily separated from each other in microfluidic devices.

The actual challenge is indeed the contribution to the possible development of microfluidic lab-on-chip devices, capable to sort particles autonomously and on a small scale. One could actually separate fast and slow particles just considering that the two types of particles move and diffuse at different speeds. After putting a drop of particle mixture on a plane and waiting sufficient time, far away from the drop one would find fast particles only, while in the neighborhood of the starting drop one would find prevalently slow particles. But this is a quite trivial and inefficient way to separate the particles. It is reasonable to think that it requires much space and time to work properly. We imagine microfluidic devices that sort fast from slow particles efficiently, in short time and in a restricted and delimited space.

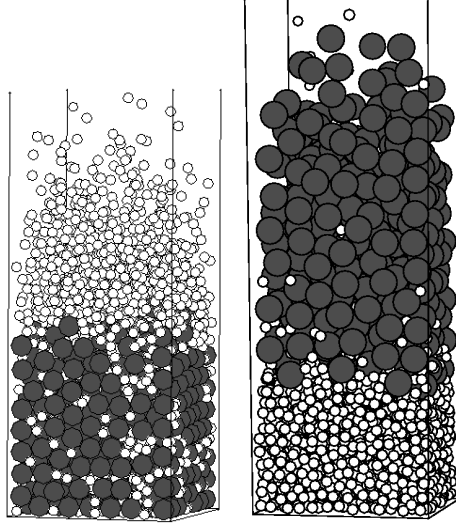


Figure 26: Separation of big and small (non-self-propelling) particles under gravity, the *Brazilian Nut Problem*. Depending on the simulation parameters like temperature, masses and diameters of the two types of particles, one can obtain that the small particles accumulate on top or below the big ones. Simulation snapshots taken from [90].

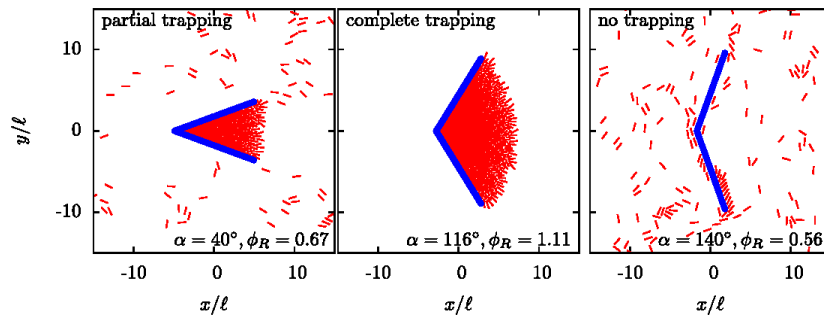


Figure 27: Trapping of self-propelling particles. Figure taken from [106].

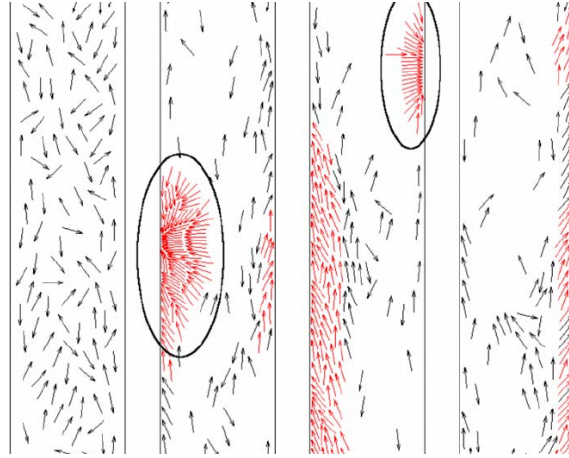


Figure 28: Aggregation of self-propelled particles near solid boundaries. Figure taken from [107].

## 4.2 Channel without flow

Brownian particles follow the Boltzmann distribution when exposed to an energy potential. On the other hand, active or self-propelled particles in energy potentials do not follow the Boltzmann distribution. The density profile of self-propelled particles shows instead peaks close to potential walls (potential barriers). This is known as solid boundary aggregation, a property of active matter [57, 61, 62, 106–109]. A particle that reaches the wall will stay there for a time which is of the order of magnitude of the time that the particle needs to change orientation because of noise, tumbling events or collisions with other particles. This does not happen for Brownian particles, which have no self-propelling force that stick them to the wall. They are free to diffuse away from the wall, their velocity direction is random and changes continuously.

In Figures 27 and 28 there are two examples of aggregation of self-propelling particles near solid boundaries. The first, taken from reference [107], is a micro-channel geometry, where the motion of rod-like particles is simulated. From the isotropic starting configuration on the left, aggregation at the walls and cluster formation and deformation is shown. An interesting geometry, made of two straight walls connected at their ends with a fixed angle, exploits the wall aggregation effect to trap active particles [106]. Interestingly, if the wall system is moved, a non trivial behavior of the trapping quality on the moving velocity of the walls is observed [109].

### 4.2.1 One component systems

We study the motion of self-propelled run-and-tumble particles of length to width aspect ratio  $\alpha = 2$  in channels with walls in the x-direction (at  $x = \pm L_x/2$ ) and periodic boundary

conditions in the  $y$ -direction. The channel has length  $L_y = 20l$  and width  $L_x = 10l$ , the number of particles can vary from  $N = 1$  to  $N = 360$ , such that the particle number density varies from  $\rho = Nl/L_xL_y \sim 0$  to  $\rho = Nl/L_xL_y = 1.8$ . As a reference, the density of hexagonally packed impenetrable beads of diameter  $a$  is  $\rho_m \simeq 2.31$ . The simulations start with random configurations and are  $10^6$  steps long. We exclude the first  $10^5$  steps from the time averages. In order to further increase the statistical averages, we compute ensemble averages over 8 different runs.

In Figure 29a we show the normalized local number density of the particles centers of mass  $\rho(x)$ , defined as

$$\rho(x) = n(x)l/L_y\Delta x \quad (53)$$

where  $n(x)$  is the number of particles in the bin centered at  $x$  of width  $\Delta x$ . The aggregation at the walls is particularly evident. A clear main peak is at distance  $x \sim 0.5$  from the walls, which corresponds to horizontal orientation of the particles (perpendicular to the walls), and several other smaller peaks are present. Increasing the self-propelling velocity these peaks increase in height, showing that the aggregation phenomenon increases with self-propelling velocity. Moreover, increasing the self-propelling velocity, the peak position slightly gets closer to the wall. Figure 29b shows another interesting quantity, the fraction  $\xi$  of particles at distance  $x < d$  from the channel walls (with  $d = 1$ , the particle length)

$$\xi = n/N \quad (54)$$

where  $n$  is the number of particles at distance  $x$  and  $N$  is the total number of particles. The particle fraction increases with self-propelling velocity and decreases with density. Computing  $\theta$ , the angle that particles form with the wall normal vector, we checked that the particle orientation at the walls does not depend on motility, as shown in Figure 29c. The slight offset of the density peaks is therefore only due to the softness of the interaction potentials. In Figure 29c we see that the angle close to the wall is 90 degrees, namely the particles which are closest to the wall are parallel to the wall. The distance between the wall and the center of mass of these particles is approximately half the width of the particle  $a/2 = 0.25$ . Then, further away from the wall, the angle decreases, reaching a value of approximately 20 degrees at the main density peak. The majority of the particles is indeed aligned almost perpendicular to the wall, as can be also seen from the density profiles and also from the snapshots in Figure 30.

#### 4.2.2 Two component systems

Here we study two-component systems, namely systems with two kind of particles which differ only in their self-propelling velocity. Half of the particles have self-propelling velocity

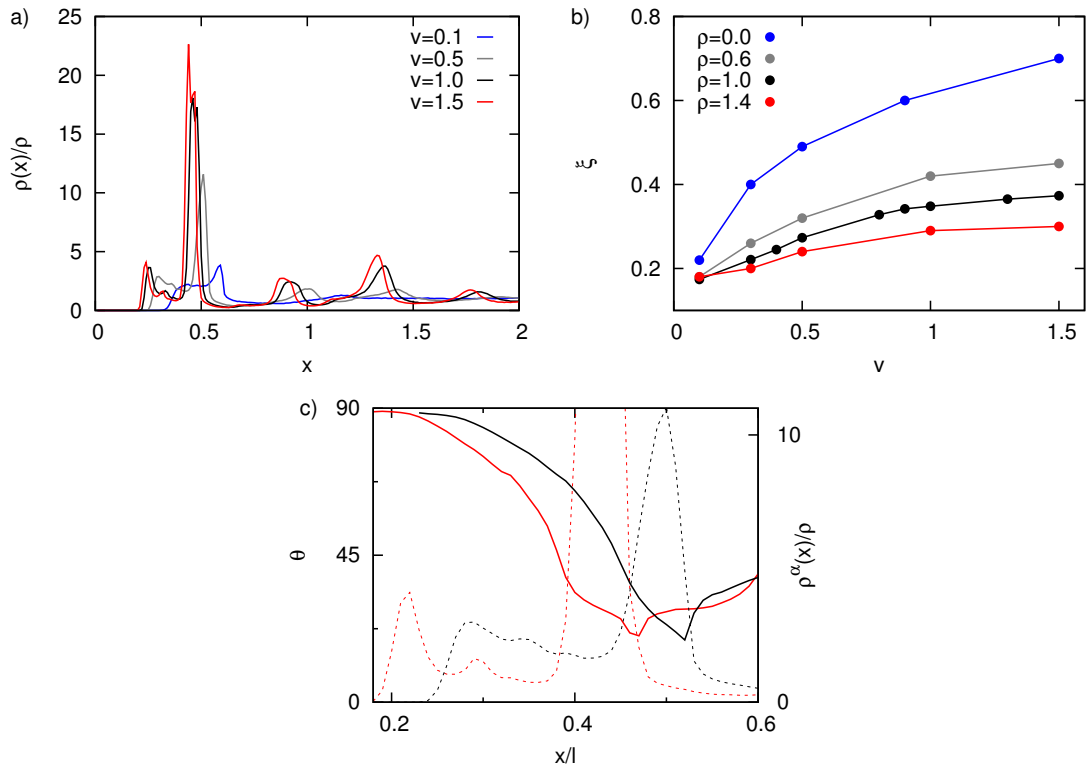


Figure 29: One component systems of run-and-tumbling particles: a) Normalized local number density profiles for different self-propelling velocities. b) Fraction of particles at distance from the wall  $x < d = 1$ . c) Angle between particle main axis and wall normal vector (solid lines). Density profiles are shown in dashed lines,  $v = 0.5$  (black) and  $v = 2$  (red).

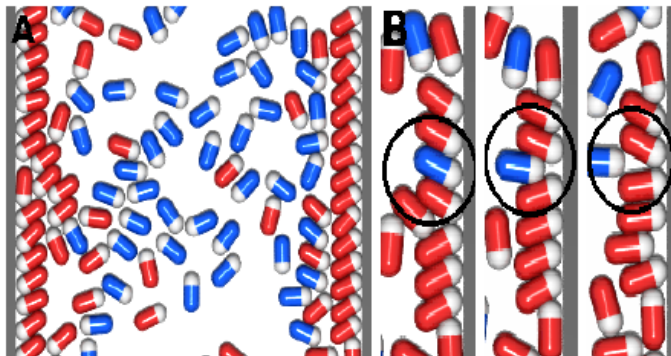


Figure 30: Simulation snapshots of a two-component system with  $v_s = 0.6$  and  $v_f = 1.4$ . a) Slow particles (blue) are segregated into the bulk, while fast particles (red) accumulate at the walls. b) Slow particle being pushed out of the wall as an illustration of the *expulsion mechanism*.

$v_s$ , which are slower than the other half of the particles that have self-propelling velocity  $v_f$ , being the faster particles. We consider Run-and-Tumbling particles. We are interested in characterizing the density of particles along the channel width for which we define the local number density of the particles centers of mass of each species  $\rho^\beta(x)$  in a bin of width  $\Delta x$ , centered at position  $x$ , as

$$\rho^\beta(x) = \frac{n^\beta(x)l}{L_y\Delta x}. \quad (55)$$

Here  $\beta$  denotes the considered species,  $n^\beta$  the number of particles with the center of mass in the considered bin. In Similar to systems with one component, Figure 31 (dashed lines), Figure 31 (solid lines) shows the density profiles of each of the components of a mixture of particles with the same velocities, namely  $v_s = 0.5$  and  $v_f = 2$ . A clear separation between the two types of particles is observed, since the density peak of slow particles in the one-component system is clearly suppressed in the mixed state. Slower particles are therefore more abundant in the bulk than the fast ones, as can be seen also in the snapshot in Figure 30A. This happens via an *expulsion mechanism* shown in Figure 30B. When a slow particle is at the wall, and there is a situation in which fast particles push symmetrically from both sides, the slow particle is expelled from the wall layer into the bulk. Therefore, fast particles are more abundant close to the walls, and slower particles are more abundant in the bulk.

In order to characterize the segregation of both components, we define the separation parameter as

$$\psi^f = \frac{\int_0^d \rho^f(x) dx}{\sum_\beta \int_0^d \rho^\beta(x) dx}. \quad (56)$$

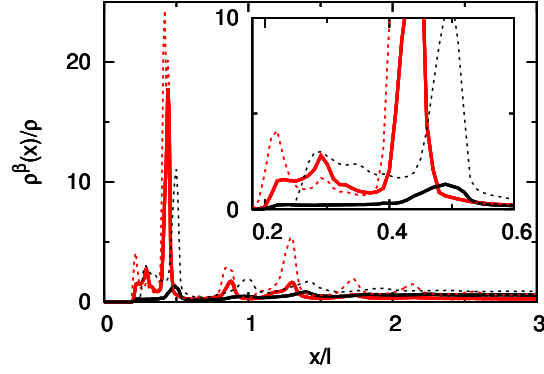


Figure 31: Normalized local number density of the particles centers of mass  $\rho^\beta(x)$  in a microchannel as function of the distance to the wall. Dashed lines correspond to two independent systems with one-component each, and solid lines to one system with two-components. For comparison, red lines denote particles with  $v = 2$ , and black with  $v = 0.5$ . The inset is a zoom on the same data.

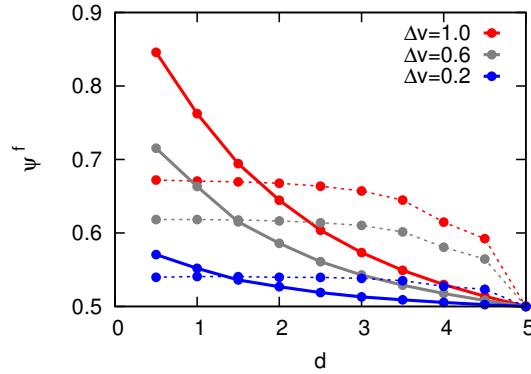


Figure 32: Separation of fast and slow particles quantified by  $\psi^f$  in eq.(56) at different distances  $d$  from the walls (solid lines) and from the channel center (dashed lines). Channel width  $L_x = 10$ .



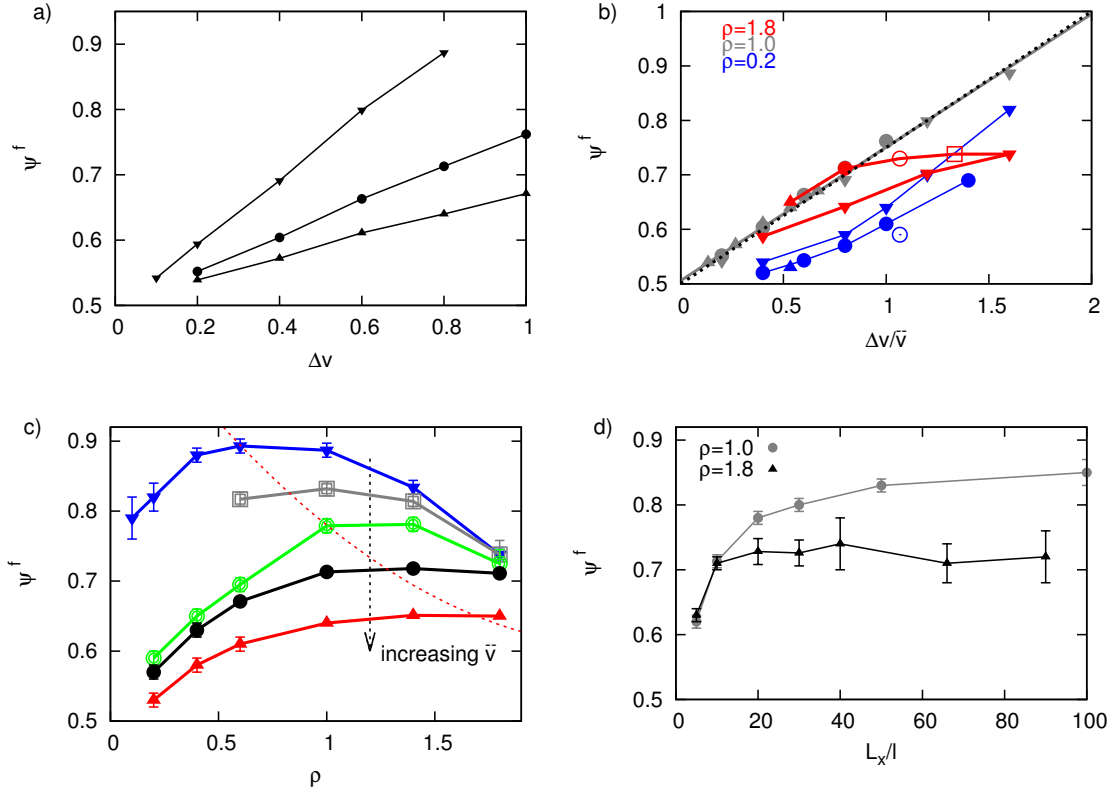


Figure 33: Separation of fast and slow particles close to the wall, quantified by  $\psi^f$  in eq. (56). Dependence on (a) velocity difference, (b) normalized velocity difference, (c) density, and (d) system size. In (a), (b), and (c), symbols consistently denote values of  $\bar{v}$ :  $\bar{v} = 0.5$  ( $\blacktriangledown$ ),  $\bar{v} = 0.6$  ( $\square$ ),  $\bar{v} = 0.75$  ( $\circ$ ),  $\bar{v} = 1.0$  ( $\bullet$ ),  $\bar{v} = 1.5$  ( $\blacktriangle$ ). The dashed line in (b) is the linear interpolation  $\psi^f = 0.25\Delta v/\bar{v} + 0.5$  and other lines are guides to the eye. Besides standard parameters, in (c) and (d)  $\Delta v = 0.8$ .

This quantity measures the percentage of fast particles in the particle population found close to the wall. By construction,  $\psi^f = 1$  or  $\psi^f = 0$  for complete separation, while for completely mixed two-component system  $\psi^f = 0.5$ . We employ  $d = l$ , the particle length, to analyze separation. Other distances, larger, but considerably smaller than  $L_x/2$  would provide qualitatively similar results, see Figure 32. In Figure 32 we notice that  $\psi^f$  decreases with  $d$  and increases with  $\Delta v$ . At  $d = L_x/2 = 5$ ,  $\psi^f = 0.5$  by construction, since for symmetry, in one channel half there will be the same amount of fast and slow particles.

In Figure 33, we analyze the dependence of the separation as a function of the difference of velocities  $\Delta v = v_f - v_s$ , average velocity  $\bar{v}$ , density  $\rho$ , and channel width  $L_x$ . Increasing  $\Delta v$  naturally leads to a larger separation, as shown in Figure 33a. This dependence can be understood better by normalizing  $\Delta v$  by  $\bar{v}$ , as shown in Figure 33b. Complete separation,  $\psi^f = 1.0$ , is expected for a mixture with one passive component, where  $\Delta v = 2\bar{v}$ , while for a system with equal velocities  $\psi^f = 0.5$ . A linear interpolation between both limits is then a reasonable first guess, and it shows indeed to be a very good approximation for the behaviour of systems with intermediate densities. For small densities, the accumulation at the walls is also small. The encounters of a larger number of particles at the walls is not frequent enough for the expulsion mechanism to be effective, therefore the separation is less efficient. For high densities, the accumulation at the wall is much higher. Situations with more than one layer of particles at the wall are frequent, resulting in a hampering of the expulsion mechanism. Interestingly, curves for different average velocity seem to approach nearly the same value of the separation parameter,  $\psi^f \simeq 0.75$ , for high densities. A continuous crossover between the behavior at small and large particle densities can be observed in Figure 33c. The separation as a function of  $\rho$  displays a local maximum for smaller values of the average velocity  $\bar{v}$ , but it is monotonically increasing with  $\rho$  for larger  $\bar{v}$ . The density that optimizes the separation increases with increasing  $\bar{v}$  (dashed red curve in Figure 33c). At constant  $\Delta v$  and  $\rho$ , separation decreases with increasing  $\bar{v}$ , as shown in Figure 33a and c. This happens because  $\Delta v/\bar{v}$  is the relevant quantity to consider, as already mentioned above. An absolute velocity difference  $\Delta v$  is less relevant when the two velocities are high, compared to the situation when the two velocities are low.

The channel width also influences the separation of the two components. When the channel is wide enough, the accumulation at each wall can be understood independently of the presence of the other wall. This is not the case for narrow channels, where particles expelled from one wall very soon arrive at the second wall, hindering separation. In Figure 33d, the separation is shown as function of the channel width  $L_x$ . At intermediate density  $\rho = 1$ , we observe a monotonic increase of the separation, reaching a plateau value at  $L_x > 50$ . At high density  $\rho = 1.8$ , the plateau value is reached already in smaller channels. Other factors that influence component separation, like the tumbling frequency,

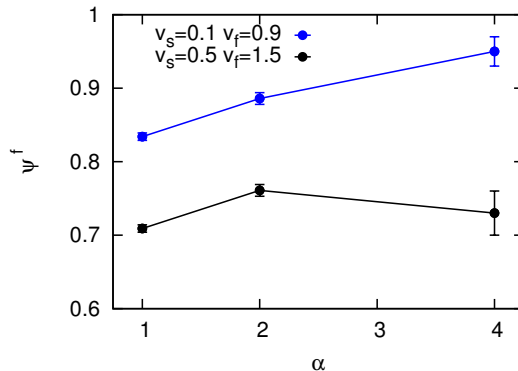


Figure 34: Separation of fast and slow particles close to the wall, quantified by  $\psi^f$  in eq. (56) as a function of particle aspect ratio.  $v_s = 0.1$  and  $v_f = 0.9$  (blue),  $v_s = 0.5$  and  $v_f = 1.5$  (black).

will be a matter of further investigation.

### Dependence of the separation on the particle aspect ratio

Although the present study is performed for elongated particles, the basics of the expulsion mechanism and the separation for particles of different velocities is expected to be valid for various particle shapes. In order to check this, we change the aspect ratio of both fast and slow particles, keeping the other parameters fixed. We do actually increase the length of the particles and decrease the number of particles in the system in order to keep the density  $\rho = lN/L_xL_y$  constant. In Figure 34 we observe that the separation exists for spherical and elongated particles, and that the separation only slightly increases with aspect ratio.

In a recent study by the group of M. C. Marchetti [110], a numerical study of mixtures of spherical particles with different radii and different velocities is performed. They observe that at same self-propelling velocities, smaller particles aggregate near the walls and bigger particles are segregated into the bulk. Increasing the velocity of the bigger particles and keeping the velocity of the small particles fixed, the tendency of the fast (and big) particles to aggregate near the walls increases: from the initial state in which small particles are at the walls (state C in Figure 35), first the mixed state is reached (state B in Figure 35), and then the fast and big particles aggregate near the walls (state A in Figure 35). At that point, the effect of the velocity difference compensates the effect of the size difference. Small particles that are also faster than the big particles will clearly aggregate at the walls even better than small particles that have the same velocity as the big particles. Preliminary simulations of a mixture of short and long rods with same self-propelling velocity show also spontaneous segregation as for small and big spheres.

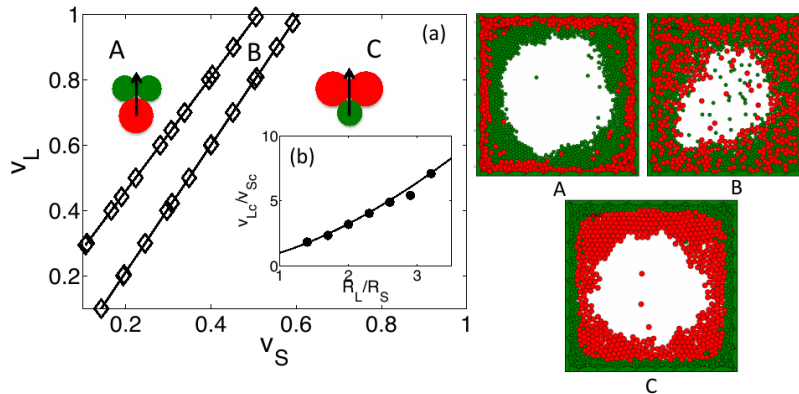


Figure 35: Left: (a) Phase diagram showing the segregated and homogeneous states as functions of the active velocities  $v_S$  and  $v_L$  (small particles are green and large ones are red online) for  $D_r = 5 \cdot 10^5$  and a total packing fraction  $\phi = 0.9$ , with each species occupying half of the packing fraction. (b) Ratio  $v_{Lc} = v_{Sc}$  as a function of the radii ratio  $R_L = R_S$ . The circles are from numerical simulation. Right: snapshots of segregated and homogeneous states. The labels A, B, C correspond to the states marked in the phase diagram. Figure and caption taken from [110].

### 4.3 Channels with Poiseuille flow

In microfluidic devices, the presence of flow is standard, such that it is relevant to extend our investigation from microchannels without solvent flow to the presence of an additional fluid flow. We therefore modify our simulation model to include the effect of an implicit solvent with a parabolic velocity profile with maximum velocity  $v_0$ . This is performed by adding to the translational and rotational velocities of each particle, the velocity and the vorticity of the flow, see Chapter 2 (Model) and Reference [57] for details. After a short introduction about upstream swimming in channels with Poiseuille flow, we first discuss single component systems, namely systems where all the particles do not differ from each other and are identical run-and-tumbling particles with length to width aspect ratio  $\alpha = 2$ , and then we focus our attention on two component systems.

In the absence of flow, particles accumulate at the wall with an angle given by parameters like the particle density, but always symmetric on average with respect to the surface normal vector [57, 62]. In the presence of flow, the interplay of self-propulsion and the vorticity field of the flow implies that the orientation of particles accumulated at the wall is almost exclusively opposite to the applied flow. This gives rise to the interesting phenomenon of *upstream swimming* at the channel walls [57, 111–114], which is only possible with self-propelled particles and not with passive tracers.

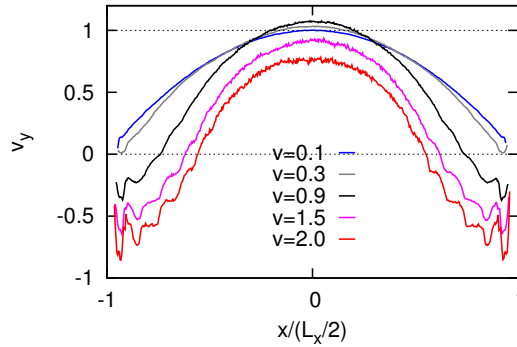


Figure 36: One component systems: velocity profiles for different self-propelling velocities. Solvent velocity  $v_0 = 1$ .

#### 4.3.1 One component systems

The upstream swimming phenomenon affects the entire particle velocity profile across the channel, shown in Figure 36. For a given flow field, upstream swimming increases with self-propelling velocity, while passive tracers simply follow the flow streamlines. Furthermore, the trajectories of single self-propelled non-tumbling particles in a parabolic flow also result in an upstream average orientation, as shown in Figure 37, which enhances the upstream swimming.

On the other hand, tumbling and collisions among particles randomize the particle orientation, such that the particle average velocity follows more easily the applied flow. Interestingly, the velocity at the channel center  $v_c$  can become larger than the applied flow  $v_0$ , see Figure 36 and Figure 38. This means that the particles are on average aligned with the flow, in contrast to the previously described effects. This effect occurs for not too small densities, and moderate self-propulsion velocities, and it is most likely related to a cooperative phenomenon. The combination of these effects can result in the non-monotonic dependence of the velocity at the channel center  $v_c$  with the self-propelling velocity, as shown in Figure 38, where the increase of  $v_c$  with density is also displayed.

Since there are particles going downstream (mostly at the center of the channel), and particles going upstream (at the walls), an interesting quantity to consider is the total particle flux, defined as

$$\phi = \int_0^{L_x} \rho(x)v_y(x)dx. \quad (57)$$

This quantity expresses the number of particles crossing a channel section in a unit of time. In the case of passive tracer particles having flat density profile  $\rho(x) = \rho$  moving in

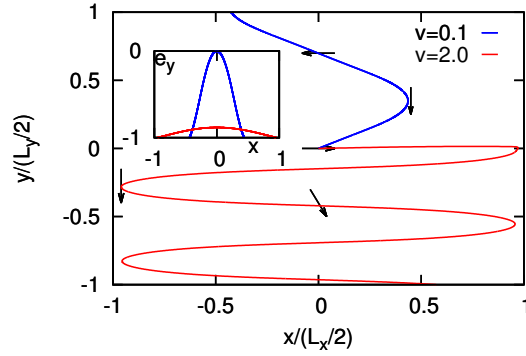


Figure 37: (Color online) Trajectories of deterministic moving (not tumbling) particles in Poiseuille flow ( $v_0 = 1$ ). Particles start at the center of the channel with horizontal orientation. Fast particles assume orientations which are always close to the upstream one, while slow particles can reach also the horizontal orientation. Arrows show orientations of particles, which are also shown in the inset.

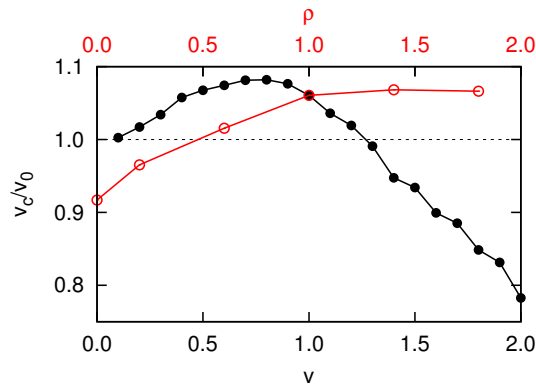


Figure 38: One component systems: Velocity at the center of the channel as a function of the self-propelling velocity (black bullets,  $\rho = 1$ ) and as a function of particle density  $\rho$  (red circles,  $v = 1$ ).

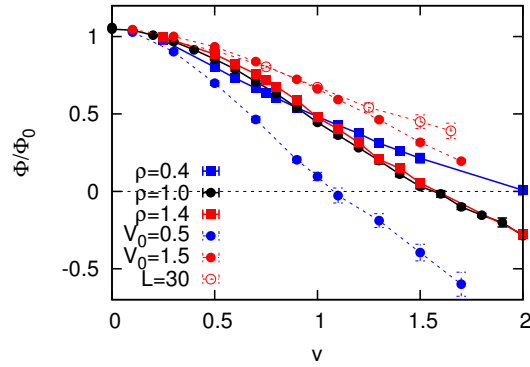


Figure 39: Normalized flux  $\phi/\phi_0$  of one-component systems as a function of the self-propelling velocity  $v$ .

a parabolic flow with maximum velocity  $v_0$ , considering that

$$\int v_y(x) dx = \int_{-L_x/2}^{+L_x/2} v_0 \left(1 - \frac{x^2}{(L_x/2)^2}\right) dx = \frac{2}{3} L_x v_0$$

the flux of passive tracers becomes

$$\phi_0 = 2\rho v_0 L_x / 3.$$

In Figure 39 the normalized flux  $\phi/\phi_0$  is displayed for various one-component systems as a function of the self-propelling velocity  $v$ . The limit of passive particles  $\phi \rightarrow \phi_0$  is reasonably well reproduced, given that the density profile is never perfectly flat in the presence of confining walls. With increasing self-propelling velocity, the flux decreases as a consequence of the increase of the upstream swimming. The dependence of the normalized flux on other system parameters is non-trivial. Increasing the average density shows a non-monotonic albeit very small variation of the normalized flux. Increasing the fluid velocity increases the normalized flux, which indicates that the particles follow the flow more the stronger it is, which is also the effect of enlarging the channel width.

### Channel without walls and with Poiseuille flow

In a recent work by the Stocker group [115] a depletion of active particles at the center of a channel with Poiseuille flow is observed. The authors understand that this depletion is only due to particle activity and the imposed flow vorticity. Inspired by this work and the considerations therein, we perform simulations of run-and-tumbling particles in Poiseuille flow without walls. We now use periodic boundary conditions not only in  $y$ -direction but also in  $x$ -direction.

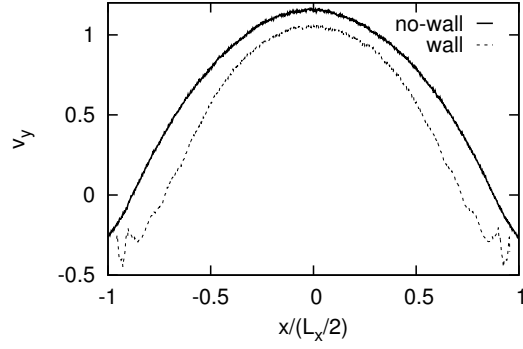


Figure 40: Velocity profiles  $v_y(x)$  of run-and-tumble particles in Poiseuille flow with and without walls.

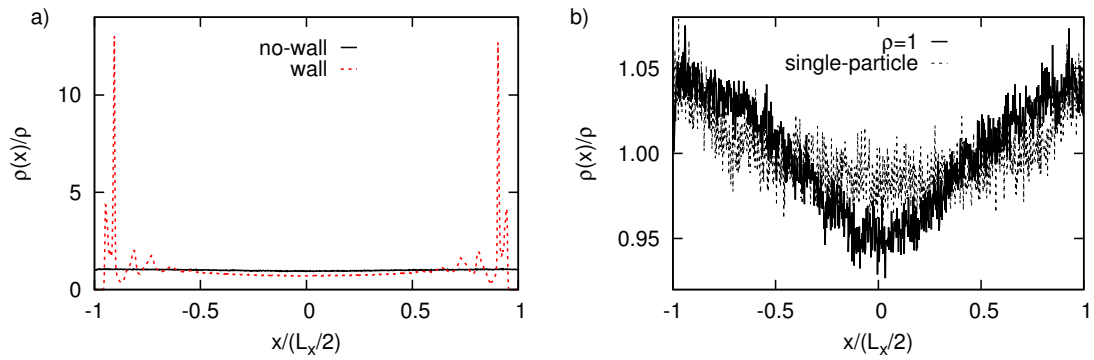


Figure 41: Local number density profiles in a microchannel with Poiseuille flow with and without walls at density  $\rho = 1$  (a). Density profiles in a channel without walls for dense system  $\rho = 1$  and single particle simulation (b).



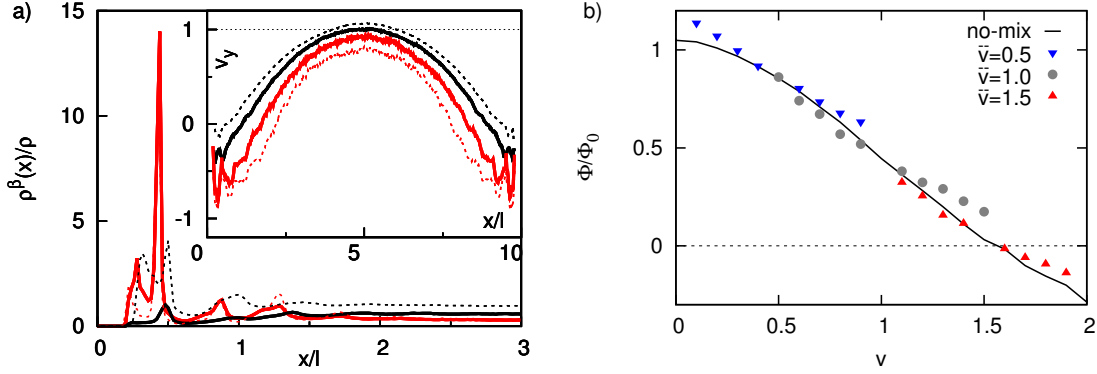


Figure 42: a) Normalized local number density of the particles center of mass in the presence of a capillary flow with  $v_0 = 1$ . Inset: Velocity profiles of each component along the channel width. Lines and parameters are the same of Figure 31. b) The line corresponds to the one-component reference flux of Figure 36, symbols to the mixture components. Four mixtures with different  $\Delta v$  are displayed for each  $\bar{v}$ . Symbols indicate  $\bar{v} = 1.5$  (▲),  $\bar{v} = 1.0$  (●), and  $\bar{v} = 0.5$  (▼). Fluxes are normalized such that  $\Delta v \rightarrow 0 \Rightarrow \phi^\alpha \rightarrow \phi$ .

As shown in Figure 40, the velocity profiles of the particles differ slightly in the two considered cases. With walls the velocity values are shifted down compared to the no-wall case. This could be due to the aligning effect of the walls which increases the upstream swimming phenomenon, which is also present without walls but less strong.

In Figure 41a we show the density profiles with and without walls. The wall-aggregation effect is clearly much stronger than the depletion induced by the flow in the absence of walls. The latter one is nevertheless clearly evident plotting the density profile of the simulation without walls only. In Figure 41b we compare two simulations without walls. One for a dense system at  $\rho = 1$  and one dilute system of a single particle  $\rho \sim 0$ . In both cases the flow induced depletion is present and is both qualitatively and quantitatively similar. We therefore exclude any relevance of density effects in the observed flow-induced depletion, which is in qualitative agreement with the results of the Stocker group.

### 4.3.2 Two component systems

The question that arises now is how the presence of flow affects the spontaneous separation in mixtures of self-propelled run-and-tumbling particles of length to width aspect ratio  $\alpha = l/a = 1/0.5 = 2$  with different velocities.

In Figure 42a density profiles are shown (see eq.(55)), which indicate that the fast particles still expel the slow ones from the near-wall region into the bulk, and that the presence of flow slightly diminishes layer formation in the proximity of the walls, similar to the one-component case [57]. The velocity profiles of each component  $v_y^\alpha(x)$  are displayed in

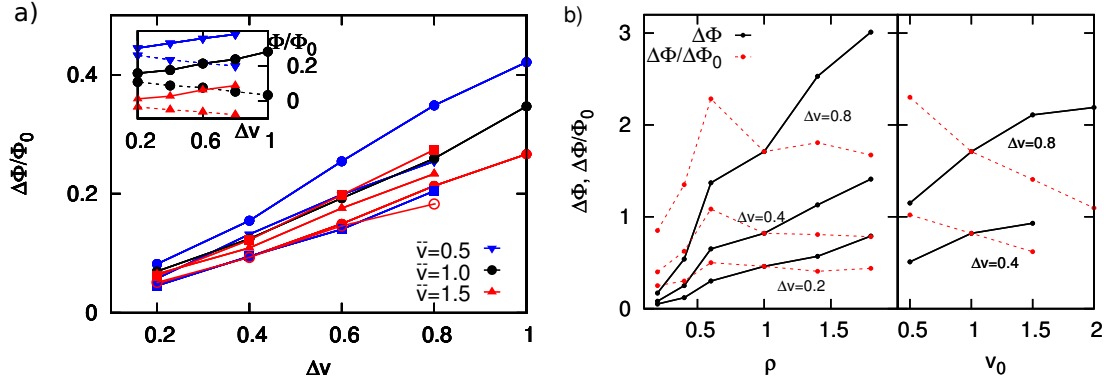


Figure 43: a) Normalized flux difference (inset: normalized flux) for two-component systems, as a function of  $\Delta v$ . Symbols are the same as in Figure 36. b) Flux difference and normalized flux difference as a function of density and fluid velocity.

the inset of Figure 42a. Both profiles differ from their counterparts in the one-component systems by getting closer to each other, which reflects the effective drag of one particle component on the other.

In a mixture, the changes in the velocity profiles translate into a slight increase of the fast particle flux relative to the single component case, while for slow particles the flux slightly decreases. This is shown in Figure 42b, where the one-component reference normalized flux is compared with the values for each of the mixed components. Only for  $\bar{v} = 0.5$ , we observe a slight flux increase for both components. In this case, the interplay between density and velocity is different, and the separation is more effective.

The separation of fast and slow particles obtained in the outflow can be characterized by the difference of the fluxes of both components  $\Delta\phi = \phi^s - \phi^f$ . This difference increases with density, fluid velocity, and channel width, similar to the normalizing flux  $\phi_0$ , and naturally also with the difference of velocities, as displayed in Figures 43a and b. Figures 43a and b show that the largest normalized flux differences occur for the smallest employed flow velocity. At that flow velocity the single-component normalized flux shows the largest decrease with self-propulsion velocity (Figure 39). As we have shown above, the mixing only slightly changes the flux values, such that the behavior of the single-component fluxes can be taken as a reference for flux differences in mixtures. An interesting consequence arising from the flux presented in Figure 39 is that for a given mixture, the applied flow velocity can be eventually be tuned to obtain a positive flux for the slow particles and a negative flux for the fast particles. For example, this can be achieved for a mixture with  $v_s = 0.5$  and  $v_f = 1.5$  and standard parameters by choosing  $v_0 = 0.5$ .

#### 4.4 Channel with Poiseuille flow and membranes

An interesting configuration to exploit the separation of self-propelled particles of different self-propulsion velocities in microcapillary flow is shown in Figure 44. It consists of two semi-permeable membranes spanned across the channel diameter at a defined channel segment. The membrane pores are assumed to be too small for the particles to penetrate, but large enough for the fluid flow to pass unhindered. Thus, in our simulations, the fluid flow is unperturbed compared to the open channel, while excluded-volume interactions are implemented for the self-propelled particles.

At the walls, the particles mostly move fast and upstream, which in the presence of the membranes leads to the accumulation of almost exclusively fast particles at the upstream membrane, as shown in Figure 44. In the center of the channel, equidistant from the walls, both particle types are present and move downstream, but slow particles are more abundant. This leads to an accumulation of a mixture of particles that is enriched in slow particles at the downstream membrane. The competition of these two effects determines the precise distribution of particles along the channel, which therefore strongly depends on the system parameters. The intrinsic distribution of self-propelled particles in the channel also translates in the accumulation at the membranes, which is much more ordered upstream than downstream.

In order to quantify the separation, we compute the percentage of fast particles at a distance  $d$  from the upstream-membrane,  $\psi_u^f$ , and the percentage of slow particles at a distance  $d$  from the downstream-membrane,  $\psi_d^s$ , which is calculated using Eq. (56) with  $d = L_y/4$ . Relevant quantities are also the total particle densities  $\rho_u$  and  $\rho_d$  in both regions. The dependence of the separation parameters and densities close to the membranes on the applied flow velocity is presented in Figure 45 for a mixture with  $v_s = 0.5$  and  $v_f = 1.5$ . In the absence of flow, there is no separation,  $\psi^\alpha = 0.5$ , and both densities are equal to  $\rho = N/A$ , which in this case is 1.25. By increasing the fluid velocity, the particles are increasingly pushed to accumulate at the downstream membrane, reaching a packing limit where neighboring particles can be slightly closer than the bead diameter due to the soft interaction potential. Interestingly, only fast particles are found at the upstream membrane for  $v_0 \geq v_s$ , while the largest proportion of slow particles is found at the downstream membrane for flow velocities a bit larger than  $v_s$ .

#### 4.5 Comparison between different noise types

The results presented until now in this chapter are obtained with the Run-and-Tumble (RnT) model. In order to judge the generality of these results, we perform simulations using Active-Brownian-Particles (ABP) and deterministically moving particles (DET). Model parameters are tuned such that a single Active-Brownian-Particle has the same rotational

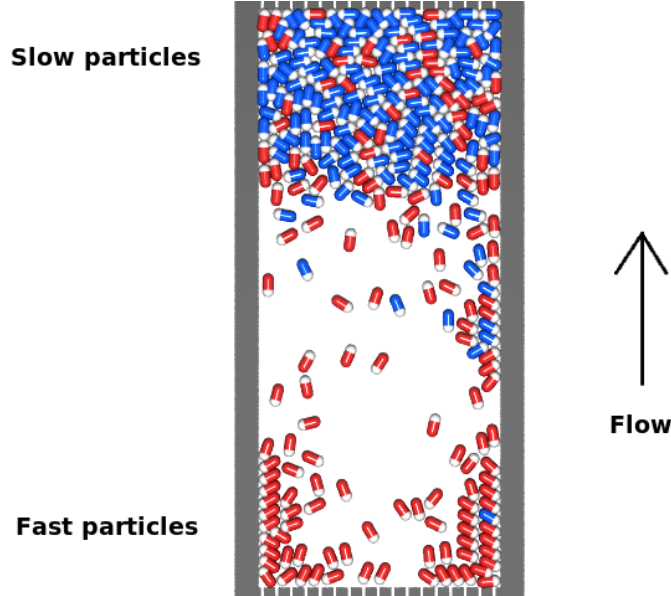


Figure 44: Simulation snapshot of the separation of fast and slow particles in a micro-channel with Poiseuille flow ( $v_0 = 1.0$ ) and membranes at the ends. Fast particles ( $v_f = 1.5$ ) are found upstream while slow ones ( $v_s = 0.5$ ) downstream.

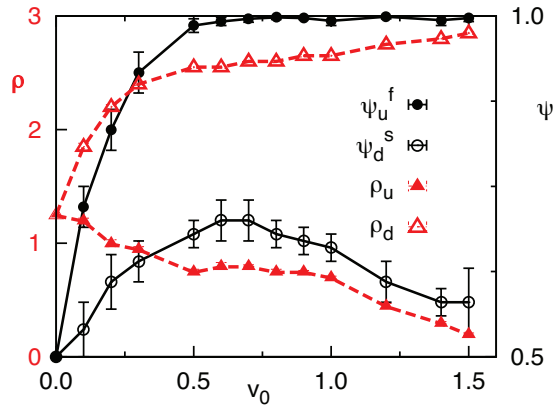


Figure 45: Percentage of fast particles in the upstream quarter of the channel  $\psi_u^f$ , and percentage of slow particles in the downstream quarter  $\psi_d^s$  as a function of the solvent velocity  $v_0$ . Total number densities in each quarters,  $\rho_u$  and  $\rho_d$ .

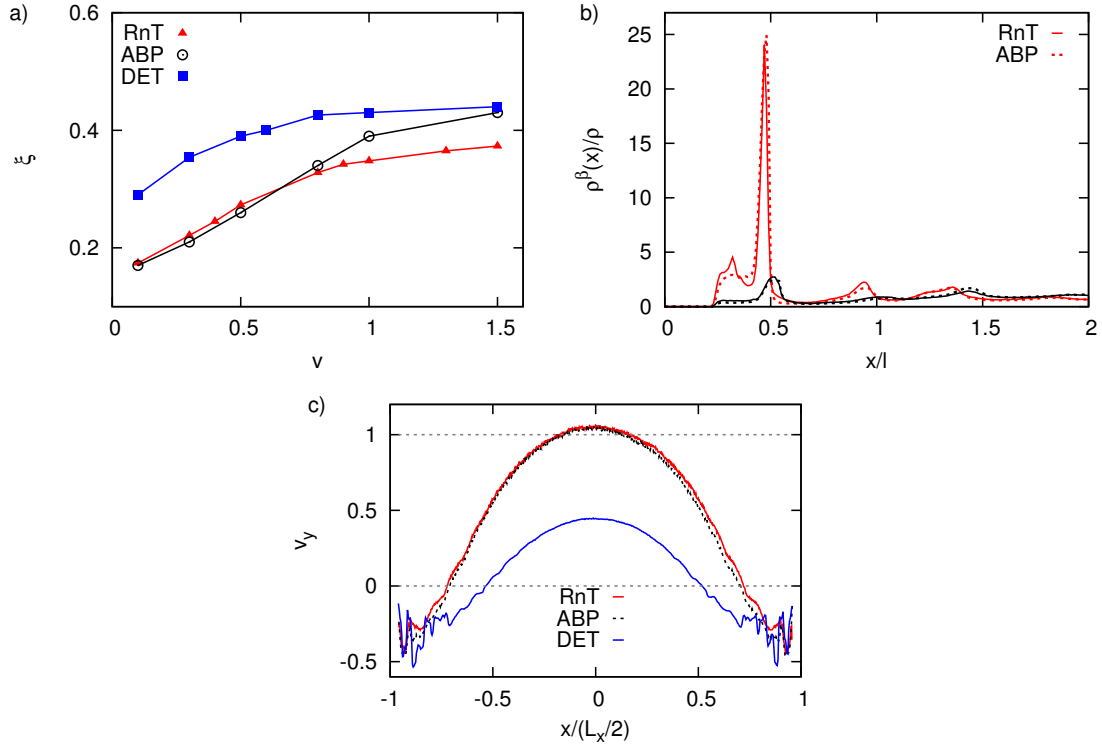


Figure 46: Comparison between deterministically moving particles (DET), Active-Brownian-Particles (ABP) and Run-and-Tumbling particles (RnT). a) Fraction  $\xi$  as a function of self-propelling velocity at different densities ( $\rho = 1$ , channel without Poiseuille flow, one-component system). b) Density profiles of fast (red lines) and slow (black lines) particles ( $\rho = 1$ , channel without Poiseuille flow, two-component system:  $v_s = 0.3$ ,  $v_f = 1.0$ ) b) Velocity profiles ( $\rho = 1$ , channel with Poiseuille flow, one-component system).

diffusion  $D_{r,0}$  as a single Run-and-Tumbling particle.

We start considering dense ( $\rho = 1$ ) one-component systems in a channel without Poiseuille flow. Figure 46a shows the fraction  $\xi$  of particles close to the walls as a function of self-propelling velocity  $v$ . The fraction  $\xi$  increases with self-propelling velocity  $v$  for all the three considered particle types. Deterministically moving particles show slightly higher fraction values than Active-Brownian-Particles and Run-and-Tumbling particles, which values almost coincide. The aggregation at the walls of deterministically moving particles is better since orientation noise is not present and only collisions with other particles can let them leave the wall. In Figure 46b we show the density profiles in a channel without solvent flow for a two-component system. Active-Brownian-Particles show almost the same profiles than Run-and-Tumbling particles. This is valid for both fast and slow particles of the two-component system.

Velocity profiles of a one-component system in a channel with Poiseuille solvent flow

are shown in Figure 46c. Also in this case there is almost no difference between Active-Brownian-Particles and Run-and-Tumbling particles. Deterministically moving particles show a quite different velocity profile. Particles tend to stay more time in upstream swimming orientation, since in the absence of noise only collisions can change the particle orientation. The velocity of deterministically moving particles results therefore to be lower than the velocity of Active-Brownian-Particles and Run-and-Tumble particles, especially at the center of the channel.

Run-and-Tumbling particles and Active-Brownian-Particles show very similar results, both for one-component systems and for two-component systems, both with and without Poiseuille solvent flow. We can therefore conclude that the results obtained in this chapter about motility-sorting in micro-channels are not dependent on the specific nature of the employed model, but have rather a general validity for different kinds of self-propelled particles.

#### 4.6 Summary

The possibility to sort and separate the different particle types of an heterogeneous mixture always interested and fascinated scientists. To develop sorting techniques is very important both for theoretical and for practical aims. A two-component mixture can be composed by two different types of passive particles, one passive and one active type, or two different active particles. We studied here mixtures of active run-and-tumble particles which differ only in their self-propelling velocity. Their motion in microchannels has been investigated, both with and without solvent Poiseuille flow. In order to better understand the physics of two-component mixtures, one-component systems have been analyzed first.

We measured several quantities like the particle density profiles along the channel, the particle orientation, and the fraction of particles close to the walls. For one-component systems of active-particles in microchannels, we have found particle aggregation at the channel walls, phenomenon which increases with self-propelling velocity. For two-component systems of active particles which differ only in their motility, it turns out that the presence of a plane wall, like the one of a microchannel, is sufficient to induce a spontaneous segregation of the two different components. Slow particles are shown to be expelled by the fast neighboring particles from the channel walls into the bulk, which results in the spontaneous segregation of the two species. Separation always grows with the velocity difference, but the dependence on other parameters is less obvious. Separation is maximized for low average particle velocities, large channels, and intermediate densities. This mechanism can be of importance to achieve particle sorting, e.g. via a pipette or a microfluidic device.

In the presence of capillary Poiseuille flow in the microchannel, one-component systems show upstream swimming at the channel walls. We measured density profiles, velocity

profiles, and the related total particle fluxes. The investigation of their dependence on system parameters like self-propelling velocity and particle density helped us to better understand the behavior of two-component mixtures. In this case, since particles with different velocities have different fluxes, the fluid velocity can be tuned to segregate slow particles downstream and fast particles upstream. In the presence of flow, separation grows with fluid velocity, channel width, and density, while there is almost no dependence on the average particle velocity. Moreover, we extend our study of the separation of fast and slow particles in a channel with flow to a channel with flow and membranes at its ends. The solvent can flow through the membranes which block the particles only. The separation of fast and slow particles turns out to be maximal for fluid velocities slightly higher than the slow-particle velocity.

In order to ensure the generalization of our conclusions beyond the details of our model, we have performed additional simulations which show that the expulsion mechanism also occurs in mixtures of spherical particles and with other swimming strategies like Active-Brownian-Particles. Qualitatively, the results are expected to persist in three-dimensional structures, as is the case for a single swimmer in Poiseuille flow [113].

Our results should be of considerable theoretical and practical interest, because they provide new insights into active matter and non-equilibrium systems. Applications of these results can be envisioned for the development of multi-stage cascade microfluidic lab-on-a-chip devices, which could then be an alternative to the use of laser traps or other external fields, for sorting particles with different motilities.





---

## 5 Run-and-Tumbling particles in ratcheted-microchannels

In this chapter the motion of self-propelled run-and-tumbling particles in channels with asymmetric ratchet-like walls is investigated and discussed. After introducing ratchet phenomena, we first study the limit of single particles, and afterwards dense systems. Finally we briefly extend the investigation to analyze the separation in mixtures of slow and fast particles.

### 5.1 Introduction

A ratchet effect is the rectification of random motion into directed motion. To obtain directed motion, two key ingredients are necessary. First, the time-reversal symmetry needs to be broken, which implies in particular that the system needs to be out of thermodynamic equilibrium. The second requirement is to break a spatial symmetry, which will define the direction of motion. This breaking of spatial symmetry can actually also happen via a spontaneous symmetry-breaking mechanism [116].

A static asymmetric potential is not sufficient to rectify the motion of Brownian particles, since spatial symmetry is broken but not time-reversal symmetry. A flashing asymmetric potential turns out to be sufficient, i.e. a potential which varies with time. The variation with time and the interplay of it with the asymmetric potential allow then the directed motion. In other words, "broken symmetry and time correlations are sufficient ingredients for transport" [117]. Examples of such systems are reported in References [117–119].

In contrast to Brownian particles, self-propelled particles, or active particles, continuously convert stored energy in kinetic energy, and are therefore intrinsically out of thermodynamic equilibrium, such that only space symmetry has to be broken in order to rectify their random chaotic motion. Several routes have already been proposed very recently [120–122]. In the following, we present the most relevant examples.

A static asymmetric potential, introduced by laser beams, is sufficient to rectify the random motion of active particles [123, 124]. The asymmetric potential is made by two

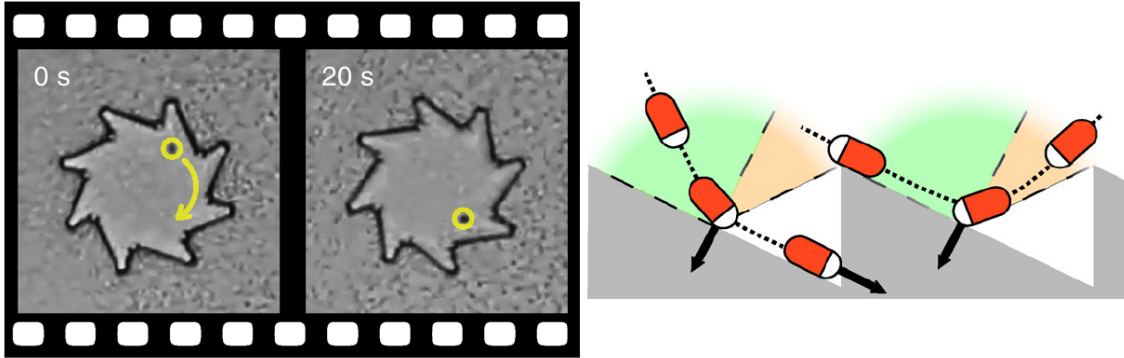


Figure 47: Experimental images of the asymmetric micro-wheel ratchet motor. Particles that arrive at a wall do align to it. Because of the wheel asymmetric geometry there are more particles moving towards the inner corners of the wheel, where particles push the wheel forward. Figure taken from [58].

potential segments, one of those is steeper than the other. Particles are blocked from the steeper potential segment, which is too steep compared to the self-propelling force and can not be overcome. Particles can overcome the other less steep potential segment and therefore a particle flux in one direction arises.

Similarly, an asymmetric micro-gear immersed in the bacterial bath spontaneously starts to rotate in one direction. Besides thermal fluctuations, a clear net rotation in one direction has been shown both numerically [56] and experimentally [58, 125]. This happens because when one particle hits a wall, the particle aligns with the wall, moving in one or the other direction depending on the incoming direction, as shown in Figure 47. Since the permitted incoming angle interval for which the particle then arrives at the inner corner of the gear is larger than the angle interval for which the particle then goes away from the gear, it is reasonable that bacteria aggregate and accumulate in inner corners of the gear pushing it forward. This is also what we expect, since, as we also discuss in other Chapters, active particles have the property to accumulate near walls [57, 61, 62, 106–109].

Another similar ratchet effect for self-propelled particles is obtained by an inhomogeneous density distribution of bacteria generated by asymmetric walls [126]. More precisely, a wall of funnels exploits the wall aggregation and wall alignment effects of the active particles. Because of the wall asymmetry, the particles cross the funnel preferentially in one direction, such that when the steady state is reached many more particles are in one region compared to the number of particles that are in the other region, see Figure 48.

Interestingly, it is also possible to obtain ratchet effects for self-propelled particles in symmetric potentials [127], in case that the self-propelling velocity of the particles varies with position and/or time. In this case the (asymmetric) dependence of the velocity on the

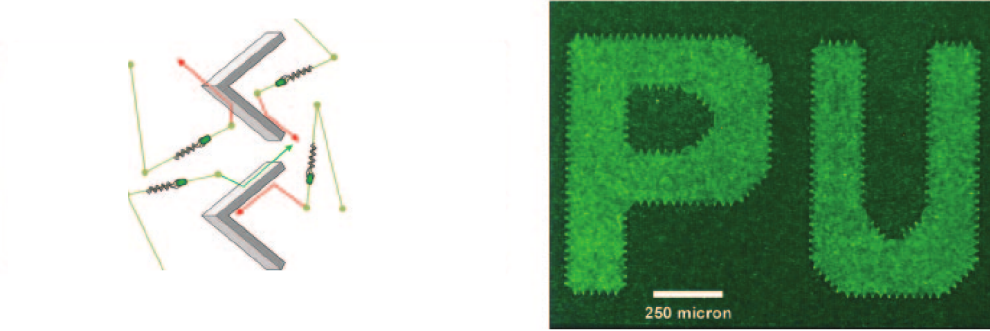


Figure 48: Left: Sketch of a wall of funnels, which in combination with active particles results into a particle flux to the right. Right: experimental image, high and low density zones are obtained delimiting the desired area with walls of funnels. Figure taken from [126].

position plays the role of the symmetry breaker, while the activity of the particles plays the off-equilibrium role.

We investigate here the motion of run-and-tumbling particles in channels with asymmetric ratchet-like walls. This situation is different from the systems previously discussed, since the wall asymmetry is intended to induce particle flux and not separation. We extend the work by the group of Marchesoni [128], where also particle flux is obtained in an asymmetric ratchet channel, to elongated particles and different ratchet geometries. We study geometries which are of particular relevance in the design of microfluidic lab-on-chip devices, where the manipulation, the transport, the control and the directed motion of particles has to be achieved. Important to emphasize is that in the asymmetric channel geometry here discussed, a directed motion is obtained without the use of laser fields or other external invasive force fields.

## 5.2 Geometry and observables

Our simulation model considers run-and-tumbling particles in two dimensions as those already introduced in Chapter 2. Similar to Chapter 4, here a channel is simulated by considering periodic boundary conditions along the x-direction and asymmetric walls at  $y = \pm L/2$ . The walls, both the plane symmetric part and the asymmetric parts, are simulated using beads fixed in space. These fixed beads have diameter  $a$  similar to the beads which form the self-propelled particles. They are positioned such that two neighboring beads have their centers at distance  $a$ . In contrast to Chapter 4, walls are here not smooth and particle locking at walls can happen. Particles can remain blocked between two beads of a wall until a tumbling event unlocks them. The ratchet character of the channel is introduced with three different asymmetric structures, which we call arm-geometry, wedge-geometry and arc-geometry, see Figure 49. The arm-geometry is constructed with walls which consist of a plane (symmetric) wall and asymmetric arms. These arms of fixed length  $r = 5$  are attached with an angle  $\theta$  at the plane walls, at certain positions  $x$ , such that the distance in x-direction between two neighboring arms is  $d$ , as sketched in Figure 49a. The wedge-geometry is constructed adding to the arm-geometry a vertical wall connecting the end of the arm with the channel wall, as shown in the sketch in Figure 49b. The arc-geometry consists of a channel with curved walls inspired by the experimental work of Reference [129]. The sketch of the geometry is shown in Figure 49c.

We are interested in investigating the ratchet effect, i.e. a non-zero average velocity of the particles. The system symmetry is broken in x-direction, given the direction of the arms we expect a positive average x-velocity. We therefore measure the x-component of the velocity and take ensemble and time averages, excluding the initial time interval during which the system reaches the steady state. The length of the simulation and of the equilibration time actually depend especially on tumbling frequency. Ensemble averages are typically taken for 3200 particles in the single-particle simulations, while for dense systems the number varies with density. We denote this ensemble and time average with  $\langle v_x \rangle$ . Moreover, to better understand the complete phenomenology, we also measure other quantities like the percentages of particles in the bulk and their average x-velocity. Velocity and density profiles along the channel width are also measured. In the following we study how these quantities depend on the system parameters like the arm angle  $\theta$ , the distance between arms  $d$ , the channel width  $L$  and the tumbling frequency  $\nu$ .

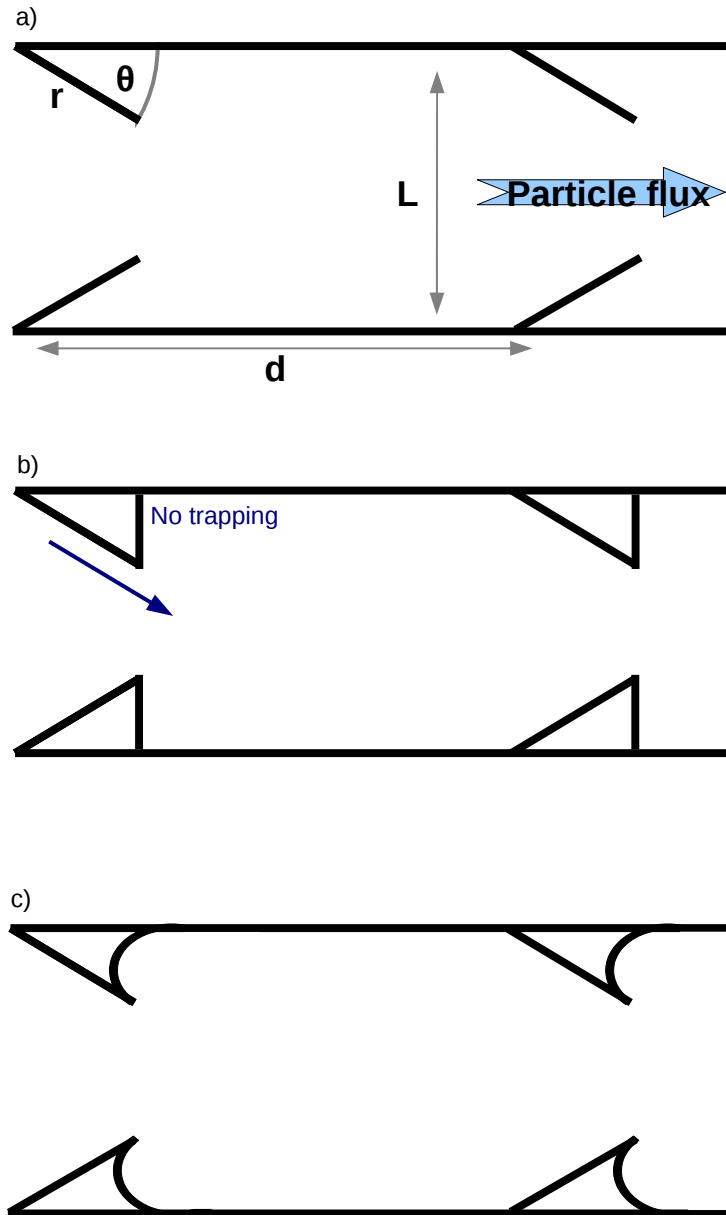


Figure 49: Sketches of the different ratchet-geometries: a) arm-geometry, b) wedge-geometry, c) arc-geometry.

### 5.3 Single-Particle Simulations

In order to understand the fundamental physics of the motion of self-propelled particles in ratchet-like channels, we start our study considering the dilute limit of single-particle simulations. The dilute limit is interesting by itself, since low particle concentrations are frequent. Moreover it serves as basis to understand the concentrated systems.

Here we first discuss results for run-and-tumbling particles of aspect ratio  $\alpha = 2$ . Such particles are similar to *E. coli* bacteria which are often used in experiments. Later we discuss also results for particles of aspect ratio  $\alpha = 1$ , i.e. for spheres, which, as we will show and discuss, behave very differently than elongated particles. Elongated particles align with walls, since at  $\alpha > 1$  steric interactions in collisions with walls induce alignment, while the orientation of spheres does in our model not depend on the interaction with other particles or with walls.

#### 5.3.1 Arm-geometry

##### Particle trapping at low arm angle

In order to better understand the dependence of the average directional-velocity on the arm angle, here we show and discuss the particle trapping at low arm angle, an important result which is independent of tumbling frequency.

At low arm angle ( $\theta < \theta_c \sim 30^\circ$ ), all particles that reach the acute angle formed by the wall and the arm get trapped into it, because of their elongation they can not escape from it. The self-propulsion keeps the particle close to the walls that form the angle and the applied torque during the tumbling event is not sufficient to reorient the particle if the angle is lower than the critical angle  $\theta_c \sim 30^\circ$ . Increasing the angle  $\theta$ , since the particle has now more space to rotate, a strong torque can reorient the particle such that the particle can escape from the angle. The escape probability from the acute angle is shown in Figure 50. These data are obtained as follows. A particle is positioned in the acute angle pointing towards it such that it does not move. A tumbling event is simulated, as usual with random torque uniformly distributed such that a free particle would rotate by an angle between  $-\pi$  and  $+\pi$ . After the tumbling event the particle may have escaped from the acute angle or not. Performing ensemble averages, namely repeating the simulation for many particles, we obtain the probability  $p$  shown in Figure 50 as number of escaping particles divided by the the total number of runs. For  $\theta < 30^\circ$ , as already discussed, the escape probability is zero and increases then almost monotonically (except for a slight non-monotonic interval between  $55^\circ$  and  $65^\circ$ ) to the probability value of 0.7 at  $\theta = 90^\circ$ .

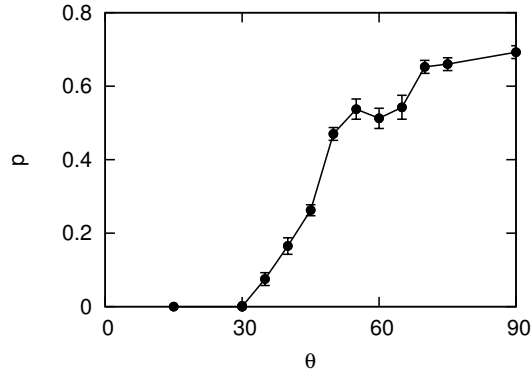


Figure 50: Escape probability  $p$  from the acute angle between arm and channel wall.

### Trajectories in the non-tumbling limit

In order to better understand the dependence of the average velocity on the system parameters, we first introduce the three possible types of trajectories of particles moving in a ratcheted microchannel with the arm-geometry. These trajectories are depicted in Figure 51 and represent the behavior of deterministically moving particles, which corresponds to run-and-tumbling particles in the limit of very low tumbling frequency.

Let's consider a particle moving parallel to one arm towards the center of the channel. If it does not tumble it arrives on the other side of the channel with the same orientation. Depending on the particular geometry of the ratchet system, namely on the distance between arms  $d$ , the angle  $\theta$ , and the channel width  $L$ , it may hit an arm or the wall. If it hits one arm, the angle  $\theta$  determines whether the particle gets aligned parallel to the arm pointing towards the center of the channel or pointing towards the channel wall:

- I:  $\theta_c < \theta < 45^\circ$ , the particle hits an arm and gets aligned parallel to it pointing towards the center of the channel. This leads to a high flux, since particles are performing diagonal trajectories always moving to the right. Therefore the average velocity is expected to be proportional to the cosine of the arm angle,

$$\langle v_x \rangle = vQ_m \cos(\theta). \quad (58)$$

where  $v$  is the self-propelling velocity and  $Q_m$  is the mobile fraction, i.e. the fraction of particles that are moving to the right and are not stuck in the acute angle. Depending on the initial condition, some particles reach the acute angle and will never escape from it in the non-tumbling limit.

- II:  $\theta > 45^\circ$ , the particle hits an arm and gets aligned parallel to it pointing towards the channel wall. The particles are no longer persistently moving to the right, after

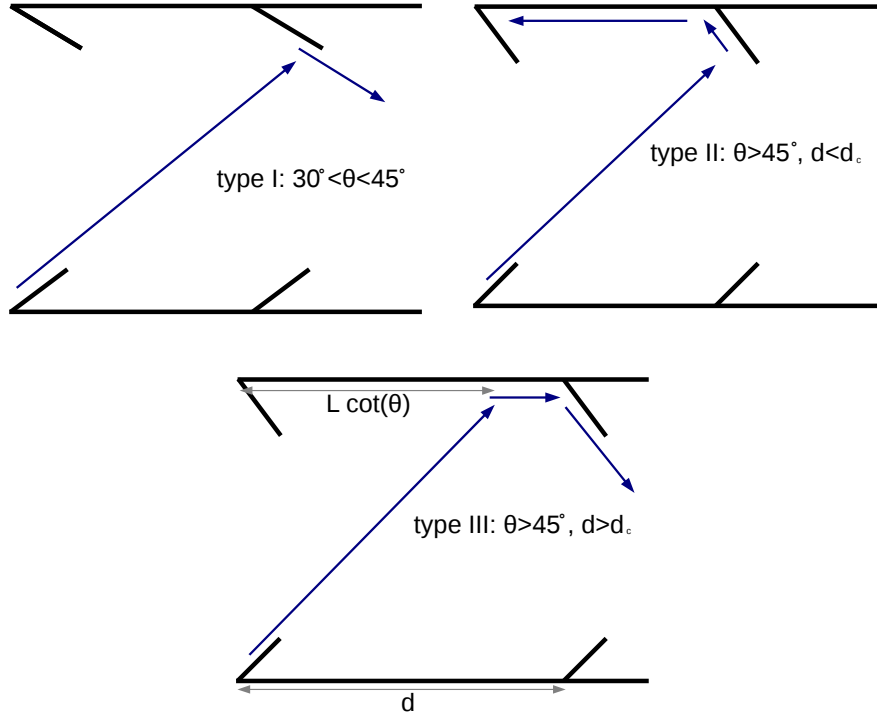


Figure 51: Sketches of trajectories of non-tumbling particles: I At  $30^\circ < \theta \leq 45^\circ$  particles hit an *arm* and get aligned with it towards the center of the channel. II At  $45^\circ < \theta$  ( $L = 20$  and arm distance  $d \leq 12$ ) particles hit an *arm* and get trapped back in the acute angle of the neighboring *arm*. III At  $45^\circ < \theta$  ( $L = 20$  and arm distance  $d > 12$ ) particles hit the channel wall and get then aligned with the *arm*.

the collision with the arm particles move back to the acute angle and get out of it only if they tumble, with an escape-trajectory-angle within the interval  $(0, \theta)$ . The average velocity is therefore expected to be lower than in case I, dominated by the escape events from the acute angle. It is expected to be proportional to the product of tumbling frequency  $\nu$  and escape probability  $p$  (average velocity zero for non-tumbling particles)

$$\langle v_x \rangle \sim \nu p. \quad (59)$$

In case I, the particle moves along one arm and its trajectory angle has to be equal to the arm angle  $\theta$ . But when the particle leaves the arm, for a short time only the tail half of the rod-particle feels a force from the arm, which lets the particle assume a trajectory angle slightly lower than  $\theta$ , as shown in Figure 52.

If instead of hitting an arm the particle hits the channel wall, then the particle will align with it in the direction of the flux and then arrive at the next arm aligning with it, independently on the angle  $\theta$ :



- III: the particle hits the channel wall instead of hitting an arm. The average velocity is therefore increased by the horizontal contribution. The traveled distance in the channel in diagonal orientation is  $L \cot(\theta)$  and the horizontal distance  $d - L \cot(\theta)$ , such that the resulting average velocity in the non-tumbling limit reads

$$\begin{aligned} \langle v_x \rangle &= [vQ_m \cos(\theta)] \frac{L \cot(\theta)}{d} + [vQ_m] \frac{d - L \cot(\theta)}{d} \\ &= \frac{vQ_m}{d} (L \cot(\theta) \cos(\theta) + d - L \cot(\theta)) \end{aligned} \quad (60)$$

which tends to  $vQ_m$  for  $d \rightarrow \infty$ .

A particle can hit the channel wall instead of an arm only if the distance between arms  $d$  is larger than the arm length  $r$ , namely only if  $d > r$ . How the average x-velocity depends on the distance between arms  $d$  will be discussed in the next paragraphs.

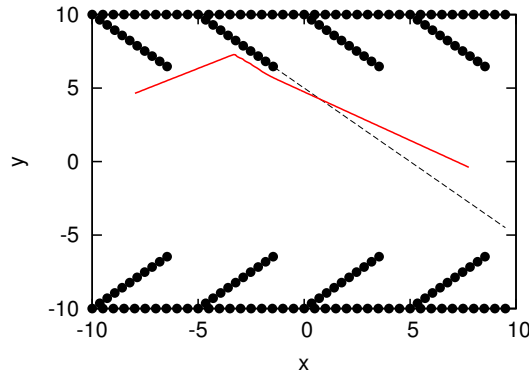


Figure 52: Trajectory of a (non-tumbling) particle colliding with an arm that has angle  $\theta = 45^\circ$  with the wall. After aligning with the arm the particle leaves the arm with a trajectory-wall angle lower than arm-wall angle.

### Dependence of the average velocity $\langle v_x \rangle$ on the arm angle $\theta$

The average velocity  $\langle v_x \rangle$  is measured in the arm-geometry for different arm angles and tumbling frequencies. At arm angle  $\theta = 0^\circ$  and  $\theta = 90^\circ$  symmetry is restored such that no net flux is expected. Therefore there has to be a non-monotonic dependence on the arm angle. The angle that maximizes the velocity depends on tumbling frequency, as shown in Figure 53. We notice also that at low angles,  $\theta \leq \theta_c \sim 30^\circ$ , all the particles get trapped in the acute angle formed by the wall and the arm, as previously discussed, and zero velocity is measured.

In Figure 53, we notice that at low frequency  $\nu = 0.001$  the flux increases from  $\theta = 30^\circ$  to  $\theta \simeq 42^\circ$ , in contrast with the cosine behavior of Eq.(58). Besides the fact that Eq.(58)

is valid in the non-tumbling limit and our tumbling rate is finite, increasing  $\theta$  the escape probability  $p$  from the acute angle increases. More particles that are blocked there can escape and contribute to the flux increasing the mobile fraction  $Q_m$ . From  $\theta = 42^\circ$  to  $\theta = 44^\circ$  we observe a slight decrease of the flux. A strong decrease is observed for angles  $\theta \geq 45^\circ$ , where the trajectory type changes from I to II.

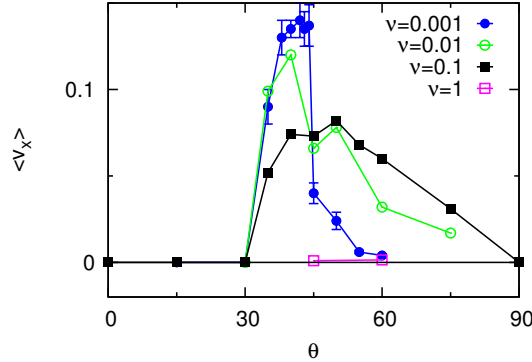


Figure 53: Average x-velocity as a function of arm angle  $\theta$ .  $L = 20$ ,  $d = 5$ .

### Dependence of the average velocity on the tumbling frequency and channel width

The value of the angle that maximizes the average velocity depends on the system parameters like the tumbling frequency, as shown in Figure 53. The average distance by which the particles moves between two tumbling events is called mean free path  $\lambda$ , which actually is the inverse of the tumbling frequency times the self-propelling velocity,  $\lambda = v/\nu$ . The dependence of the average velocity on the frequency is shown in Figure 54. At high enough frequency it tends to zero, since particles change direction so frequently that they can be considered as passive Brownian particles.

For almost all considered arm angles  $\theta$  the dependence of the average velocity on the tumbling frequency  $\nu$  is non-monotonic, as shown in Figure 54. For arm angles  $\theta \geq 45^\circ$  and low frequency, the particles are on trajectory type II and the velocity is therefore very low. Increasing the tumbling frequency  $\nu$  the particles escape more often from the acute angle and therefore the velocity increases as expected, see Eq.(59). If  $\nu$  is further increased, the velocity decreases because particles can be considered passive Brownian particles, as already discussed. At low frequency ( $\nu = 0.001$ ) the maximal velocity is obtained at arm angle  $\theta = 40^\circ$ . Only at  $\theta = 40^\circ$  the dependence of the flux on the tumbling frequency  $\nu$  is monotonically decreasing. That happens since at  $\theta = 40^\circ$  the motion is of type I and the escape probability from the acute angle  $p$  is high enough such that low frequency leads to the maximal velocity. Interestingly this does not happen at  $\theta = 35^\circ$ , where the velocity

first increases with frequency. This happens since at  $\theta = 35^\circ$  the escape probability  $p$  from the acute angle is still quite low, many particles are still trapped and an increase of the tumbling frequency leads to more escape events.

The variation of the tumbling frequency is strongly related to the variation of the channel width, since the relevant quantity to consider is the channel-width to mean-free-path ratio  $L/\lambda = L\nu/v$ . An increase of the tumbling frequency should be almost equivalent to an increase of the channel width. Increasing the channel width  $L$  and increasing the mean free path  $\lambda$  keeping the ratio constant, we notice that the flux does not stay unchanged, but slightly increase, as shown in Figure 55. This happens since increasing the channel width, we also increase the mean-free-path of the particles, but do not change the distance between arms  $d$ . Thus not every length scale in the system is increased simultaneously in order to keep it self-similar.

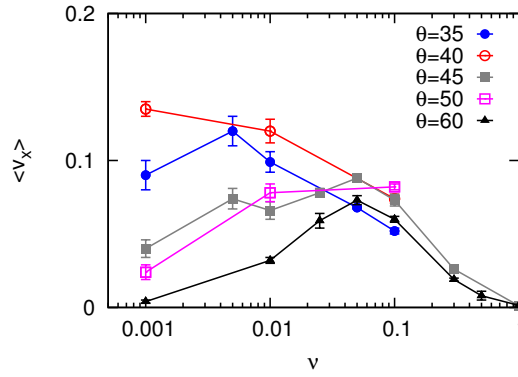


Figure 54: Average x-velocity as a function of tumbling frequency  $\nu$ .  $L = 20$ ,  $d = 5$ .

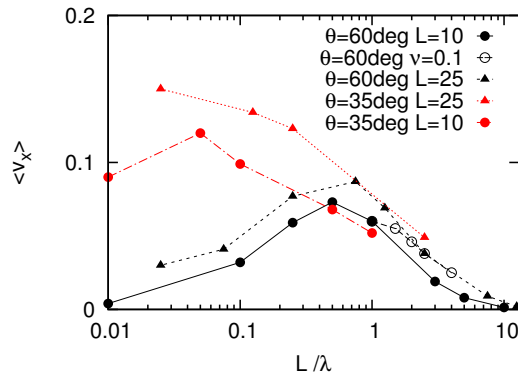


Figure 55: Average x-velocity as a function of channel width  $L$  times tumbling frequency  $\nu$  (namely channel width  $L$  by mean free path  $\lambda$ )  $L\nu = L/\lambda$ .

**Dependence on the distance between arms  $d$** 

A change of the distance between two neighboring arms  $d$  at low tumbling frequency and arm angle  $\theta > 45^\circ$  leads to a sudden change between trajectory type II and trajectory type III. This results in a sudden increase of the measured average x-velocity, since particles will now not be deviated back by the arms. We clearly observe the crossover at  $\nu = 0.001$  and  $\theta = 60^\circ$ , as shown in Figure 56. The increase is in qualitative agreement with Eq.(60). From the data shown in Figure 56, we notice that the distance  $d$  between arms has major importance only at low frequencies. In this limit, low angles show a slight flux increase with increasing  $d$ , while for high angles there is a sudden and larger increase. The distance in x-direction that particles run until they reach the opposite wall is  $\cot(\theta)$ . If the distance between arms is smaller,  $d < \cot(\theta)$ , only trajectory type II is possible. If instead the distance between arms is larger, namely if  $d > \cot(\theta)$ , particles will perform trajectory type III. Therefore we can define a critical arm distance  $d_c = \cot(\theta)$ , which varies with the arm angle  $\theta$ . As shown in Figure 56, the transition happens for  $d > 12$ , which is in good agreement with the expected value  $\cot(\theta) = 11.5$ .

On the other hand, at low angles particles are not going back after the collision with the arm, and so an increase of the arm distance  $d$  does not lead to a sudden increase of the velocity, but rather to a steady increase due to the longer completely horizontal trajectories that particles perform along the channel wall. The crossover is now not from trajectory type II to trajectory type III, but from trajectory type I to trajectory type III.

The presented phenomenology is valid at low tumbling frequency. At higher frequencies ( $\nu = 0.1$ ) the mean free path of the particles is smaller, particles do not so often arrive on the other side of the channel, and therefore changing  $d$  does not lead to significant changes in the average velocity. Actually the average velocity is expected to vanish in the limit of infinite arm distance ( $d \rightarrow \infty$ ), since that case is equivalent to a simple symmetric channel without asymmetric ratchet-like walls. The transition to this regime seems to occur at much larger arm separations than those investigated here.

**Dependence on the phase shift between the arms on the two walls**

A natural and interesting question is whether the relative position between arms on the upper and lower wall is an important parameter to vary in order to increase the ratchet effect. We call phase shift  $s$  the relative position between arms on the upper and lower wall. Similarly as a change of the distance between arms  $d$ , a change of the phase shift between the two walls can lead to a change between trajectory type II and III. As already mentioned, at distance between arms  $d = 5$  trajectory type III is not possible, since in that case the arm length  $r$  equals the distance  $d = r = 5$ , and the geometry makes trajectory type III impossible.

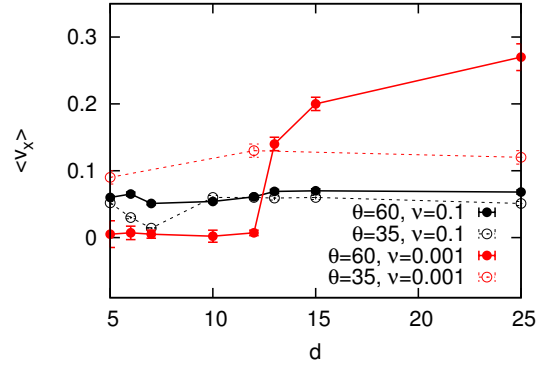


Figure 56: Average x-velocity as a function of arm distance  $d$ .

The average velocity is analyzed as a function of the phase shift  $s$ . Phase shift  $s = 0$  refers to the situation in which arms of both walls are exactly opposite to each other. Similarly,  $s = d/2$  corresponds to arms exactly in between the arms of the opposite wall. Due to the symmetry of the system it is necessary and sufficient to study the interval  $0 < s/d < 0.5$ .

In Figure 57 the velocity as a function of phase shift for arm distance  $d = 10$  and  $d = 15$  is shown. The employed arm angle is  $\theta = 60^\circ$  and the tumbling frequency is  $\nu = 0.001$ . At arm distance  $d = 10$  the velocity is low without any phase shift, since the trajectory is of type II. Increasing the phase shift, we notice that sudden increase of the velocity at phase shift  $s/d \sim 0.4$  ( $s \sim 4$ ), reflecting a sudden change from trajectory type II to type III. On the other hand, at arm distance  $d = 15$ , at zero phase shift the trajectory type is already III. An increase of the phase shift turns out to be have the opposite effect in this case, the velocity suddenly decreases at  $s/d \sim 0.2$  ( $s = 3$ ), reflecting a sudden change from trajectory type III to type II. We can therefore conclude that the phase shift  $s$  allows the system to switch between two types of behaviors. One behavior is dominated by trajectory type III in which the average x-velocity in the channel is significant. The second behavior is dominated by trajectory type II, and the average velocity is practically vanishing. This effect could in fact be used as a switch in a device with movable walls.

### Velocity and density profiles

Until now we have characterized the induced flux as an average quantity in the channel. It is actually also interesting to determine if and how it is distributed across the channel width. In Figure 58a we show a velocity field at arm angle  $\theta = 40^\circ$  and tumbling frequency  $\nu = 0.001$ . The x-component of the velocity is shown as a function of the position in the channel. The velocity is positive at the center of the channel and slightly negative between the arms, close to the walls. The highest value of the velocity is observed near the ends of

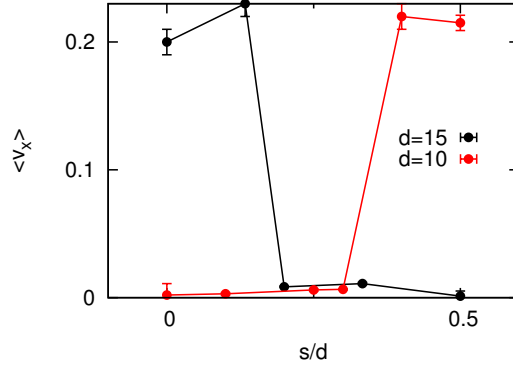


Figure 57: Average x-velocity as a function of the phase shift  $s$  between the arms on the two walls for arm distance  $d = 10$  and  $d = 15$ . Arm angle  $\theta = 60^\circ$  and tumbling frequency  $\nu = 0.001$ .

the arms. Similarly, in Figure 58b velocity profiles along the channel width  $v_x(y)$  are shown. Two velocity profiles are shown, for  $\theta = 40^\circ$  both at high and at low tumbling frequency  $\nu$ . The average velocity is higher for low frequency, as we also know from Figure 53. Besides the described behavior close to the walls, the velocity profiles are remarkably flat. This means that there is no significant variation of the flow across the channel. This can be understood due to the nature of the motion and it is in contrast to the common parabolic flow profile in a channel induced by the presence of an external flow. At the center of the channel, the velocity may slightly decrease because of tumbling events, as clearly happens at higher frequency.

Figure 58c shows a profile of the local number density of the particles centers of mass  $\rho(y) = n(y)/L_x\Delta y$ , where  $n(y)$  is the number of particles in the bin of width  $\Delta y$  centered at position  $y$ . For tumbling frequency  $\nu = 0.1$  and arm angle  $\theta = 40^\circ$ , there are two main peaks close to the walls, where approximately 75% of the particles are staying in the acute angle until a tumbling event occurs.

### Average velocity in the bulk and percentage of particles in the bulk

The velocity and density profiles shown in the previous paragraph helped us to understand if the transport is different close to the walls and in the channel center. In order to gain more understanding in this respect, we measure the average x-velocity  $\langle v_x \rangle_b$  in the bulk and the normalized average density  $\rho_b/\rho$  of particles in the bulk (which is 2 if all particles are in the bulk, 1 if the distribution is homogeneous, and 0 if all particles are close to the walls), as shown in Figure 59.

We define bulk as the region for which the distance from the channel center is less than  $b$  with  $b = (L - 2r)/2$ , which for the most standard parameter employed here is  $b = 5$ .

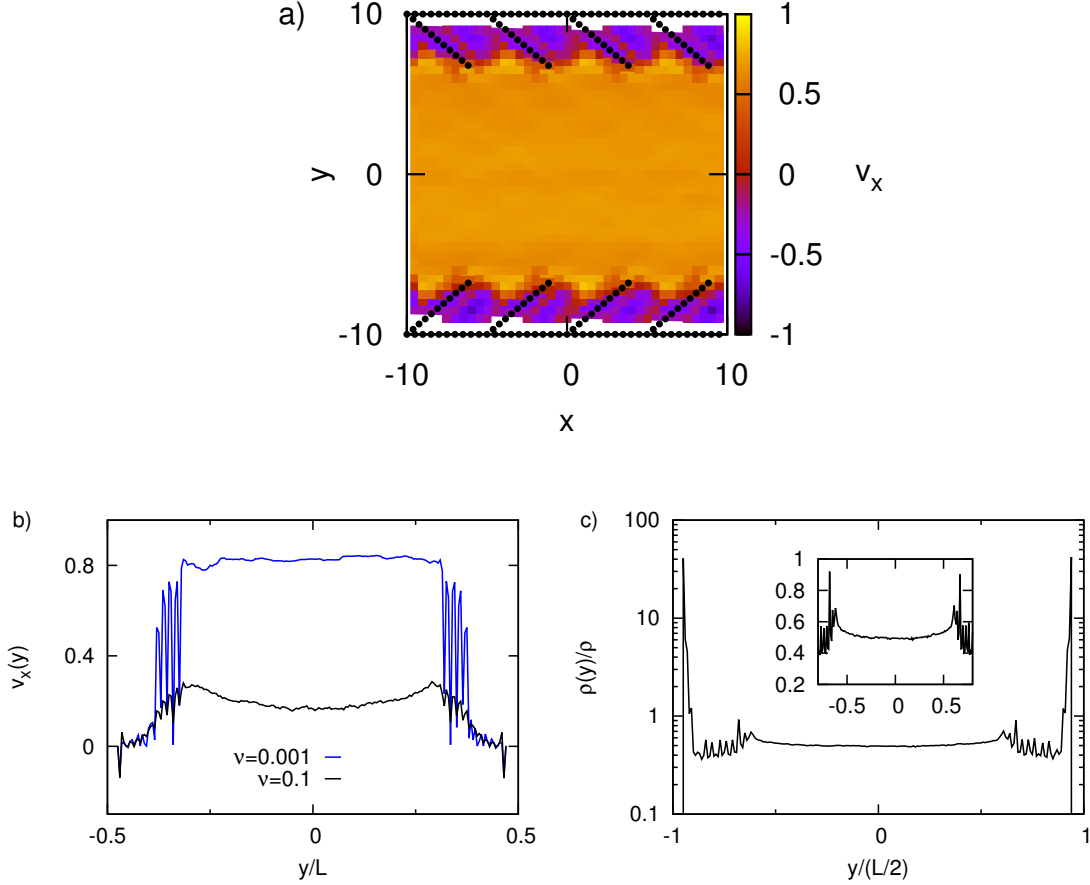


Figure 58: a)  $x$ -velocity as a function of position in space. Arm angle  $\theta = 40^\circ$ , tumbling frequency  $\nu = 0.001$ . b) Velocity profiles at  $\theta = 40^\circ$ . c) Density profile at  $\theta = 40^\circ$  and  $\nu = 0.1$ . Inset: zoom on same data.

This means that the bulk region is defined independently on the arm angle  $\theta$ . The velocity in the bulk has a qualitative similar behavior as the total average velocity, as can be seen comparing Figures 53-54 and 59a,b. Both averages have the same dependence as a function of arm angle  $\theta$  and as a function of tumbling frequency  $\nu$ . At low frequency, the velocity in the bulk is much higher than at higher frequency, since at higher frequencies particles do tumble more and the motion in the bulk will be more random, disordered and less oriented. Quantitatively, the values of the velocity in the bulk are higher than the values of the total average velocity, since particles at the walls are not considered, and most of those particles are not moving while being blocked in the acute angle and waiting for a tumbling event.

The density of particles in the bulk is zero for low angles  $\theta < \theta_c$ , where all particles get trapped in the acute angle. Increasing the angle, the number of particles in the bulk

strongly depends on the tumbling frequency, see Figures 59c,d. For a relatively high frequency  $\nu = 0.1$  ( $\lambda = 10$ ), it increases monotonously with the angle, similarly as the escape probability does. At low frequency ( $\nu = 0.001$ ) the number of particles in the bulk has a non-monotonous behavior, increasing until  $\theta \sim 40^\circ$  and decreasing afterwards. The first increase is due to the fact that even if lower angle means more horizontal trajectory and so higher average x-velocity, at  $\theta = 35^\circ$  the escape probability from the acute angle is still quite low and many particles remain trapped. The successive decrease reflects the change in motion type from type I to II. Both in Figure 59c and 59d we clearly notice that the density in the bulk increases with increasing tumbling frequency. This happens since increasing the tumbling frequency means having more tumble events that let particles leave walls more often and reach them less often. Particles behave more similarly to passive Brownian particles which do not aggregate near walls and are uniformly distributed.

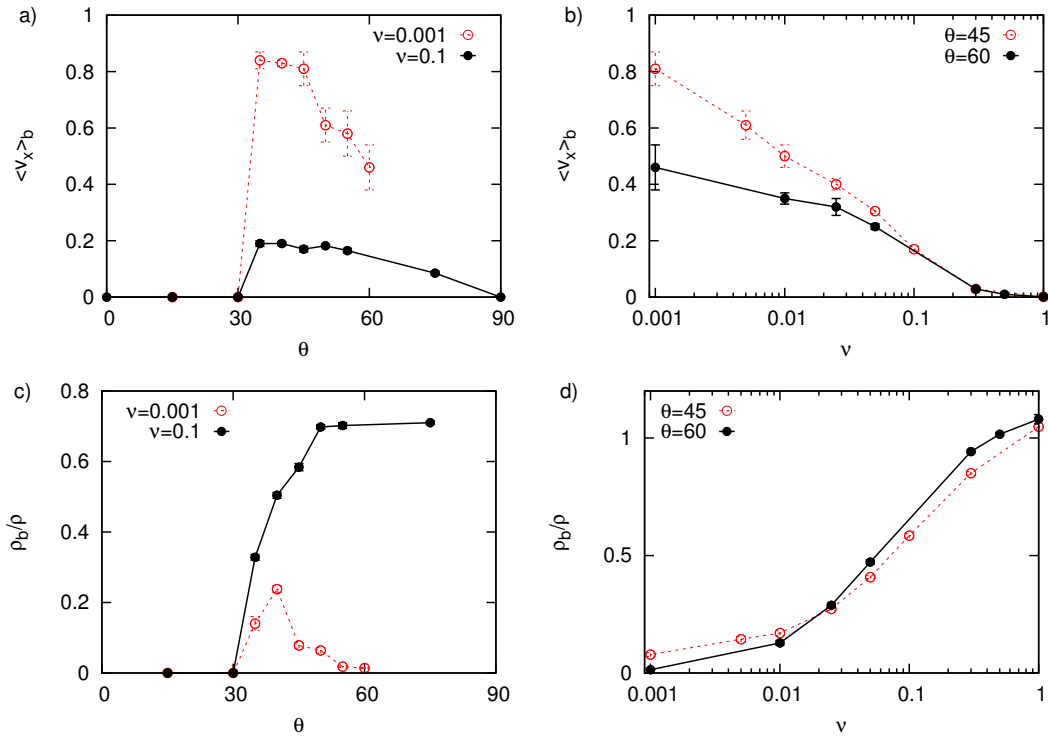


Figure 59: Average x-velocity in the bulk  $\langle v_x \rangle_b$  ( $-5 < y < 5$ ) as a function of arm angle (a) and tumbling frequency (b). Normalized density of particles in the bulk  $\rho_b/\rho$  as a function of arm angle (c) and tumbling frequency (d).



### 5.3.2 Wedge geometry

In order to study how differences in the design of the asymmetric ratchet-like channels affect the average velocity of particles, and in order to study also more realistic geometries which might be easier to build, we now consider a slight different channel geometry, which we call wedge geometry.

As described in the previous section, the arm-geometry is modified by adding a vertical wall connecting the end of the arm with the channel wall, as shown in the sketch in Figure 49B. Particles can then not get trapped in the acute angle. Instead we have a  $90^\circ$  angle from which the particles can easily escape. As shown in Figure 60, we now get a particle average velocity also at small angles  $\theta < 30^\circ$ . At  $\theta = 5^\circ$  we measure a very low average velocity, then it suddenly increases to the flux maximum which is now at  $\theta \sim 10^\circ$ . The value of the maximum is higher for low tumbling frequencies.

At angles  $\theta \leq 45^\circ$ , the average velocities are much higher if the wedge-geometry is used, while at larger angles the average velocity value of the arm-geometry can be slightly higher than the one with the wedge-geometry. This happens because of two competing effects. The first and apparently stronger effect is the escape probability from the acute angle, which for the arm-geometry increases with angle, favoring the wedge-geometry for which the angle to escape from is always  $90^\circ$ . The other effect is that after the random tumbling event, the direction in which the particle leaves the wall confinement is distributed between zero and  $\theta$  for the arm-geometry, or between zero and  $90^\circ$  for the wedge-geometry. A small  $\theta$  and so a smaller mean escape angle increases the flux, given the longer and more horizontal trajectories necessary to reach the opposite wall. At  $\theta \leq 45^\circ$  the first effect is leading and the wedge geometry shows higher fluxes, while at larger angles the second effect is leading and the arm-geometry shows higher fluxes, especially at higher tumbling frequencies where particles more frequently leave the acute angle.

The dependence on other system parameters like distance  $d$  and channel width  $L$  is expected to be the same as in the already discussed arm-geometry, since the behavior is based on the different types of trajectories of low-tumbling particles similar to that in the arm-geometry.

### 5.3.3 Dependence on particle aspect ratio

For comparison and completeness we now extend our study to spherical particles of aspect ratio  $\alpha = 1$ .

The particle elongation, namely the fact that  $\alpha > 1$  ensures in this model particle alignment with walls, like we observe and have largely described for particles with aspect ratio  $\alpha = 2$ . The alignment will take place for each aspect ratio larger than one, eventually just at slight different speeds, such that in the single particle limit we expect almost the

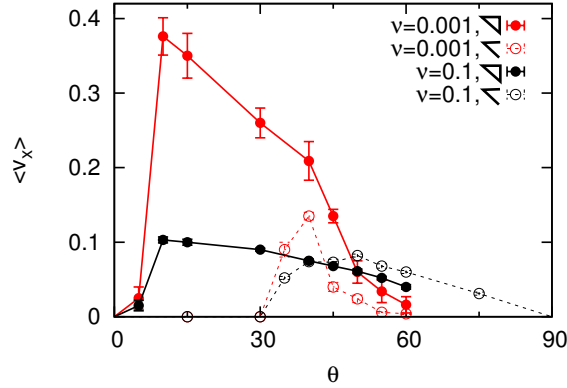


Figure 60: Average x-velocity as a function of arm angle  $\theta$  in the wedge geometry (solid lines) compared to the arm geometry values (dashed lines).

same qualitative behavior at any  $\alpha > 1$ .

On the other hand, we expect a strong qualitative difference in the motion of particles of aspect ratio  $\alpha = 1$ , namely for Janus particles. Spheres do not align with any boundary wall. They do also not get completely trapped in acute angles, since their rotational diffusion does not depend on anything else than the tumbling frequency and is therefore not affected from the interaction with the walls. In Figure 61 we show the average x-velocity of spheres in a channel with arm-geometry as a function of arm angle  $\theta$  for two different tumbling frequencies. We notice that there is no critical angle below which there is particle trapping. Instead we observe that the average velocity has its maximum for an arm angle  $\theta \sim 15^\circ$ .

Also the average velocity in the bulk and the density of particles in the bulk behave differently compared to elongated particles of aspect ratio  $\alpha > 1$ . As shown in Figure 63, the average velocity in the bulk increases with the arm angle and it is larger for low tumbling frequency. The density of particles in the bulk is almost independent on the arm angle and is much larger for high tumbling frequency than for low frequency, where the density of particles in the bulk is very low ( $\sim 0.01 = 1\%$ ). Both the independence of the angle as well as these very low values can be explained considering that spheres do not align with the walls. The particles remain oriented towards the walls and do not leave the arm parallel to it, but leave the arm in the direction of their orientation. The trajectory performed until a tumble event occurs is sketched in Figure 62. The velocity of the particle is maximal in the part of the trajectory away from the walls, where the velocity of the particle equals the self-propelling velocity. At the walls the actual velocity is the component of the self-propelling velocity parallel to the wall.

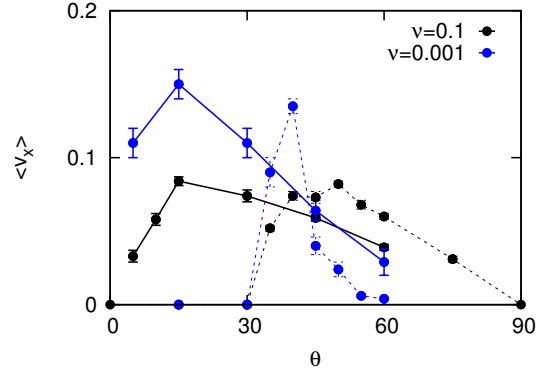


Figure 61: Average x-velocity as a function of arm angle  $\theta$  in the arm geometry for run and tumbling particles of aspect ratio  $\alpha = 1$  (solid lines) and  $\alpha = 2$  (dashed lines).

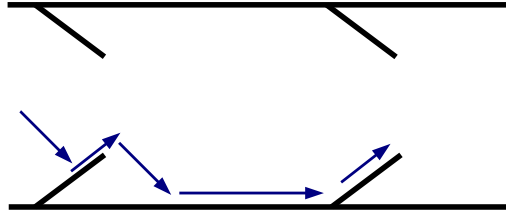


Figure 62: Sketch of the trajectory of a non-tumbling self-propelling sphere ( $\alpha = 1$ ) in the arm-geometry. The orientation of the particle is not affected by the wall.

## 5.4 Effects of particle density

In practice, most systems have low but finite densities, such that it is of great interest to study how particle density affects the ratchet effect. We therefore now consider systems with variable density, and study the effect of the excluded volume between particles. Density turns out to have a very strong effect on the ratchet effect. As can be seen from the simulation snapshots of Figure 64, particles exhibit accumulation and jamming at the walls. No complete trapping in the acute angle is possible any more, since the area between arm and wall is limited and not all particles can fit in. Moreover, trajectories in the bulk are further randomized because of collisions.

### Arm geometry

We start by studying density effects in the arm-geometry. Elongated run-and-tumbling particles of aspect ratio  $\alpha = 2$  are considered. In Figure 65, the particle average velocity along the channel as a function of particle density is shown for different arm angles and

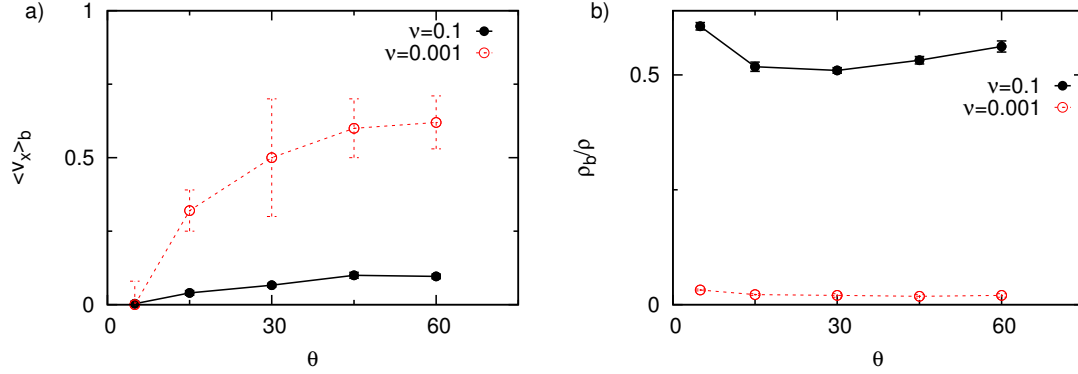


Figure 63: Average x-velocity in the bulk (a) and normalized average density of particles in the bulk (b) as a function of arm angle  $\theta$  in the arm geometry for run and tumbling particles of aspect ratio  $\alpha = 1$  (spheres).

tumbling frequencies. The average x-velocity rapidly decreases with increasing density. At density  $\rho = 1$ , the average x-velocity is already almost vanishing at any arm angle and tumbling frequency considered. The velocity decreases with increasing density since particles aggregate and jam near the walls and between the arms, as can be seen also in Figure 64. The particles which are closer to walls and arms get blocked by other particles pushing on them. Increasing further the particle density, the particles fill up all the space between the arms until the ratchet geometry is almost completely hidden by the particles, such that the other particles will not be affected by the channel asymmetry. Some reminiscent effect of the ratchet structure may be seen in the pattern how particles accumulate at the walls (see Figure 64A).

In Figure 65a the dependence on density is shown for arm angle  $\theta = 35^\circ$  and different tumbling frequencies. At all considered frequencies, the velocity decreases monotonically with density. We notice that average velocity values for low tumbling frequencies are always higher than the values for higher tumbling frequency, as it is also for single-particle simulations. In Figure 65b the dependence on density at tumbling frequency  $\nu = 0.1$  and different arm angles is shown. At low angles ( $\theta = 15^\circ$ ) the dependence on density is non-monotonic. A single particle would get trapped in the acute angle, the velocity is therefore zero at low density. The velocity increases up to density  $\rho \sim 0.25$ , and decreases afterwards. For all the other angles the velocity monotonically decreases with density.

#### Dependence on the arm distance $d$

In the previous section we have seen in the single-particle limit how the distance between arms is an important parameter to vary at high arm angles ( $\theta > 45^\circ$ ) and low tumbling frequency ( $\nu = 0.001$ , namely in narrow channels,  $\lambda/L = 1/\nu L \gg 1$ ).

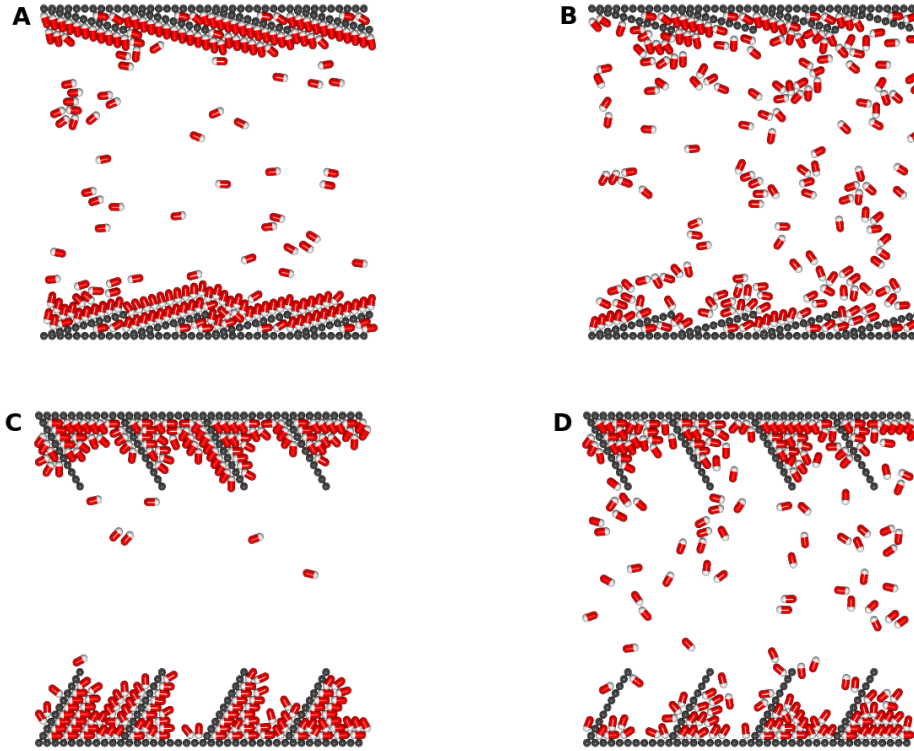


Figure 64: Simulation snapshots at density  $\rho = 0.5$  in the arm-geometry at different arm angles  $\theta$  and tumbling frequencies  $\nu$ : a)  $\theta = 15^\circ$  and  $\nu = 0.001$ . b)  $\theta = 15^\circ$  and  $\nu = 0.1$ . c)  $\theta = 60^\circ$  and  $\nu = 0.001$ . d)  $\theta = 60^\circ$  and  $\nu = 0.1$ .

In order to design optimal ratchet-like micro-channels, an interesting question to consider is whether the arm distance is an important parameter also in denser systems. In Figure 66 we see that for dense systems the arm distance  $d$  has not the same strong effect as it had on single-particle simulations. For dense systems, at arm angle  $\theta = 35^\circ$ , the velocity slightly decreases with arm angle, while at  $\theta = 60^\circ$  we notice a slight increase of the velocity, but the velocity values are really low and close to zero, almost all the particles are blocked close to the walls. The little increase of the velocity is probably due to the same mechanisms that we have discussed in the single-particle case, namely the change in motion type from type II to III. The observed decrease is in agreement with the expectation that the velocity tends to zero in the limit of infinite arm distance  $d \rightarrow \infty$ , since that case is equivalent to a channel without asymmetric ratchet-like walls.

#### Average velocity and density in the bulk

In Figure 67, we show the average x-velocity of particles in the bulk, as well as the normal-

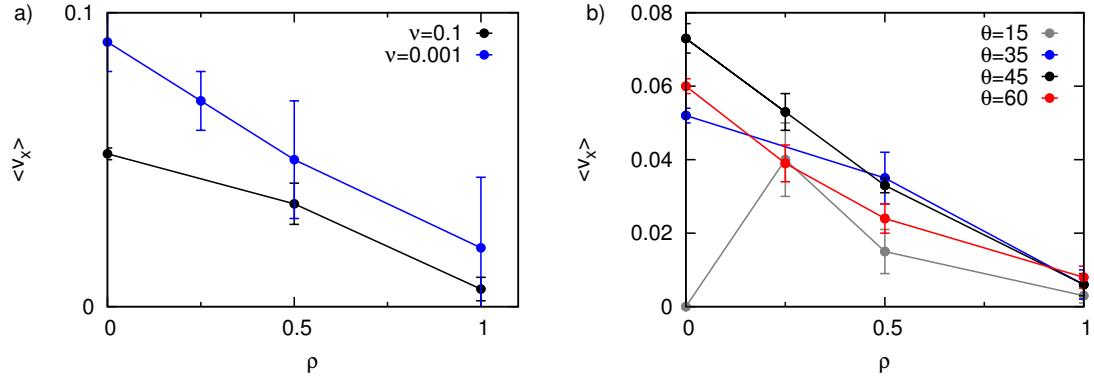


Figure 65: Particle average x-velocity as a function of particle density in the arm-geometry. a) Arm angle  $\theta = 35^\circ$  and different tumbling frequencies. b) Tumbling frequency  $\nu = 0.1$  and different angles (color code in the legend).

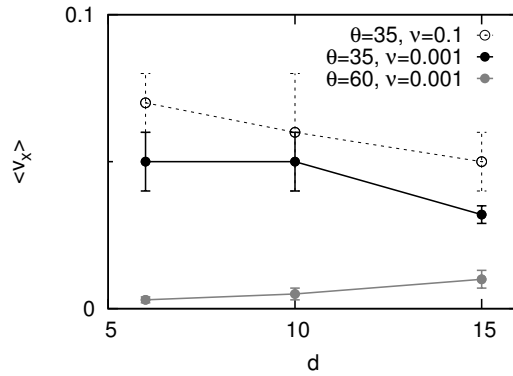


Figure 66: Average x-velocity as a function of arm distance  $d$  for systems at particle density  $\rho = 0.25$ .

ized density of particles in the bulk, where bulk is defined as the space region for which the distance from the channel center is less than  $b$  with  $b = (L - 2r)/2 = 5$ , as before. Both quantities behave very differently as in the single-particle case. The percentage of particles in the bulk decreases with arm angle  $\theta$ , since for high angles there is more space (more area) between the arms where particles can aggregate and get blocked, as it can be seen from the simulation snapshots shown in Figure 64. The x-velocity in the bulk increases with the arm angle  $\theta$ , since increasing the angle there are less particles in the bulk which means having less collisions and so less randomness and higher x-velocity. In Figure 67 we also notice that increasing the tumbling frequency  $\nu$  increases the number of particles in the bulk, since particles are less blocked at the walls, but their x-velocity in the bulk will be lower since with more particles there will be more collisions and so less oriented motion. The behavior of the total x-velocity (Figure 65) can be also understood from the described

behavior of the percentage of particles in the bulk and their x-velocity.

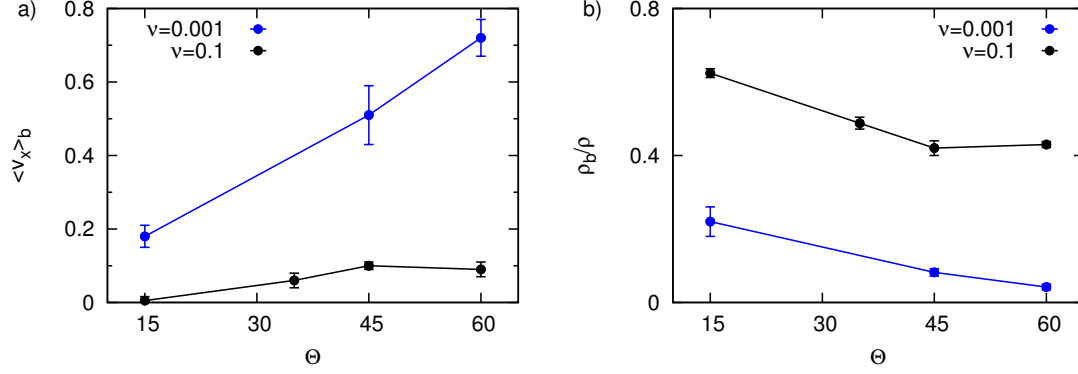


Figure 67: Average x-velocity in the bulk (a) and normalized average density of particles in the bulk (b) as a function of arm angle. Tumbling frequency  $\nu = 0.1$  (black) and  $\nu = 0.001$  (blue), particle density  $\rho = 0.5$ .

### Wedge geometry

We now consider the wedge-geometry presented in the previous sections. In the single-particle case the highest velocity value has been observed with the wedge-geometry at arm angle  $\theta = 10^\circ$  and low frequency  $\nu = 0.001$ . How this value is affected by the particle density is shown in Figure 68. In this dense case, the use of the wedge geometry instead of the arm-geometry does not have any strong effect on the average x-velocity of the particles. For almost all the angles and frequencies examined, we find for the wedge geometry lower or comparable average x-velocity values than those of the arm-geometry, as can be seen in Figure 69.

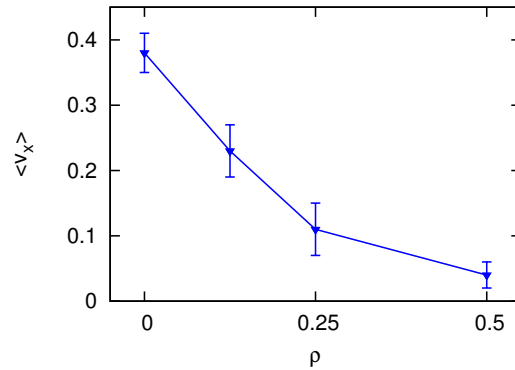


Figure 68: Particle average x-velocity as a function of particle density in the wedge-geometry at angle  $\theta = 10^\circ$  and tumbling frequency  $\nu = 0.001$ .

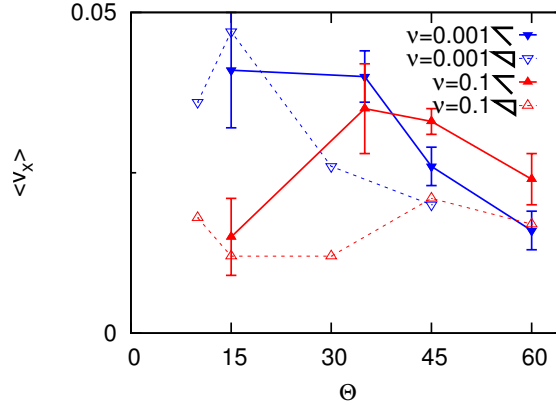


Figure 69: Particle average x-velocity as a function of arm angle. Tumbling frequency  $\nu = 0.1$  (red up-triangles) and  $\nu = 0.001$  (blue down-triangles). Particle density  $\rho = 0.5$ . Solid lines: arm geometry. Dashed lines: Wedge geometry.

### Arc geometry

We have seen that most of the particles aggregate near the walls especially at the angles between walls and arms. In order to increase the ratchet effect, i.e. the average x-velocity of particles, we modify the ratchet geometry, as shown in the sketch of the geometry in Figure 49c. In Figure 70 we show a comparison of the average x-velocity values as a function of particle density for these three geometries at angle  $\theta = 45^\circ$  and tumbling frequency  $\nu = 0.1$ . For all the geometries considered, the velocity decreases with density. The arc geometry clearly produces better particle average x-velocity than the other two geometries, although the values are still much smaller than the single particle values. Moreover we notice that at least at this angle, the velocity in the arm geometry is slightly higher than the velocity in the wedge geometry, which results to be the worst option out of the three considered at angle  $\theta = 45^\circ$ .

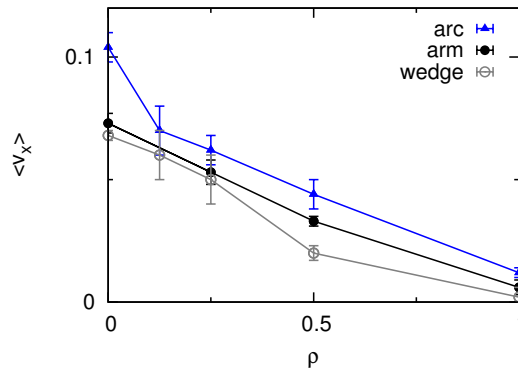


Figure 70: Average x-velocity as a function of particle density  $\rho$  for the three different geometries at angle  $\theta = 45^\circ$  and tumbling frequency  $\nu = 0.1$ .



## 5.5 Mixture of fast and slow particles

In nature, populations of particles frequently have a wide distribution of certain properties, like particle length or particle self-propelling velocity, such that it is very interesting to study how heterogeneous populations behave. Furthermore, this can help to develop microfluidic devices capable to automatically sort different kind of particles. We start studying heterogeneous populations of particles by considering the simple situation of a two-component system, namely a system with particles of two different types. We consider here the arm-geometry with particles that differ only in their self-propelling speed. A simulation snapshot is shown in Figure 71. We notice that the expulsion mechanism presented and discussed in Chapter 4 still leads to a clear separation of fast particles at the walls and slow particles in the bulk. On the other hand, the ratchet effect leads to a nonzero particle average velocity along the channel main axis. The interplay between expulsion mechanism and ratchet effect leads to particle separation also in direction of the channel main axis, similarly as what happens in a channel with imposed Poiseuille flow (see Chapter 4).

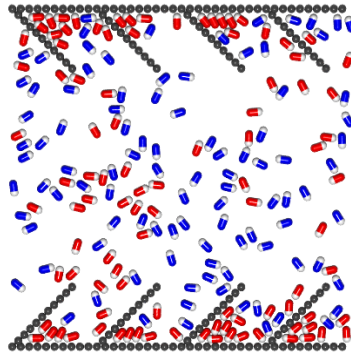


Figure 71: Simulation snapshot: Slow particles  $v_s = 0.2$  in blue and fast particles  $v_f = 0.8$  in red.

Our system is composed by  $N = 200$  run-and-tumbling particles of length to width aspect ratio  $\alpha = 2$  and standard tumbling frequency  $\nu = 0.1$ . The considered ratchet geometry is the arm-geometry (arm angle  $\theta = 45^\circ$ , arm distance  $d = 5$ , channel width  $L = 20$ ). We have  $N/2$  fast particles with velocity  $v_f$  and  $N/2$  slow particles with velocity  $v_s$  such that the average velocity is  $\bar{v} = (v_f + v_s)/2$  and the total particle density is  $\rho = 0.5$ .

### Dependence on velocity difference $\Delta v$ and comparison with single-component systems

The average x-velocity of fast and slow particles is shown in Figure 72 in comparison with single-component data. Interestingly, for almost all the self-propelling velocities that we

analyzed, the average x-velocity of both slow and fast particles is actually higher than it would be if we consider them alone in a single-component system. Note that in Figure 72 pairs of red bullets refer to simulations with average velocity  $\bar{v} = 1$ , such that for example the red bullet at  $v = 1.5$  refers to the average x-velocity of fast particles ( $v_f = 1.5$ ) in a mixture with slow particles with velocity  $v_s = 0.5$ . A first consequence of this observation is that it would be more efficient (in the sense that the rectification effect of the ratchet is stronger) to have a mixture of  $N/2$  fast particles and  $N/2$  slow particles instead of having  $N$  particles with velocity  $\bar{v} = (v_f + v_s)/2$ .

The  $N/2$  fast particles aggregate and jam less than the  $N$  fast particles of a system with only fast particles. They are therefore less blocked at the channel walls, such that the average x-velocity of fast particles increases. On the other hand, the  $N/2$  slow particles are also less blocked at the walls compared to a one-component system of  $N$  slow particles. Moreover, slow particles are now almost segregated to the channel center but can still feel the ratchet asymmetry such that their motion will be directed and not symmetric and random. The x-velocity increases therefore also for slow particles. The x-velocity increase of slow particles is also due to collisions with the fast particles.

Comparing the average x-velocity of the  $N/2$  fast or slow particles in the mixture with the simulation data of  $N/2$  fast or slow particles in one-component systems ( $\rho = 0.25$  black open circles in Figure 72), we notice that the one-component data are still quite larger than the mixture data. This reflects the important effect that particle density has. Increasing the total number of particles in the system leads to a decrease of the average velocity.

In order to support the optimization of the design of microfluidic sorting devices, it is important to know which is the optimal arm angle that maximizes the separation of slow and fast self-propelling particles in ratchets. We therefore compute the average velocity of slow and fast particles in channels with asymmetric ratchet-like walls (arm-geometry) at different arm angles. As shown in Figure 73, the separation of fast and slow particles is approximately proportional to the ratchet effect of single-component systems. The optimal angle for which the difference of velocity between fast and slow particles is maximal, is approximately  $35^\circ$ , angle for which we get also the strongest ratchet effect of single-component systems.

### **Comparison with channel with Poiseuille flow**

We have seen that fast and slow self-propelling particles can be separated from each other in different ways. We studied the separation of fast and slow self-propelling particles in micro-channels with and without Poiseuille flow (Chapter 4), and we also studied the separation of particles in micro-channels with asymmetric ratchet-like walls. An interesting question to answer is in which of these situations the separation of fast and slow self-propelling

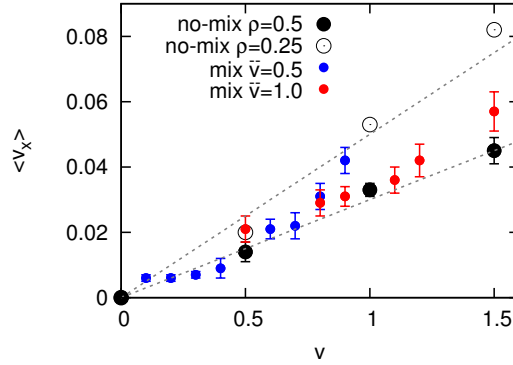


Figure 72: Average x-velocity of fast and slow particles in an equimolar two-component mixture with particle density  $\rho = 0.5$ , tumbling frequency  $\nu = 0.1$  and arm angle  $\theta = 45^\circ$ . Red bullets refer to simulations with average velocity  $\bar{v} = 1$ , blue bullets to simulations with average velocity  $\bar{v} = 0.5$ . Black bullets are single-component simulations data with  $\rho = 0.5$  and black circles single-component simulations data with density  $\rho = 0.25$ . Lines are guides to the eye.

particles is better achieved.

In order to quantify and measure the separation quality, we have defined the separation parameter (see Eq.(56) in Chapter 4)

$$\psi = \psi^f = \frac{\int_0^d \rho^f(x) dx}{\sum_{\alpha} \int_0^d \rho^{\alpha}(x) dx}. \quad (61)$$

Comparing the value of a channel without flow and without asymmetric ratchet-like walls ( $\psi = 0.78 \pm 0.01$ ) with the value of a channel without flow but with asymmetric ratchet-like walls ( $\psi = 0.81 \pm 0.02$ ), we can conclude that at least for this set of parameters ( $\rho = 0.5$ ,  $v_s = 0.5$ ,  $v_f = 1.5$ ,  $L = 20$ ) the two geometries perform in the same way. In a channel with Poiseuille flow, the expulsion mechanism works such that the separation at the channel walls can still be measured and the value ( $\psi = 0.79 \pm 0.01$ ) is comparable with the channel without flow.

On the other hand, in channels with asymmetric ratchet-like walls as well as in channels with Poiseuille flow, separation happens not only in the direction perpendicular to the walls, which has been quantified with the separation parameter  $\psi$ . Separation happens also parallel to the walls, and has been quantified measuring the average particle velocity or the particle flux (see equation 57 in Chapter 4). In the case of channel with Poiseuille flow these values are much higher ( $\langle v_s \rangle = 0.59 \pm 0.01$ ,  $\langle v_f \rangle = 0.29 \pm 0.01$ ,  $\Delta v = 0.30 \pm 0.01$ ) than for the channel with ratchet-like walls ( $\langle v_s \rangle = 0.021 \pm 0.001$ ,  $\langle v_f \rangle = 0.057 \pm 0.001$ ,  $\Delta v = 0.036 \pm 0.001$ ), although these values clearly depend on the imposed capillary velocity,

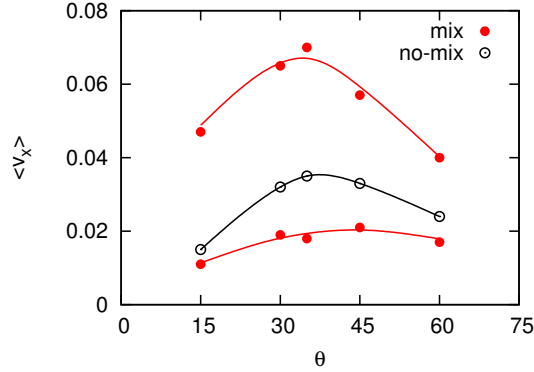


Figure 73: Average x-velocity of fast and slow particles in two-component systems as a function of the arm angle  $\theta$  (red bullets), total particle density  $\rho = 0.5$ , tumbling frequency  $\nu = 0.1$ ,  $v_s = 0.5$ ,  $v_f = 1.5$ . Black circles are single component simulations data with  $\rho = 0.5$ ,  $\nu = 0.1$  and  $v = 1$ .

which is not necessary in the ratchet geometry.

We can therefore conclude that in order to separate self-propelling particles with different motilities, channels with Poiseuille flow are better than micro-channels with ratchet-like walls. A better design of the ratchet-geometry could eventually lead to better performance of such devices, but so far as we have studied the channel with flow has better separation results. If a separation along the channel section is desired (separation perpendicular to the channel walls) all the considered setups perform similarly, such that a simple channel can be successfully utilized.

## 5.6 Summary

In this Chapter, we have studied the motion of active particles in micro-channels with asymmetric ratchet-like walls. Rectifying the random motion of passive Brownian particles has been fascinating scientists for a long time. More recently, physicists started to study also active particles, and the possibility of rectifying their random motion. It is therefore very interesting to give a contribution in the study of ratchet devices for active particles.

We studied first the motion in the dilute limit of single particles, in order to better understand the fundamental physics that governs the behavior of dense systems. At higher densities, we considered both single-component systems, where all the particles do not differ from each other, and also two-components systems, where we study the motion of particles which differ in their self-propelling speed. We consider three different ratchet-like geometries, which we call arm-geometry, wedge-geometry and arc-geometry, and study the ratchet phenomenology as a function of system parameters like arm-angle, arm distance and particle mean-free-path to channel-width ratio.

We study the ratchet effect measuring several quantities. The most relevant is the average velocity along the channel axis, which is indeed a measure of the ratchet effect. For single-particle simulations, the maximal velocity is obtained in the wedge-geometry at low angles ( $\theta \sim 10^\circ$ ) for elongated particles of aspect ratio  $\alpha = 2$  and low tumbling frequency  $\nu = 0.001$ . In the arm-geometry, at such low angles, particles get trapped in the acute angle between arm and channel wall. Due to their elongation particles can not escape from it. Spherical particles do not get trapped, but their velocity values are not the highest observed. With increasing particle density, the velocity strongly decreases in all the considered cases. Only in the arm-geometry at low angles, when particles get trapped, the behavior on density is non-monotonic, resulting in a relative maximal velocity at density  $\rho = 0.25$ . At density  $\rho = 0.5$  the best resulting geometry still is the wedge-geometry at low angles ( $\theta \sim 15^\circ$ ), although now the difference with other geometries and other angles is smaller. For two-component systems, the separation of fast and slow particles is approximately proportional to the ratchet effect of single-component systems. Although the channel with ratchet-like walls does not need any imposed flow to separate fast and slow particles along the channel main axis, it turns out to be less effective in separating fast and slow particles compared to a channel with Poiseuille flow.

Our results provide new insights in the off-equilibrium physics, in particular in the physics of self-propelled particles in static ratchets. The presented findings could be of particular interest in the development and design of new microfluidic lab on chip ratchet-devices in order to improve transport of active matter as well as sorting techniques for multicomponent systems.



---

## 6 Conclusions

We have studied the properties of the motion of self-propelled particles by means of numerical simulations. We have mainly focused our attention to the dynamics of Run-and-Tumbling particles. The Run-and-Tumble model is inspired by the motion of bacteria like *E. coli*, which is characterized by straight motions, called runs, and random tumbling events, where the bacterium changes orientation.

Diffusion coefficients are fundamental quantities in order to characterize systems with large number of particles. Therefore we studied the motion of Run-and-Tumbling particles in bulk, where we analyzed rotational and translational diffusion coefficients. The dependence of these coefficients on particle density, particle aspect ratio and self-propelling velocity has been investigated, giving rise to interesting results like the increase of the rotational diffusion with increasing density in a certain region of the aspect ratio - velocity parameter space. This never happens with passive Brownian rods, for which collisions with other particles always hinders rotation. At low aspect ratio, particles are still not long enough to form clusters, and collisions among self-propelled particles lead to an enhancement of their rotation. We explained this result with an active-gas theory. This approximation considers binary and localized collisions among particles. This is indeed the case for particles of low aspect ratio, for which collisions do not induce alignment but do only enhance their rotation. Increasing aspect ratio, particles tend to align more and eventually form clusters. The active-gas-picture does not hold any more and the rotational diffusion coefficient decreases with increasing density.

The translational diffusion coefficient behaves, as a consequence of the rotational diffusion behavior, in good agreement with the relation  $D \sim v^2/D_r$ . This agreement is better at low aspect ratio and low particle density, where the active-gas approximation is valid. For low aspect ratio, the translational diffusion decreases with particle density. At high aspect ratio, we expect it to increase with density, but since particles tend to form clusters which rotate very slowly, we could not reach the diffusive regime and therefore we could not

measure the diffusion coefficient. As a function of self-propelling velocity, the translational diffusion of single-particle simulations increases quadratically. On the other hand, for non-vanishing concentrations, the translational diffusion of elongated particles increases with self-propelling velocity, but not quadratically. This happens since the rotational diffusion coefficient does also increase with self-propelling velocity. In order to better understand and describe the presented phenomenology of particle dynamics in bulk, investigating also the range of validity of the active-gas approximation, we performed a detailed two-particles scattering analysis, studying how collision angle and collision position of two elongated particles affects their alignment and rotation. We furthermore studied how particle aspect ratio and particle density affects cluster formation, using Voronoi tessellation and order parameters. Concerning the dynamics of self-propelled particles in bulk, future investigations could be done studying the diffusion coefficients of elongated rods as a function of particle density, corroborating the result that translational diffusion can increase with density at high aspect ratios ( $\alpha \geq 4$ ). Moreover, in order to corroborate these findings, and in order to have a more experiment-related simulation, the rotational diffusion increase with increasing density could be tested also with slightly different models, as, for example, models where the diffusion coefficients of single particles depend on their aspect ratio.

Populations of particles are in nature usually heterogeneous in all their characteristics, like size, shape, composition or in self-propelling velocity. For example, sperm cells of mammals are not all equally fast and only the fastest ones can reach the ovum and fertilize it. It is therefore of great interest to develop sorting techniques. Here we have investigated two-component systems of particles with different motility, studying their motion in micro-channel confinement, employing channels with and without fluid Poiseuille flow. The presence of a wall induces the separation of fast and slow particles, slow ones are expelled by the fast ones from the wall into the bulk, resulting in a segregated state. This phenomenon has been analyzed as a function of various system parameters like particle density, particle velocities, and channel width. Separation always grows with the velocity difference, but the dependence on other parameters is less obvious. It turns out that low average velocity, intermediate density, and large channels optimize separation of particles with different motility. We have also investigated how the presence of a capillary Poiseuille flow in the microchannels affects segregation. In this case, tuning the fluid velocity, fast particles swim upstream, while slow particles swim downstream, leading to particle sorting in flow direction. In the presence of flow, separation grows with fluid velocity, channel width, and density, while there is almost no dependence on the average particle velocity. We proposed a setup in which the channel is confined between membranes. The membrane is supposed to be penetrable by the fluid but not by the particles. The separation is shown to be the maximal for fluid velocities slightly higher than the slow-particle velocity.



---

Rectifying the random chaotic motion of both passive particles has been fascinating scientists for a long time. More recently, also active particles and the possibility of rectifying their random motion attracted several research work. Here we studied the rectification of the random motion of Run-and-Tumbling particles in channels with asymmetric ratchet-like walls. We quantified this phenomenon measuring quantities like the average particle velocity as a function of several system parameters. We used three types of ratchet geometries, which we called arm-geometry, wedge-geometry and arc-geometry. The arm-geometry is made by small diagonal walls, called arms, added to the main walls of the channel. The diagonal arms break the symmetry and induce the directed particle motion. The wedge-geometry differs from the arm-geometry by an additional wall which prevents particle trapping. Indeed, in the arm-geometry at low arm angles, particles get trapped in the acute angle between arm and channel wall. Due to their elongation particles can not escape from it. Spherical particles do not get trapped but neither align with walls, resulting in low velocity values. The arc geometry, consisting of round parts instead of acute angles, is designed to avoid particle trapping and jamming. We studied first the motion in the dilute limit of single particles, in order to better understand the fundamental physics that governs the behavior of denser systems. For single-particle simulations, the maximal ratchet effect is obtained with the wedge-geometry at low angles ( $\theta \sim 10^\circ$ ) for elongated (non-spherical) particles and low tumbling frequency (high mean free path to channel width ratio).

With increasing particle density, the velocity strongly decreases in almost all the considered cases. Only in the arm-geometry at low angles, when particles get trapped, the behavior on density is non-monotonous, resulting in a maximal velocity at semi-dilute densities. For non-vanishing concentrations the best geometry results still to be the wedge-geometry at low angles, although now the difference with other geometries and other angles is smaller. We considered not only single-component systems but also two-components systems of particles with different motility. Particle separation along the channel main axis is here obtained only with the asymmetric ratchet-like structure. Although here no imposed solvent flow is needed to sort particles, the separation results to be less effective than the separation which can be obtained in microchannels with Poiseuille flow.

The study of the separation of particles with different self-propelling velocities could be extended to particles which differ in other properties like geometry or tumbling frequency. Furthermore it could be interesting to check the precise influence of hydrodynamic interactions on dynamical quantities like rotational and translational diffusion, and on separation of particles in channels.

Even though we mainly focused our attention to Run-and-Tumbling particles, the presented results turn out to be independent on the model details. We checked the validity of

sample results also with other self-propelled particle models like Active-Brownian-Particles. Our results give new insights into the fascinating world of self-propelled particles. The presented findings are of particular relevance for transport, sorting and separation techniques. We imagine applications of these results in the development of microfluidic lab-on-chip devices, capable to manipulate several particles ensembles in a simple environment without using laser traps or other invasive external fields.

---

## Acknowledgments

Here first of all I would like to acknowledge Prof. Dr. Gerhard Gompper and Dr. Marisol Ripoll for giving me the opportunity to work in the *Institute of Complex Systems, Theoretical Soft Matter and Biophysics* at the *Forschungszentrum Jülich*, where I could write this PhD thesis. I thank them both especially also for their support and help which they always nicely gave me, without which this PhD thesis would probably not have been completed.

Furthermore I would like to acknowledge the International Helmholtz Research School for Biology and Soft Matter (IHRS BioSoft) for the opportunity to follow seminars, lectures and transferable-skills courses which have been offered from the School itself. Being a member of it also encouraged and helped the communication and networking among me and students of different disciplines.

I would also like to thank the colleagues of the Institute, especially Dr. Adam Wysocki, for very useful discussions and help. Finally I would like to thank Dr. Luca Angelani and Dr. Roberto Di Leonardo for having introduced me in the world of Physics of Self-Propelled Particles.

## References

- [1] T. Vicsek and A. Zafeiris, Phys. Rep. **517**(3-4), 71 (2012).
- [2] A. Dussutour, V. Fourcassié, D. Helbing, and J.-L. Deneubourg, Nature **428**(6978), 70 (2004).
- [3] Y. Katz, K. Tunstr, C. C. Ioannou, C. Huepe, and I. D. Couzin, Proc. Natl. Acad. Sci. U.S.A. **108**(46), 18720 (2011).
- [4] M. Ballerini, N. Cabibbo, R. Candelier, A. Cavagna, E. Cisbani, I. Giardina, V. Lecomte, A. Orlandi, G. Parisi, A. Procaccini, M. Viale, and V. Zdravkovic, Proc. Natl. Acad. Sci. U.S.A. **105**(4), 1232 (2008).
- [5] A. Schadschneider, W. Klingsch, H. Klüpfel, T. Kretz, C. Rogsch, and A. Seyfried, in *Encyclopedia of complexity and systems science* (Springer, 2009), pp. 3142–3176.
- [6] D. Helbing, I. Farkas, and T. Vicsek, Nature **407**(6803), 487 (2000).
- [7] H.-P. Zhang, A. Be'er, E.-L. Florin, and H. L. Swinney, Proc. Natl. Acad. Sci. U.S.A. **107**(31), 13626 (2010).
- [8] A. Walther and A. H. Müller, Soft Matter **4**(4), 663 (2008).
- [9] M. Yang and M. Ripoll, Phys. Rev. E **84**, 061401 (2011).
- [10] D. Chowdhury, L. Santen, and A. Schadschneider, Physics Reports **329**(4), 199 (2000).
- [11] D. Helbing, Rev. Mod. Phys. **73**(4), 1067 (2001).
- [12] A. Kudrolli, Rep. Prog. Phys. **67**(3), 209 (2004).
- [13] J. Elgeti, R. G. Winkler, and G. Gompper, Rep. Prog. Phys. (to appear).
- [14] K. Drescher, J. Dunkel, L. H. Cisneros, S. Ganguly, and R. E. Goldstein, Proc. Natl. Acad. Sci. U.S.A. **108**(27), 10940 (2011).
- [15] E. Lauga and T. R. Powers, Rep. Prog. Phys. **72**(9), 096601 (2009).
- [16] B. Rodenborn, C.-H. Chen, H. L. Swinney, B. Liu, and H. Zhang, Proc. Natl. Acad. Sci. U.S.A. **110**(5), E338 (2013).
- [17] H. C. Berg, *E. coli in Motion* (Springer, 2004).

- 
- [18] F. Neidhart *et al.*, *Escherichia coli and Salmonella.*, no. Ed. 2 (Blackwell Science Ltd, 1996).
- [19] M. Cates, Reports on Progress in Physics **75**(4), 042601 (2012).
- [20] J. Klafter and I. M. Sokolov, *First steps in random walks: from tools to applications* (OUP Oxford, 2011).
- [21] E. Frey and K. Kroy, Ann. Phys. **14**(1-3), 20 (2005).
- [22] A. Einstein, Ann. Phys. **17**(549-560), 16 (1905).
- [23] R. Brown, Edinburgh New Philosophical Journal **5**, 358 (1828).
- [24] G. M. Viswanathan, M. G. da Luz, E. P. Raposo, and H. E. Stanley, *The physics of foraging*, vol. 1 (Cambridge University Press, 2011).
- [25] K. Martens, L. Angelani, R. Di Leonardo, and L. Bocquet, The European Physical Journal E **35**(9), 1 (2012).
- [26] L. Angelani, EPL **102**(2), 20004 (2013).
- [27] L. Landau and E. Lifshitz, *Fluid Mechanics: Volume 6 (Course Of Theoretical Physics)* (Butterworth-Heinemann, 1987).
- [28] [www.physics.nyu.edu/pine/hydrodynamic\\_reversibility.html](http://www.physics.nyu.edu/pine/hydrodynamic_reversibility.html) .
- [29] S. Kim and S. J. Karrila, *Microhydrodynamics: principles and selected applications* (Dover Publications, 1991).
- [30] G. Batchelor, *An introduction to fluid mechanics* (Cambridge University Press, 1970).
- [31] R. Golestanian and A. Ajdari, Phys. Rev. E **77**(3), 036308 (2008).
- [32] E. M. Purcell, in *AIP Conference Proceedings* (1976), vol. 28, p. 49.
- [33] H. H. Wensink, J. Dunkel, S. Heidenreich, K. Drescher, R. E. Goldstein, H. Löwen, and J. M. Yeomans, Proc. Natl. Acad. Sci. U.S.A. **109**(36), 14308 (2012).
- [34] F. Peruani, J. Starruß, V. Jakovljevic, L. SØgaard-Andersen, A. Deutsch, and M. Bär, Phys. Rev. Lett. **108**(9), 098102 (2012).
- [35] I. Theurkauff, C. Cottin-Bizonne, J. Palacci, C. Ybert, and L. Bocquet, Phys. Rev. Lett. **108**(26), 268303 (2012).

## REFERENCES

---

- [36] I. Buttinoni, J. Bialké, F. Kümmel, H. Löwen, C. Bechinger, and T. Speck, *Phys. Rev. Lett.* **110**(23), 238301 (2013).
- [37] J. Tailleur and M. Cates, *EPL* **86**(6), 60002 (2009).
- [38] Y. Yang, V. Marceau, and G. Gompper, *Phys. Rev. E* **82**(3), 031904 (2010).
- [39] C. A. Yates, R. E. Baker, R. Erban, and P. K. Maini, *Canadian Applied Mathematics Quarterly* (2011).
- [40] T. Vicsek, A. Czirók, E. Ben-Jacob, I. Cohen, and O. Shochet, *Phys. Rev. Lett.* **75**(6), 1226 (1995).
- [41] A. Czirók, A.-L. Barabási, and T. Vicsek, *Phys. Rev. Lett.* **82**, 209 (1999).
- [42] G. S. Redner, M. F. Hagan, and A. Baskaran, *Phys. Rev. Lett.* **110**(5), 055701 (2013).
- [43] F. Peruani, A. Deutsch, and M. Bär, *Phys. Rev. E* **74**(3), 030904 (2006).
- [44] Y. Fily and M. C. Marchetti, *Phys. Rev. Lett.* **108**(23), 235702 (2012).
- [45] Y. Fily, S. Henkes, and M. C. Marchetti, *Soft Matter* **10**(13), 2132 (2014).
- [46] A. Wysocki, R. G. Winkler, and G. Gompper, *EPL* **105**(4), 48004 (2014).
- [47] M. Abkenar, K. Marx, T. Auth, and G. Gompper, *Phys. Rev. E* **88**(6), 062314 (2013).
- [48] C. W. Harvey, M. Alber, L. S. Tsimring, and I. S. Aranson, *New Journal of Physics* **15**(3), 035029 (2013).
- [49] J. Stenhammar, A. Tiribocchi, R. J. Allen, D. Marenduzzo, and M. E. Cates, *Phys. Rev. Lett.* **111**(14), 145702 (2013).
- [50] D. Strömbom, *Journal of theoretical biology* **283**(1), 145 (2011).
- [51] I. D. Couzin, J. Krause, R. James, G. D. Ruxton, and N. R. Franks, *Journal of theoretical biology* **218**(1), 1 (2002).
- [52] F. Peruani, T. Klauss, A. Deutsch, and A. Voss-Boehme, *Phys. Rev. Lett.* **106**(12), 128101 (2011).
- [53] I. D. Couzin, J. Krause, N. R. Franks, and S. A. Levin, *Nature* **433**(7025), 513 (2005).
- [54] L. Angelani, *Phys. Rev. Lett.* **109**(11), 118104 (2012).

- 
- [55] A. J. Wood and G. J. Ackland, Proceedings of the Royal Society B: Biological Sciences **274**(1618), 1637 (2007).
- [56] L. Angelani, R. Di Leonardo, and G. Ruocco, Phys. Rev. Lett. **102**(4), 048104 (2009).
- [57] A. Costanzo, R. Di Leonardo, G. Ruocco, and L. Angelani, Journal of Physics: Condensed Matter **24**(6), 065101 (2012).
- [58] R. Di Leonardo, L. Angelani, D. Dell' Arciprete, G. Ruocco, V. Iebba, S. Schippa, M. Conte, F. Mecarini, F. De Angelis, and E. Di Fabrizio, Proc. Natl. Acad. Sci. U.S.A. **107**(21), 9541 (2010).
- [59] P. Romanczuk, M. Bär, W. Ebeling, B. Lindner, and L. Schimansky-Geier, The European Physical Journal Special Topics **202**(1), 1 (2012).
- [60] M. Cates and J. Tailleur, EPL **101**(2), 20010 (2013).
- [61] J. Elgeti and G. Gompper, EPL **85**(3), 38002 (2009).
- [62] J. Elgeti and G. Gompper, EPL **101**(4), 48003 (2013).
- [63] S. F. Edwards and M. Doi, Clarendon, Oxford (1986).
- [64] Y. Han, A. Alsayed, M. Nobili, J. Zhang, T. C. Lubensky, and A. G. Yodh, Science **314**(5799), 626 (2006).
- [65] Y. Han, A. Alsayed, M. Nobili, and A. G. Yodh, Phys. Rev. E **80**(1), 011403 (2009).
- [66] J. Maguire, J.-P. McTague, and F. Rondelez, Phys. Rev. Lett. **45**(23), 1891 (1980).
- [67] D. Frenkel and R. Eppenga, Phys. Rev. Lett. **49**, 1089 (1982).
- [68] D. Frenkel and R. Eppenga, Physical Review A **31**(3), 1776 (1985).
- [69] F. Höfling, T. Munk, E. Frey, and T. Franosch, Phys. Rev. E **77**(6), 060904 (2008).
- [70] F. Höfling, E. Frey, and T. Franosch, Phys. Rev. Lett. **101**(12), 120605 (2008).
- [71] M. E. Foulaadvand and M. Yarifard, The European Physical Journal E: Soft Matter and Biological Physics **34**(4), 1 (2011).
- [72] M. E. Foulaadvand and M. Yarifard, Phys. Rev. E **88**, 052504 (2013).
- [73] L. Onsager, Physical Review **65**(3-4), 117 (1944).
- [74] M. Doi and S. Edwards, Journal of the Chemical Society, Faraday Transactions 2: Molecular and Chemical Physics **74**, 560 (1978).

- [75] J.-P. Hansen and I. R. McDonald, *Theory of simple liquids* (Elsevier, 1990).
- [76] D. Frenkel and J. Maguire, *Molecular Physics* **49**(3), 503 (1983).
- [77] A. Baskaran and M. C. Marchetti, *Phys. Rev. Lett.* **101**(26), 268101 (2008).
- [78] P. M. Reis, R. A. Ingale, and M. D. Shattuck, *Phys. Rev. Lett.* **98**(18), 188301 (2007).
- [79] A. Kudrolli, *Phys. Rev. Lett.* **104**(8), 088001 (2010).
- [80] V. Yadav and A. Kudrolli, *The European Physical Journal E: Soft Matter and Biological Physics* **35**(10), 1 (2012).
- [81] J. R. Howse, R. A. L. Jones, A. J. Ryan, T. Gough, R. Vafabakhsh, and R. Golestanian, *Phys. Rev. Lett.* **99**, 048102 (2007).
- [82] R. Golestanian, T. Liverpool, and A. Ajdari, *New Journal of Physics* **9**(5), 126 (2007).
- [83] R. Golestanian, *Phys. Rev. Lett.* **102**(18), 188305 (2009).
- [84] G. Voronoi, *Journal für die reine und angewandte Mathematik* **134**, 198 (1908).
- [85] P. Kraikivski, R. Lipowsky, and J. Kierfeld, *Phys. Rev. Lett.* **96**, 258103 (2006).
- [86] J. C. Maxwell, *Theory of heat* (DoverPublications.com, 2001).
- [87] R. P. Feynman, R. B. Leighton, M. Sands, and E. Hafner, *Am. J. Phys.* **33**, 750 (1965).
- [88] G. Vroege and H. Lekkerkerker, *The Journal of Physical Chemistry* **97**(14), 3601 (1993).
- [89] D. Reguera, A. Luque, P. Burada, G. Schmid, J. Rubi, and P. Hänggi, *Phys. Rev. Lett.* **108**(2), 020604 (2012).
- [90] D. C. Hong, P. V. Quinn, and S. Luding, *Phys. Rev. Lett.* **86**(15), 3423 (2001).
- [91] J. P. Brody and P. Yager, *Sensors and Actuators A: Physical* **58**(1), 13 (1997).
- [92] K. Loutherbach, J. Puchalla, R. H. Austin, and J. C. Sturm, *Phys. Rev. Lett.* **102**(4), 045301 (2009).
- [93] T. Duke and R. Austin, *Phys. Rev. Lett.* **80**(7), 1552 (1998).
- [94] K. Müller, D. A. Fedosov, and G. Gompper, *Scientific reports* **4** (2014).
- [95] R. M. Schultz and C. J. Williams, *Science* **296**(5576), 2188 (2002).



- 
- [96] A. Bollendorf, J. Check, D. Katsoff, and D. Lurie, *Systems Biology in Reproductive Medicine* **32**(2), 157 (1994).
- [97] B. Shao, L. Z. Shi, J. M. Nascimento, E. L. Botvinick, M. Ozkan, M. W. Berns, and S. C. Esener, *Biomedical microdevices* **9**(3), 361 (2007).
- [98] M. MacDonald, G. Spalding, and K. Dholakia, *Nature* **426**(6965), 421 (2003).
- [99] G. M. Whitesides, *Nature* **442**(7101), 368 (2006).
- [100] B. S. Cho, T. G. Schuster, X. Zhu, D. Chang, G. D. Smith, and S. Takayama, *Analytical chemistry* **75**(7), 1671 (2003).
- [101] S. R. McCandlish, A. Baskaran, and M. F. Hagan, *Soft Matter* **8**(8), 2527 (2012).
- [102] M. Mijalkov and G. Volpe, *Soft Matter* **9**(28), 6376 (2013).
- [103] I. Berdakin, Y. Jeyaram, V. V. Moshchalkov, L. Venken, S. Dierckx, S. J. Vanderleyden, A. V. Silhanek, C. A. Condat, and V. I. Marconi, *Phys. Rev. E* **87**, 052702 (2013).
- [104] C. Maggi, A. Lepore, J. Solari, A. Rizzo, and R. Di Leonardo, *Soft Matter* **9**(45), 10885 (2013).
- [105] W. Yang, V. Misko, K. Nelissen, M. Kong, and F. Peeters, *Soft Matter* **8**(19), 5175 (2012).
- [106] A. Kaiser, H. Wensink, and H. Löwen, *Phys. Rev. Lett.* **108**(26), 268307 (2012).
- [107] H. Wensink and H. Löwen, *Phys. Rev. E* **78**(3), 031409 (2008).
- [108] G. Li and J. X. Tang, *Phys. Rev. Lett.* **103**(7), 078101 (2009).
- [109] A. Kaiser, K. Popowa, H. Wensink, and H. Löwen, *Phys. Rev. E* **88**(2), 022311 (2013).
- [110] X. Yang, M. L. Manning, and M. C. Marchetti, *Soft Matter* **10**, 6477 (2014).
- [111] J. Hill, O. Kalkanci, J. L. McMurry, and H. Koser, *Phys. Rev. Lett.* **98**(6), 068101 (2007).
- [112] R. Nash, R. Adhikari, J. Tailleur, and M. Cates, *Phys. Rev. Lett.* **104**(25), 258101 (2010).
- [113] A. Zöttl and H. Stark, *Phys. Rev. Lett.* **108**(21), 218104 (2012).

## REFERENCES

---

- [114] A. Zöttl and H. Stark, *The European Physical Journal E* **36**(1) (2013).
- [115] R. Rusconi, J. S. Guasto, and R. Stocker, *Nature Physics* (2014).
- [116] D. van der Meer, P. Reimann, K. van der Weele, and D. Lohse, *Phys. Rev. Lett.* **92**(18), 184301 (2004).
- [117] M. O. Magnasco, *Phys. Rev. Lett.* **71**(10), 1477 (1993).
- [118] J. Rousselet, L. Salome, A. Ajdari, and J. Prost, *Nature* **370**(6489), 446 (1994).
- [119] H. Chen, Q. Wang, and Z. Zheng, *Phys. Rev. E* **71**, 031102 (2005).
- [120] F. Jülicher, A. Ajdari, and J. Prost, *Rev. Mod. Phys.* **69**(4), 1269 (1997).
- [121] P. Reimann, *Physics Reports* **361**(2), 57 (2002).
- [122] P. Hänggi and F. Marchesoni, *Rev. Mod. Phys.* **81**(1), 387 (2009).
- [123] L. Angelani, A. Costanzo, and R. Di Leonardo, *EPL* **96**(6), 68002 (2011).
- [124] E. Yariv and O. Schnitzer, *Phys. Rev. E* **90**, 032115 (2014).
- [125] A. Sokolov, M. M. Apodaca, B. A. Grzybowski, and I. S. Aranson, *Proc. Natl. Acad. Sci. U.S.A.* **107**(3), 969 (2010).
- [126] P. Galajda, J. Keymer, P. Chaikin, and R. Austin, *J. Bacteriol.* **189**(23), 8704 (2007).
- [127] A. Pototsky, A. M. Hahn, and H. Stark, *Phys. Rev. E* **87**(4), 042124 (2013).
- [128] P. K. Ghosh, V. R. Misko, F. Marchesoni, and F. Nori, *Phys. Rev. Lett.* **110**(26), 268301 (2013).
- [129] S. Elizabeth Hulme, W. R. Di Luzio, S. S. Shevkoplyas, L. Turner, M. Mayer, H. C. Berg, and G. M. Whitesides, *Lab Chip* **8**, 1888 (2008).

Ich versichere, dass ich die von mir vorgelegte Dissertation selbständig angefertigt, die benutzten Quellen und Hilfsmittel vollständig angegeben und die Stellen der Arbeit - einschliesslich Tabellen, Karten und Abbildungen -, die anderen Werken im Wortlaut oder dem Sinn nach entnommen sind, in jedem Einzelfall als Entlehnung kenntlich gemacht habe; dass diese Dissertation noch keiner anderen Fakultät oder Universität zur Prüfung vorgelegen hat; dass sie - abgesehen unten angegebenen Teilpublikationen - noch nicht veröffentlicht worden ist sowie, dass ich eine solche Veröffentlichung vor Abschluss des Promotionsverfahrens nicht vornehmen werde. Die Bestimmungen der Promotionsordnung sind mir bekannt. Die von mir vorgelegte Dissertation ist von Professor G. Gompper betreut worden.

- Costanzo A. et al. "Motility-sorting of self-propelled particles in microchannels." EPL **107** 36003 (2014)

Jülich, den 1. Februar 2015

## Curriculum vitae

Vorname: Andrea  
Name: Costanzo  
Geschlecht: maennlich  
Geburtsdatum: 9.2.1986  
Geburtsort: Neapel (Italien)  
Staatsangehoerigkeit: italienisch

- ab 11.2011 **Doktorand** am Institute for Complex Systems, Theoretical Biophysics and Soft Matter, Forschungszentrum Juelich
- 3.2011-31.10.2011 Wissenschaftlicher Mitarbeiter in Rom, Italien  
Istituto per i processi chimico fisici, IPCF-CNR
- 10.2008-23.9.2010 **Master** (M. Sc.) Physik  
Universitaet „La Sapienza“ Rom,  
mit der Endnote 110/110 *magna cum laude* abgeschlossen  
Masterarbeit: „Numeric study of the motion of bacteria in a channel“  
Beteruer: Dr. L. Angelani
- 9.2005-29.9.2008 **Bachelor** Physik  
Universitaet „La Sapienza“ Rom, Italien  
mit der Endnote 110/110 abgeschlossen.  
Bachelorarbeit: „Minimal models of low Reynolds number swimmer“  
Betreuer: Dr. R. Di Leonardo
- 13.5.2005 **Abiturpruefung:**  
Deutsche Schule Rom, Endnote 1,5  
Die Schule verlieh ihm einen Preis fuer die besonderen Leistungen  
in den Faechern Physik und Chemie.

## **Veroeffentlichungen:**

- A. Costanzo, J. Elgeti, T. Auth, G. Gompper and M. Ripoll,  
"Motility-sorting of self-propelled particles in microchannels",  
EPL **107** 36003 (2014)
- A. Costanzo, R. Di Leonardo, G. Ruocco and L. Angelani,  
"Transport of self-propelling bacteria in micro-channel flow",  
Journal of Physics: Condensed Matter **24**, 065101 (2012)
- L. Angelani, A. Costanzo and R. Di Leonardo,  
„Active ratchets“,  
Europhysics Letters **96**, 68002 (2011)